Princetonlaan 6
3584 CB Utrecht
P.O. Box 80015
3508 TA Utrecht
The Netherlands

www.tno.nl

T +31 88 866 42 56
F +31 88 866 44 75

TNO report

TNO 2016 R10425

Groningen field 2013 to present
Gas production and induced seismicity

Date 14 April 2016

Author(s) Karin van Thienen-Visser, Danijela Sijacic, Jan-Diederik van Wees, Dirk Kraaijpoel, Joost Roholl

Copy no
No. of copies
Number of pages 92 (incl. appendices)
Number of appendices
Sponsor
Project name G1 Groningen winningsplancyclus
Project number 060.20655/01.08.02

Summary

A production plan for the Groningen field was submitted in 2013. In 2016 submission of an updated production plan for the Groningen field is expected.

State Supervision of Mines (Staatstoezicht op de Mijnen, SodM) has requested the following technical evaluations from TNO-AGE:

- Update on production and seismicity of the Groningen field
- Update of event density maps

New results on statistics and physical understanding are to be discussed in the light of mitigation of seismic hazard of the Groningen field.

These activities have been performed within the framework of the yearly work plan for the Ministry of Economic Affairs (reference AGE 16-10.009).

Production and seismicity of the Groningen field

Some major changes in production and seismicity of the Groningen field have occurred since EZ launched a dedicated research program in 2013 (TK 2012-2013 33529, no. 2). An overview is presented of production reduction measures and trends in seismic events.

Production

Since 2014 there have been a number of production reduction measures (Table i).

Table i. Overview of production reduction measures in the Groningen field

Date	Reduction measures by the Minister of Economic Affairs
17 January 2014	○ A maximum field production of 42. bcm for 2014 ○ Maximum 3 bcm for the Loppersum clusters
December 2014	○ A maximum production of 39.4 bcm for 2015 ○ Maximum 3 bcm for the Loppersum clusters ○ Maximum 9.9 bcm for the clusters close to Hoogezand-Sappemeer for the period 1st October 2015 until 30th September 2016 ○ Maximum 2 bcm for the Eemskanaal cluster
February 2015	○ Maximum field production of 16.5 bcm for the first six months of 2015
14 April 2015	○ Limit production from Loppersum clusters to necessity for the security of supply
23 June 2015	○ Maximum field production of 13.5 bcm for the last six months of 2015
18 November 2015	○ Maximum field production of 27 bcm for the gas year 2015/2016

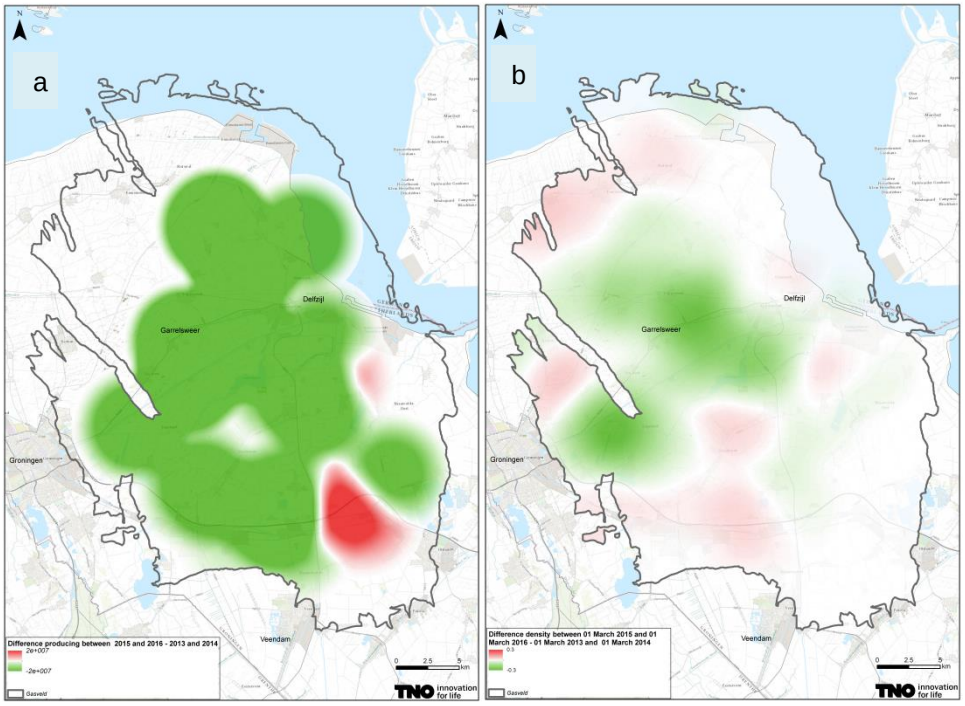

Figure i a. The difference in production between 2015 and 2013. Green indicates a lower level in 2015 compared to 2014, red a higher level, both with a maximum of $2 \cdot 10^7$ Nm^3. The red area is caused by production of Scheemderzwaag (SZW) and de Eeker (EKR). The densities were determined using a Kernel Density (standard GIS application) with a radius of 5 km and a cell size of 50 m.

b. The difference in event density between 2015 and 2013. Green indicates a lower level in 2015 compared to 2014, red a higher level, both with a maximum of 0.3 events per km^2. The densities were determined using a Kernel Density (standard GIS application) with a radius of 5 km and a cell size of 50 m.

NAM has complied with these production reduction measures. As a result production in the field has fallen considerably compared to 2013 (Figure i-a). Additionally, production has been distributed differently over the field.

Seismicity

Seismicity of the Groningen field has dropped considerably since 2013 (Figure i-b). Compared to 2013 there are less seismic events in the Loppersum area. Statistical analysis for the entire field shows a lower seismic event rate since May 2014[1]. Event rates have decreased rapidly since 2013 (Figure ii). These findings are statistically more meaningful compared to earlier studies (TNO 2015b, c).

[1] about 44 events per year with magnitudes larger than or equal to 1.0 ($M_L \geq 1.0$).

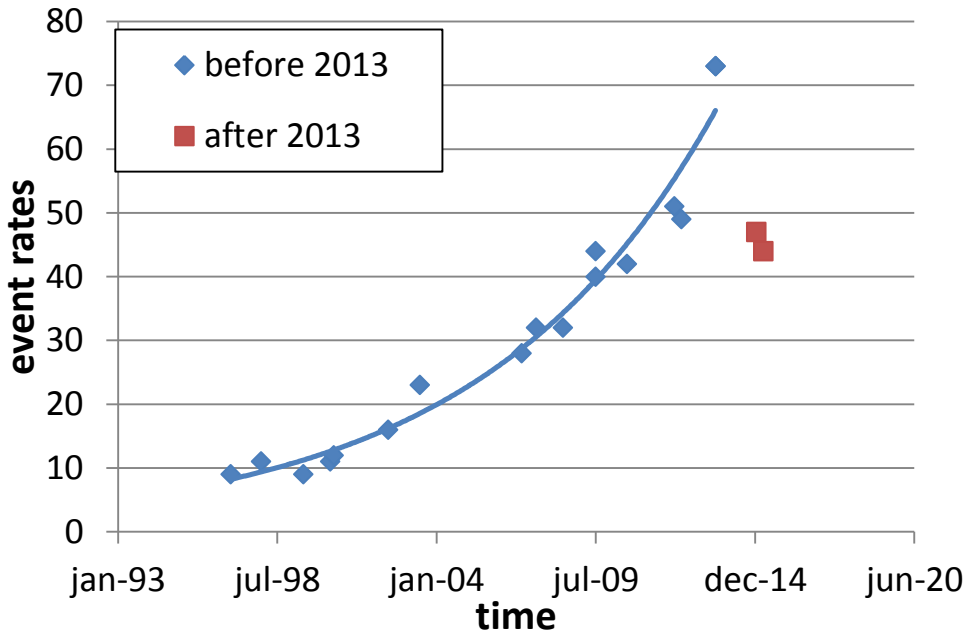

Figure ii. Event rate ($M_L \geq 1.0$) change with time for the entire Groningen field according to the Bayesian change point model results. The solid lines are meant as illustration. The exponential fits are made through the data before and after 2013. However, the fits have been made without taking into account uncertainties and, thus, cannot be used to make conclusions on event rates for the Groningen field.

Physical understanding of the cause of seismicity

In 2013 (NAM 2013), compaction was used as a first order approximation for the short term prognosis of seismicity in the Groningen field. Observations of induced seismicity since 2014, after the reduction of production in the Loppersum clusters, showed that the relation is more complex (TNO 2015b, c). Time dependent compaction models, which fit the observations of subsidence best, do not explain the drop in seismicity since 2014. Geomechanical models predict that the relationship of compaction and seismicity breaks since 2014. Consequently, time dependent compaction does not lead to additional seismicity Linear compaction models, on the other hand, do not fit the observations of subsidence, but can explain the occurrence of seismicity due to their instant reaction to a pore pressure (or stress) change (Figure iii).
In summary, compaction can be used as a proxy for seismicity, in the absence of a proper physical model and in case no significant changes (like production reduction measures) occur.

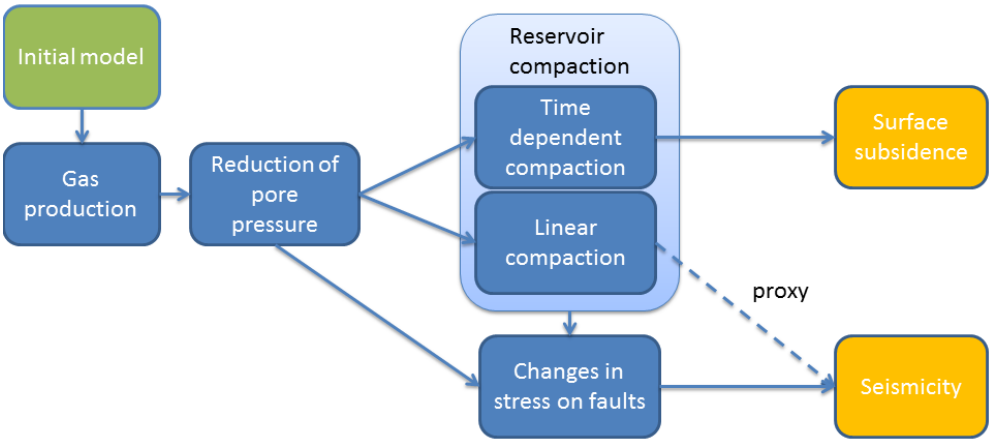

Figure iii Improved schematic of the relation between gas production and seismicity

Scope for mitigation of seismic hazard

In 2013 (NAM 2013) compaction was used as a proxy for the occurrence of seismicity for the next 2 to 3 years. There was not a clear correlation between estimated event locations and mapped faults. It was expected that any beneficial changes in seismicity due to production reduction measures would be temporary.

Now, in 2016 we have learned that seismicity is not primarily caused by compaction. Faults play a major role. Observations of seismic events recorded in borehole stations indicate that events occur on known faults (NAM 2015). Faults in the Loppersum area are likely more prone to movement caused by increasing stresses on the faults due to their favorable orientation in the stress field, in conjunction to stress changes caused by pressure reduction, compaction, geometry and geological characteristics of the fault. Improved physical understanding indicates that seismicity rates are expected to be correlated primarily to rates of pressure change. These findings support scope for mitigation of induced seismicity adjusting production scenarios.

Contents

Summary **2**

1 Introduction **10**

2 Observations of gas production and induced seismicity in Groningen since 2013 ..... **12**
2.1 Production in 2014 and 2015 12
2.2 Production density maps 18
2.3 Seismicity in 2014 and 2015 20
2.4 Event density maps 22
2.5 Production and seismicity: comparing 2015 to 2013 23

3 Statistical data analysis **25**
3.1 Magnitude of completeness of the Groningen field in the period 1995 to 2014 25
3.2 Bayesian change point analysis 27
3.3 Influence of the magnitude of completeness in Groningen 31

4 Compaction as a proxy for seismicity **34**

5 Findings **36**

6 References **40**

7 Signature **42**

Appendices
A Figures production and event density
B Catalogue completeness analysis for the Groningen borehole seismic network (from 1996 until extension in fall 2014)
C Appendix Bayesian change point
D Time dependent compaction and induced seismicity: inferences from geomechanical modelling of gas depletion

Figures

Figure 1-1. The chain of building blocks needed for the seismic hazard and risk assessment. 10
Figure 2-1. locations of the clusters in the Groningen field and their abbreviations . 13
Figure 2-2 a) Yearly production (bcm) of the Groningen field in 2013, 2014 and 2015 (www.nlog.nl). The red lines indicate the production limits in 2014 and 2015. b) Monthly production (bcm) of the Groningen field in 2013, 2014 and 2015 (www.nlog.nl). 14
Figure 2-3 a) Yearly production (bcm) of the Loppersum clusters in 2013, 2014 and 2015. The red line indicates the imposed production limit in 2014 and 2015 (www.nlog.nl). b) Monthly production (bcm) of the Loppersum clusters in the year 2013, 2014 and 2015 (www.nlog.nl). 14
Figure 2-4 Monthly production (bcm) of the Loppersum clusters Leermens (LRM), Overschild (OVS), De Paauwen (PAU), TEN Post (POS) and 't Zand (ZND) for 2013 (top), 2014 (middle) and 2015 (bottom) (www.nlog.nl). 15
Figure 2-5 Half yearly production (bcm) of the Groningen field in 2015 (www.nlog.nl). 16
Figure 2-6. a) Yearly production (bcm) of the Eemskanaal (EKL) cluster for 2013, 2014 and 2015. The red line indicates the imposed production limit of 2 bcm for 2015 (www.nlog.nl). b) Monthly production (bcm) of the Eemskanaal (EKL) cluster in 2013, 2014 and 2015 (www.nlog.nl). 17
Figure 2-7. a) Yearly production (bcm) in the southwest clusters for the years 2013, 2014 and 2015 (www.nlog.nl). b.) Monthly production (bcm) in the southwest clusters for the years 2013, 2014 and 2015 (www.nlog.nl). 17
Figure 2-8. Monthly production of the Southwest clusters (Froombosch (FRB), Kooipolder (KPD), Slochteren (SLO), Zuiderveen (ZDV), Spitsbergen (SPI), Tusschenklappen (TUS), Sappemeer (SAP)) for 2013 (top), 2014 (middle) and 2015 (bottom) (www.nlog.nl). 18
Figure 2-9. Top: Density of production (Nm3 per km^2) from March 2013 to March 2016. The producing/non-producing clusters are indicated by the colored small circles (green indicates producing, blue indicates non-producing). Bottom: Difference in production (in Nm^3 per km^2) between the indicated periods. A negative difference in production, shown in green, indicates a lower production between in the later period compared to the earlier period. Larger size figures are shown in Appendix A. 19
Figure 2-10 Observed seismic events with magnitude above M_L=1.0 from January 2014 to March 2016. The colour scale indicates the magnitude of the events and the Groningen 'gas field contour is indicated in red. 20
Figure 2-11 Number of events with magnitudes larger than or equal to 1.5 registered in the Groningen field from the start of seismicity in 1991 to 2015. .22
Figure 2-12 Top: Event density (number of events per km^2) 1 March 2013 to 1 March 2016 per year. The observed events and their magnitudes are indicated by the coloured small circles. Bottom: Difference in event density between the indicated periods. A negative difference (green) indicates a lower event density in the later period compared to the earlier period. A positive difference is indicated in red. Larger size figures are shown in Appendix A. 23

Figure 2-13a. The difference in production between 2015 and 2013 and b. The difference in event density in 2015 and 2013. Green indicates a lower level in 2015 compared to 2014, red a higher level. 24
Figure 3-1. Magnitude of completeness contours for the Groningen borehole network in the period 1996-2010, based on a probabilistic model for event detection. Magnitude of completeness is defined to be the lowest magnitude that has a 95% probability of being detected in 3 or more borehole stations....26
Figure 3-2 Magnitude of completeness contours for the Groningen borehole network in the period 2010-2014, based on a probabilistic model for event detection. Magnitude of completeness is defined to be the lowest magnitude that has a 95% probability of being detected in 3 or more borehole stations....26
Figure 3-3a. Illustration of the Bayesian change point analysis in the case of a single step increase in event rate and (b) a gradually increasing event rate with time, as can be seen in the seismicity catalogue for Groningen. In case situation (b) occurs in reality, the Bayesian Change point model will find situation (a) for a single time window. 28
Figure 3-4. Event rates ($M_L \geq 1.0$) change with time for the entire Groningen field. The solid lines are the exponential fits trough the data before and after 2013. The data are shown in Table C-1 in Appendix C. The exponential fits are made through the data before and after 2013. However, the fits have been made without taking into account uncertainties and, thus, cannot be used to make conclusions on event rates for the Groningen field. 29
Figure 3-5a. Probability density functions for the pre change date event rate (in events/day) – dashed line and the post change date event rates (in events/day) for the change point of May 19th 2014 and (b) The probability density function of the change point in time over the period of 2012 up to now (March 2016). 30
Figure 3-6a. Histogram of declustered seismic data for Groningen field and events M≥1.0 and b. for declustered seismic data for the Groningen field and events M≥1.3. 31
Figure 3-7. Event rate change with time for the entire Groningen field and all magnitudes above 1.3. The data are shown in Table C-2 in Appendix C. 32
Figure 4-1. Schematic of the relation between gas production and seismicity 34
Figure 4-2 Improved schematic of the relation between gas production and seismicity 35

Tables

Table 1-1. Overview of previous TNO reports 10
Table 2-1 Overview of the limits imposed by the Minister of Economic Affairs on the production of the Groningen field in 2014 and 2015. Cluster locations are indicated in Figure 2-1. 12
Table 2-2 Induced seismic events (source: KNMI) of the Groningen field with M_L>2.0 for the period January 2014-March 2016 21
Table 3-1. Overview of investigated time intervals and the resulting change points in event rate. The Bayes factor determines the odds of a change point model over one single constant rate model. Table includes results from TNO 2015b. Results highlighted in red are further elaborated in section 3.2.1. 29
Table 3-2. Overview of investigated time intervals and the resulting change points in event rate for events of M_L≥1.3. The Bayes factor determines the odds of change point model above one single constant rate model. The latest investigated time interval includes only events in 10 km radius around central point (latitude 53.297 and longitude 6.782) in the Loppersum area with magnitudes M_L≥1.2, since this is the magnitude of completeness for this area (section 3.1). 32

1 Introduction

Background

In 2012, the largest induced seismic event caused by gas depletion of the Groningen gas field occurred. This event triggered investigations into the rate of seismic events, their magnitudes, ground accelerations and damages of houses and infrastructure (Figure 1-1).

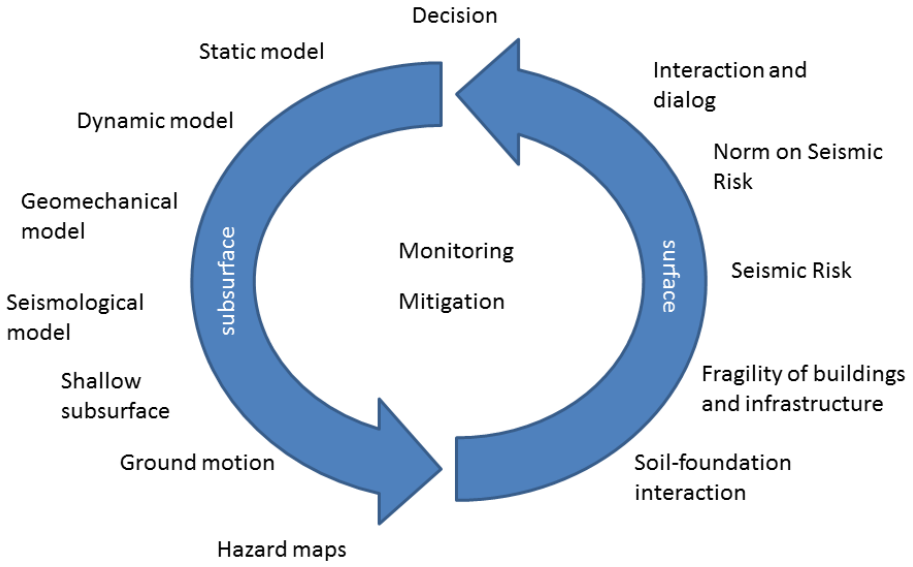

Figure 1-1. The chain of building blocks needed for the seismic hazard and risk assessment.

Figure 1-1 illustrates the building blocks that are needed to make hazard and risk analysis for the induced seismicity in Groningen. Many of the building blocks have been analysed in previous TNO reports (Table 1-1).

Table 1-1. Overview of previous TNO reports

Which report	Focus on building block
TNO (2013)	Static, Dynamic, Geomechanical and Seismological model
TNO (2014a)	Dynamic and Geomechanical model
TNO (2014b)	Monitoring and Mitigation, Static, Dynamic and Geomechanical model
TNO and CBS (2014)	Monitoring and Mitigation
TNO (2015a)	Movement at the surface, Ground motion, Hazard maps, Fragility of Buildings, Seismic risk
TNO (2015b)	Monitoring and Mitigation, Geomechanical model
TNO (2015c)	Monitoring and Mitigation, Geomechanical model
TNO (2015d)	Dynamic, Geomechanical and Seismological model
TNO and KNMI (2015)	Hazard maps

Scope

State Supervision of Mines (Staatstoezicht op de Mijnen, SodM) has requested (per e-mail January 26 2016) the following technical evaluations from TNO-AGE:

- Update on production and seismicity of the Groningen field
- Update of event density maps

New results on statistics and physical understanding are discussed in the light of mitigation of seismic hazard of the Groningen field.

These evaluations are performed within the framework of the yearly work plan for the Ministry of Economic Affairs (reference AGE 16-10.009).

Report Setup

Chapter 2 focuses on the observations of production and seismicity since the update of the Groningen production plan in 2013. In Chapter 3 the catalogue completeness is examined in the period between 1996 up to October 2014. A summary of earlier findings concerning the statistical analysis of the events using the Bayesian change point model is shown. Additionally the magnitude of completeness is used to check for changes in seismicity since 2014. In chapter 5 compaction as a proxy for the occurrence of seismicity is re-evaluated using geomechanical modelling and time dependent compaction. Finally in chapter 6 the findings are summarized.

2 Observations of gas production and induced seismicity in Groningen since 2013

In this chapter the production of the Groningen field in 2014 and 2015 is shown and compared to the production limits imposed by the Minister of Economic Affairs; earlier production in 2013 is shown as well (section 2.1 - section 2.2*)*. Secondly, the seismicity of the Groningen field is evaluated using recent observations (section 2.3) and event densities (section 2.4).

2.1 Production in 2014 and 2015

Table 2-1 shows the overview of the limits imposed by the Minister of Economic Affairs on the production of Groningen field in 2014 and 2015. In the next paragraphs these production reduction measures will be discussed for each calendar year (2014, 2015).

Table 2-1 Overview of the limits imposed by the Minister of Economic Affairs on the production of the Groningen field in 2014 and 2015. Cluster locations are indicated in Figure 2-1.

Date	Reduction measure by the Minister of Economic Affairs
17 January 2014	○ A maximum production of 42,5 bcm for 2014 ○ Maximum 3 bcm for the Loppersum clusters (Leermens, Overschild, de Paauwen, Ten Post, Het Zand)
December 2014	○ A maximum production of 39,4 bcm for 2015 ○ Maximum 3 bcm for the Loppersum clusters (Leermens, Overschild, de Paauwen, Ten Post, Het Zand) ○ Maximum 9,9 bcm for the clusters close to Hoogezand-Sappemeer (Kooipolder, Slochteren, Zuiderveen, Spitsbergen, Tusschenklappen, Froombosch, Sappemeer) for the period 1st October 2015 until 30th September 2016 ○ Maximum 2 bcm for the Eemskanaal cluster
February 2015	○ Maximum production of 16,5 bcm for the first six months of 2015
14 April 2015	○ Limit production from Loppersum clusters if necessary for the security of supply
23 June 2015	○ Maximum production of 13,5 bcm for the last six months of 2015
18 November 2015	○ Maximum production of 27 bcm for the gas year 2015/2016

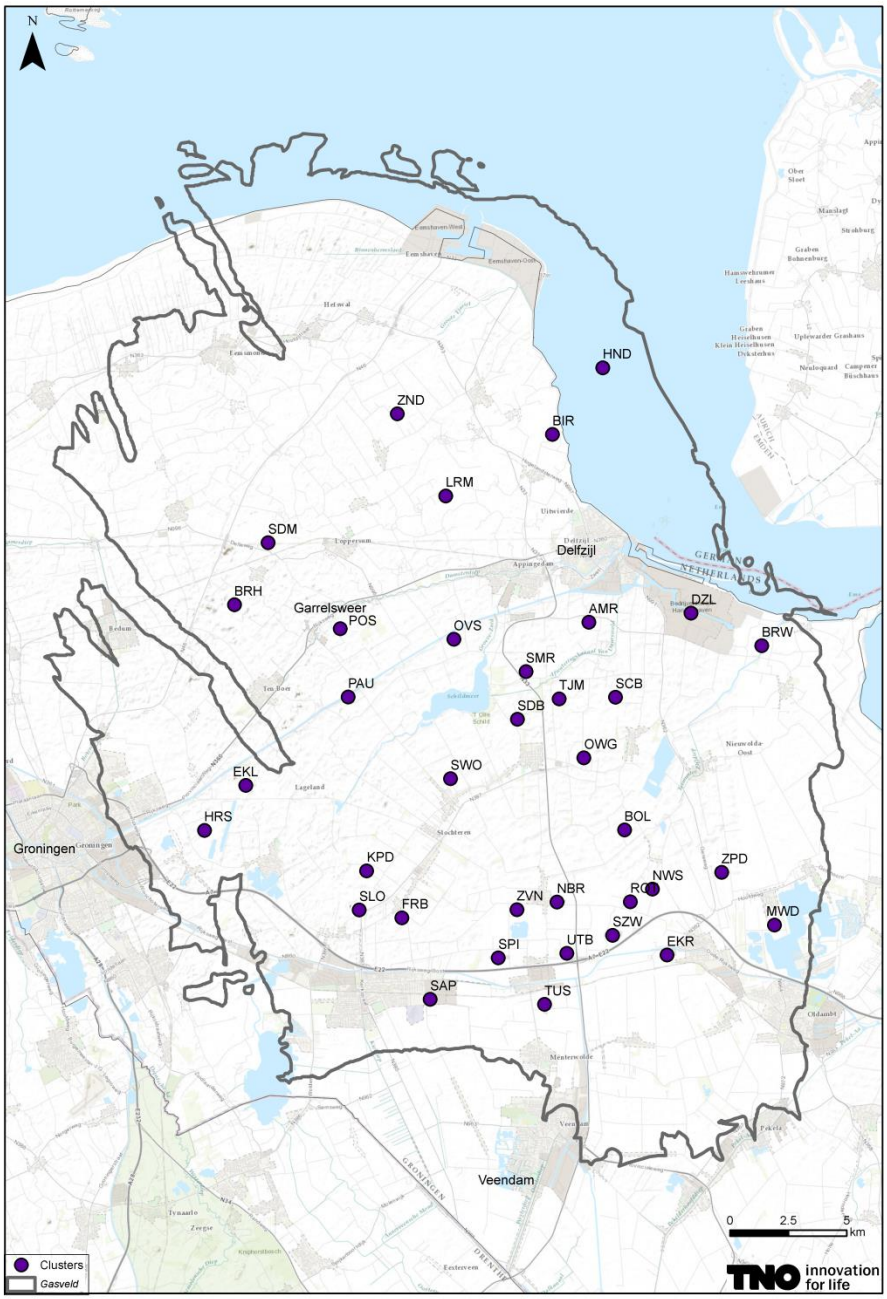

Figure 2-1. locations of the clusters in the Groningen field and their abbreviations

2.1.1 Production reduction measures 2014

On January 17th of 2014 gas production of the Groningen field was limited to 42.5 bcm for the year 2014 by the Minister of Economic Affairs in reaction to the increase in seismicity leading up to a M_L=3.6 event in August 2012. Additionally the production of the Loppersum clusters (Leermens (LRM), Overschild (OVS), De Paauwen (PAU), Ten Post (POS) and 't Zand (ZND)) was limited to 3 bcm per year.

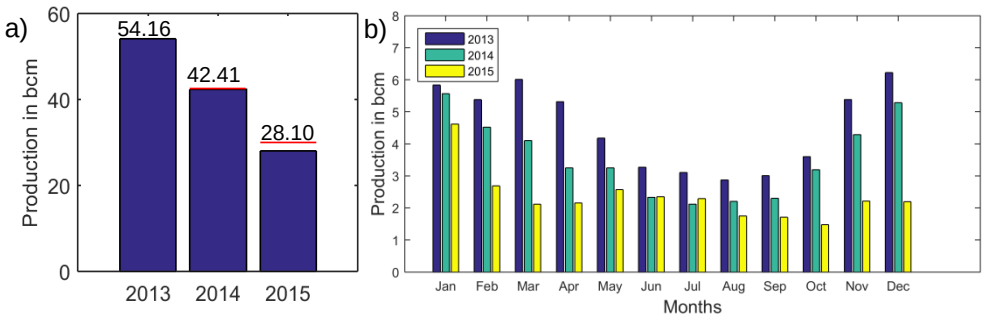

Figure 2-2 a) Yearly production (bcm) of the Groningen field in 2013, 2014 and 2015 (www.nlog.nl). The red lines indicate the production limits in 2014 and 2015. b) Monthly production (bcm) of the Groningen field in 2013, 2014 and 2015 (www.nlog.nl).

In comparison to 2013 the actual production in 2014 was reduced from 54.16 bcm to 42.41 bcm, which is under the imposed maximum (Figure 2-2a). The monthly production pattern in 2014 is similar to that of 2013, with higher production in the winter months and lower production in the summer months *(*Figure 2-2b). The reduction of production in 2014 was achieved largely by the reduction of production in the Loppersum area from 17.2 bcm in 2013 to 2.59 bcm in 2014 (Figure 2-3a). Production of the Loppersum clusters was highest in January and December 2014. Production in all Loppersum clusters (LRM,OVS, PAU, POS and ZND) has been reduced with negligible production of the PAU cluster from April 2014 until March 2015 (Figure 2-4).

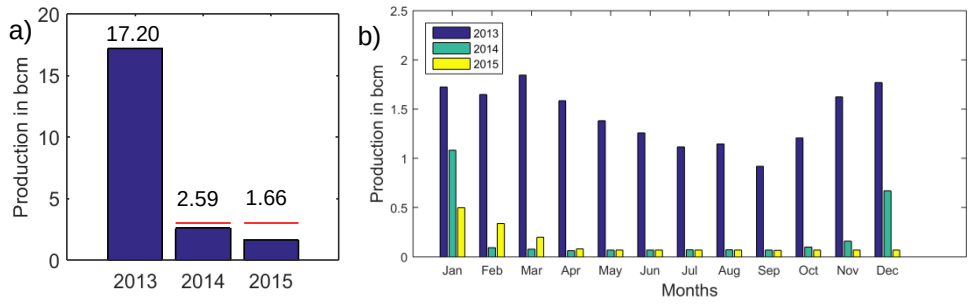

Figure 2-3 a) Yearly production (bcm) of the Loppersum clusters in 2013, 2014 and 2015. The red line indicates the imposed production limit in 2014 and 2015 (www.nlog.nl). b) Monthly production (bcm) of the Loppersum clusters in the year 2013, 2014 and 2015 (www.nlog.nl).

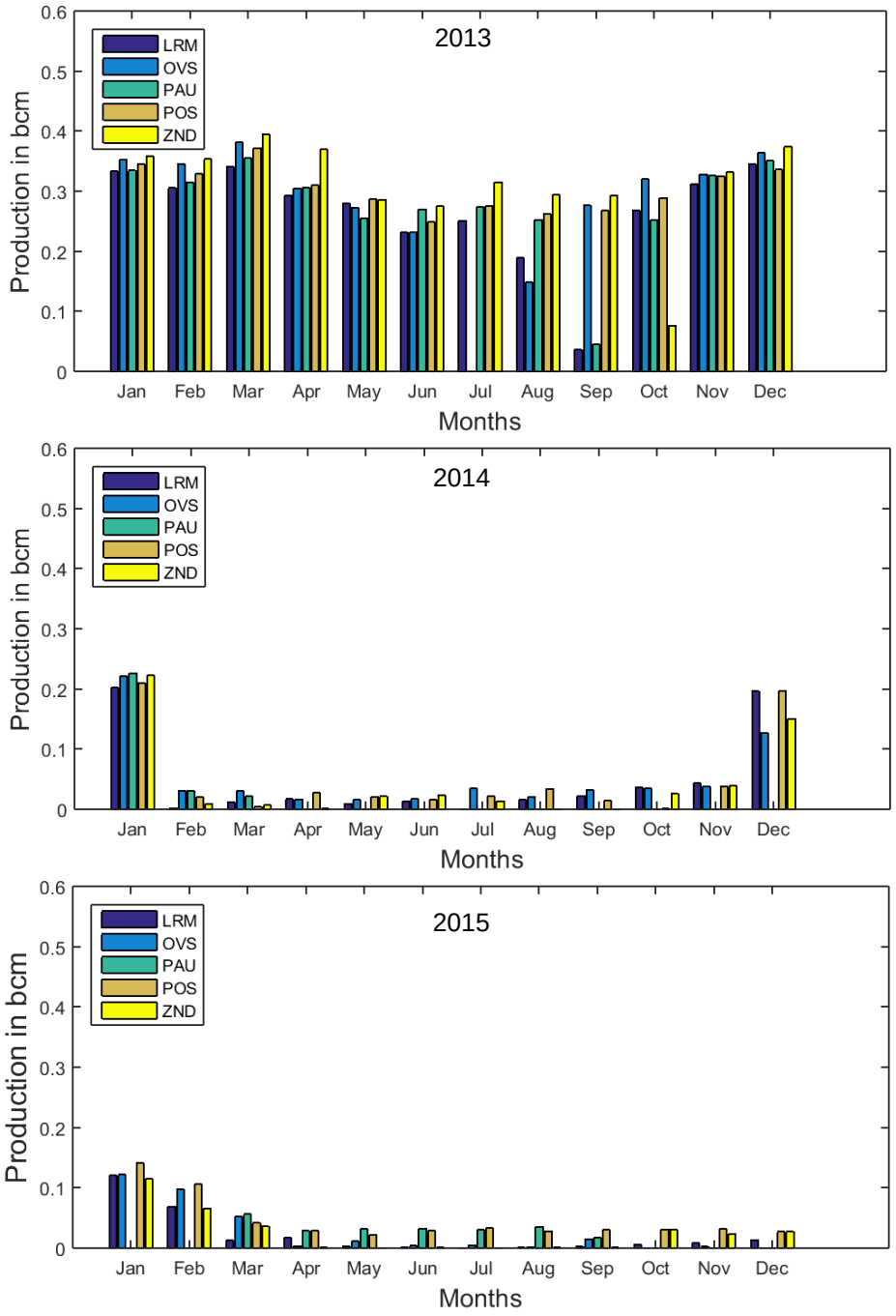

Figure 2-4 Monthly production (bcm) of the Loppersum clusters Leermens (LRM), Overschild (OVS), De Paauwen (PAU), TEN Post (POS) and 't Zand (ZND) for 2013 (top), 2014 (middle) and 2015 (bottom) (www.nlog.nl).

2.1.2 Production reduction measures in 2015

Field wide

In the year 2015 additional limits to the gas production in Groningen were imposed. The gas production in the Groningen field was limited to 16.5 bcm for the first six months of 2015 (January 2015 to July 2015). After the first six months production was limited to a maximum of 30 bcm for 2015. On November 18th 2015 the Council

of State (Raad van State) decided on a limit on the gas production of the gas year 2015/2016 of 27.5 bcm based on the security of supply.

In addition the following regional limits on gas production were imposed in 2015:

- A maximum of 3.0 bcm per year for the Loppersum clusters (Leermens (LRM), Overschild (OVS), De Paauwen (PAU), Ten Post (POS) and ‘t Zand (ZND))
- A maximum of 2.0 bcm per year for the Eemskanaal (EKL) cluster
- A maximum of 9.9 bcm per year for the Southwest clusters (Froombosch (FRB), Kooipolder (KPD), Slochteren (SLO), Zuiderveen (ZDV), Spitsbergen (SPI), Tusschenklappen (TUS), Sappemeer (SAP))

In comparison to 2013 and 2014 actual gas production in Groningen was reduced to 28.1 bcm (Figure 2-1), below the imposed limit of production for 2015 (30 bcm). In the first half of 2015 the production was 16.48 bcm and the second half year 11.62 bcm (Figure 2-5). Both the yearly production and the half yearly production were below the maximum allowed production limits (16.5 bcm and 30 bcm respectively).

Gas production during the winter months of November and December 2015 was significantly lower compared to 2013 and 2014. Therefore, the seasonal production swing (higher production during the winter months and lower production in the summer months) was lower in 2015 compared to 2013 and 2014 (Figure 2-3).

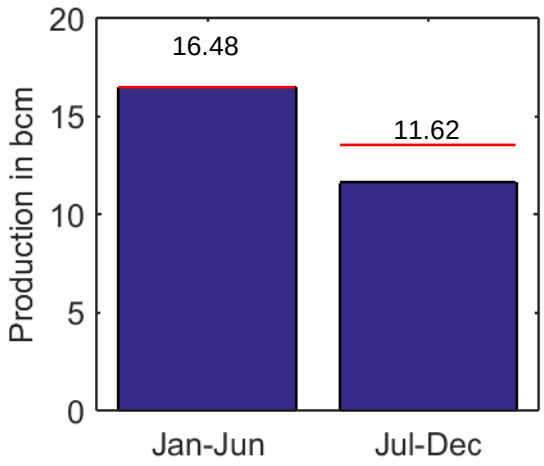

Figure 2-5 Half yearly production (bcm) of the Groningen field in 2015 (www.nlog.nl).

Loppersum clusters

Gas production in the Loppersum area was further reduced from 2.59 bcm to 1.66 bcm in 2015, which is below the imposed limit of 3 bcm. From January till March 2015 gas production for the Loppersum cluster was at a level of 0.3 - 0.5 bcm per month. For the remaining part of 2015 gas production in the Loppersum cluster remained below 0.1 bcm for each month.

Eemskanaal cluster

Gas production in 2013 and 2014 for the Eemskanaal cluster was 2.54 bcm and 2.09 bcm respectively. In 2015 gas production decreased to 1.14 bcm, which was below the imposed limit for Eemskanaal (2.0 bcm in 2015). Monthly gas production

rates for Eemskanaal in 2015 were lower compared to 2014, except for September 2015. In September 2014 Eemskanaal production was temporarily stopped for technical reasons.

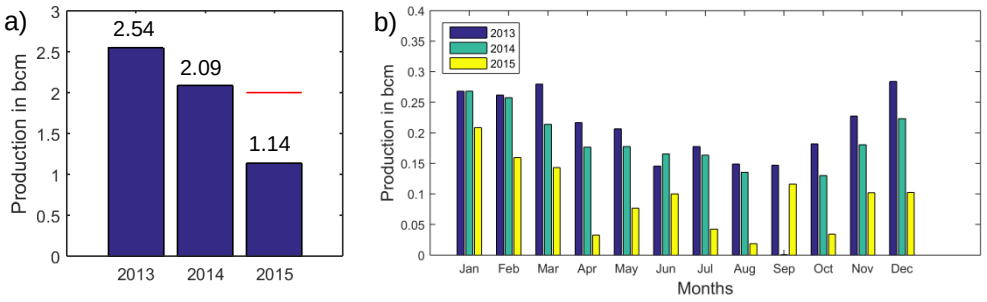

Figure 2-6. a) Yearly production (bcm) of the Eemskanaal (EKL) cluster for 2013, 2014 and 2015. The red line indicates the imposed production limit of 2 bcm for 2015 (www.nlog.nl).
b) Monthly production (bcm) of the Eemskanaal (EKL) cluster in 2013, 2014 and 2015 (www.nlog.nl).

Southwest clusters

The total production from the southwest clusters (Froombosch (FRB), Kooipolder (KPD), Slochteren (SLO), Zuiderveen (ZDV), Spitsbergen (SPI), Tusschenklappen (TUS), Sappemeer (SAP)) in 2015 was 8.15 bcm, which is under the imposed limit of 9.9 bcm. Gas production in 2013 and 2014 was 12.89 bcm and 13.57 bcm respectively. The reduction in 2015 was, therefore, significant (>60%). In 2013 and 2014 a seasonal pattern is seen in the production. In 2015 the production pattern has been more erratic with higher production in January and May till June and comparatively low production in November and December.

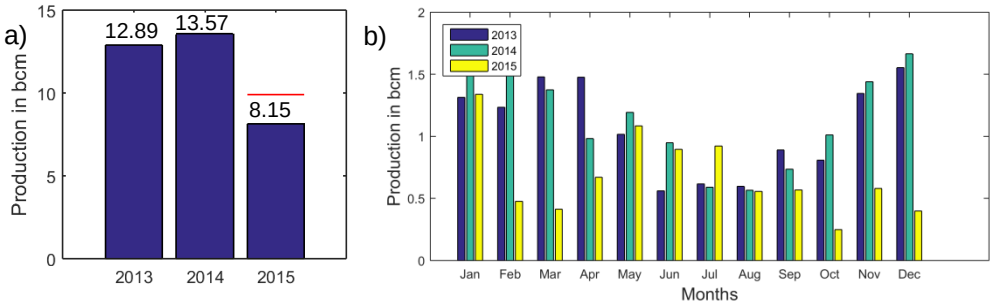

Figure 2-7. a) Yearly production (bcm) in the southwest clusters for the years 2013, 2014 and 2015 (www.nlog.nl).
b.) Monthly production (bcm) in the southwest clusters for the years 2013, 2014 and 2015 (www.nlog.nl).

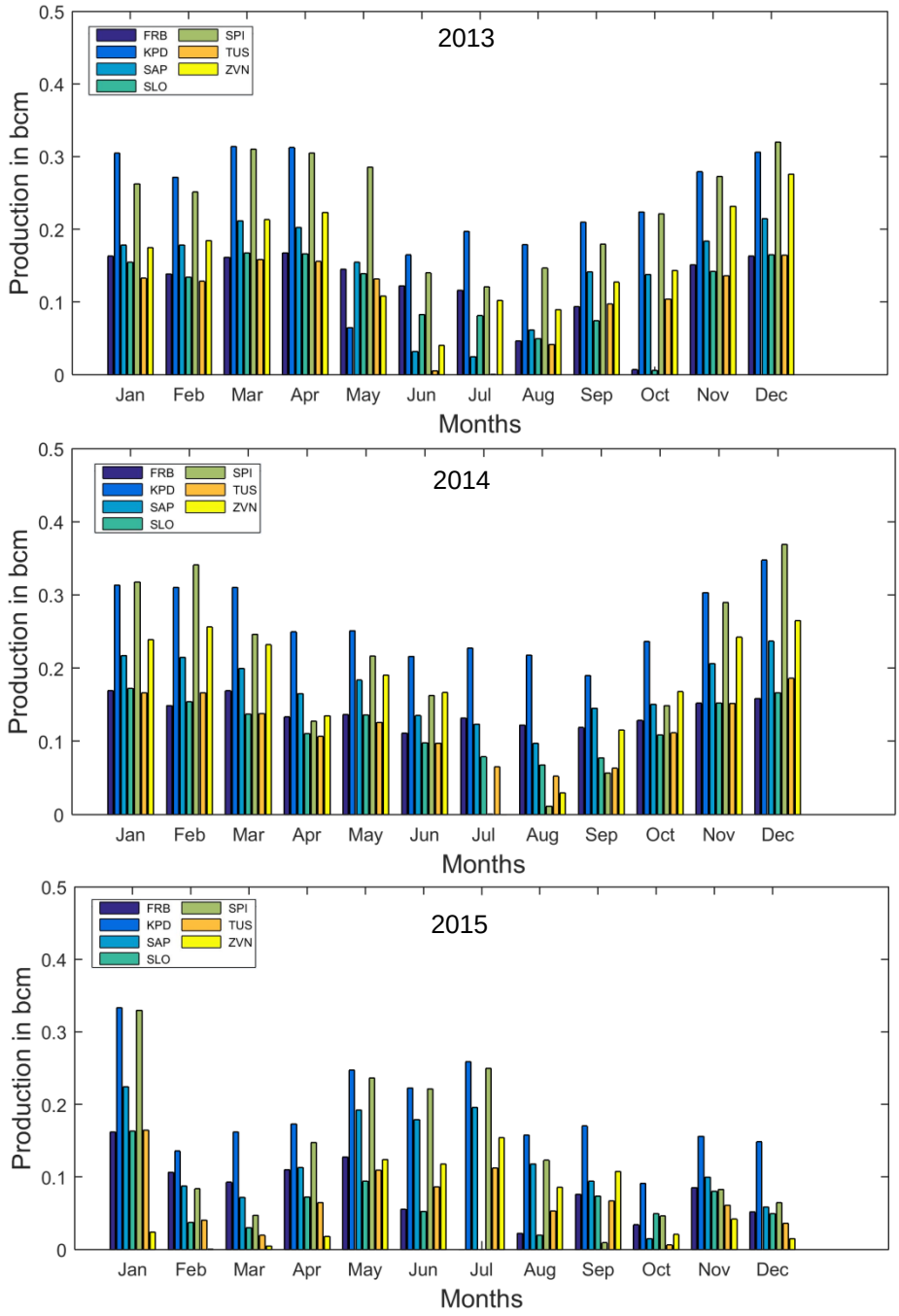

Figure 2-8. Monthly production of the Southwest clusters (Froombosch (FRB), Kooipolder (KPD), Slochteren (SLO), Zuiderveen (ZDV), Spitsbergen (SPI), Tusschenklappen (TUS), Sappemeer (SAP)) for 2013 (top), 2014 (middle) and 2015 (bottom) (www.nlog.nl).

2.2 Production density maps

Figure 2-9 shows the production density for the period of 1 March 2013 until March 2016 per year, as well as the differences in production density between those periods. The densities were determined using a Kernel Density (standard GIS application) with a radius of 5 km and a cell size of 50 m. Since January 2014 production has been reduced in the center of the Groningen field. In 2014, production was increased in the south, east and southeast of the field to

compensate for the reduction in the center of the field. In Figure 2-9 (bottom figure) it can be seen that there is a large decrease in the center and northwest of the field for the period 1 March 2014 to 1 March 2015 compared to the period 1 March 2013 to1 March 2014. Furthermore, a decrease in the south area in the field is observed. A small increase in production is seen in the southwestern part of the field and a larger increase in the northeastern part of the field. In January 2015, production in the southwest of the field was limited as well, leading to decreases in production in 2015. This can be seen clearly in the difference in production density the period 1 March 2015 to1 March 2016 compared to the period 1 March 2013 to 1 March 2014, where in almost the whole field a reduction of the production is observed. Only in two small patches a slight increase in production is seen.

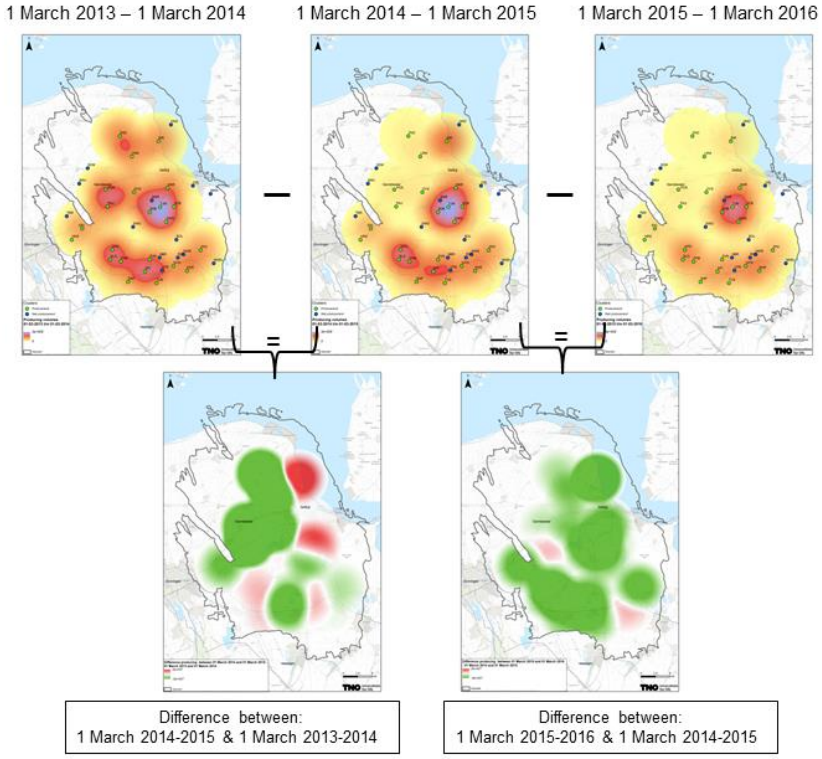

Figure 2-9. Top: Density of production (Nm3 per km^2) from March 2013 to March 2016. The producing/non-producing clusters are indicated by the colored small circles (green indicates producing, blue indicates non-producing). Bottom: Difference in production (in Nm^3 per km^2) between the indicated periods. A negative difference in production, shown in green, indicates a lower production between in the later period compared to the earlier period. Larger size figures are shown in Appendix A.

2.3 Seismicity in 2014 and 2015

Figure 2-10 shows the locations of the 96 seismic events with a magnitude above M_L=1.0 observed from January 2014 to March 2016. The largest event was observed near Hellum (30-09-2015) with a magnitude of M_L=3.1.

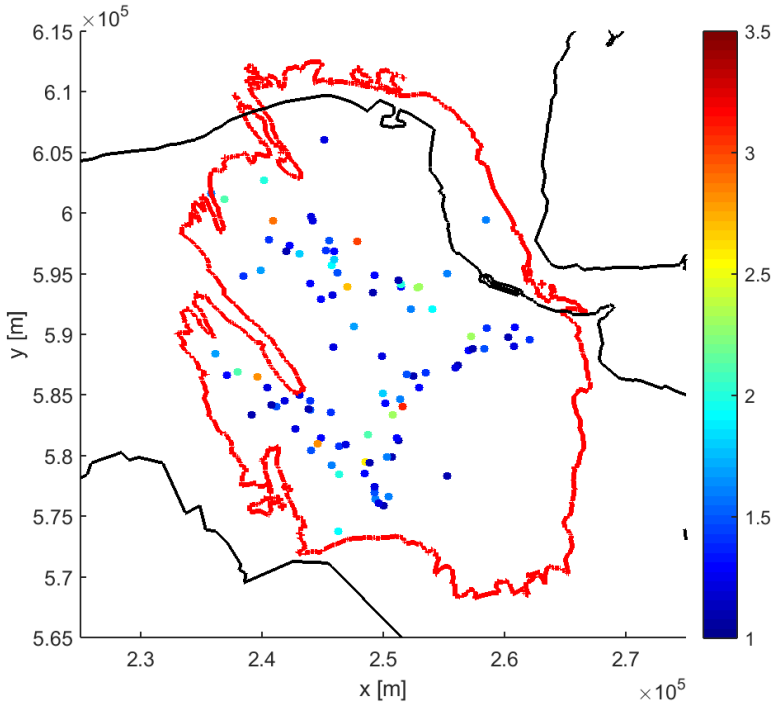

Figure 2-10 Observed seismic events with magnitude above M_L=1.0 from January 2014 to March 2016. The colour scale indicates the magnitude of the events and the Groningen 'gas field contour is indicated in red.

2.3.1 *Events above M_L=2.0*

Table 2-2 shows the induced seismicity of the Groningen field for the period January 2014 till March 2016 for all events larger than M_L=2.0. In 2014 there were 8 events with a magnitude above 2.0, in 2015 there were 5 events with a magnitude above 2.0. In the year 2016, up to March 1st one event larger than M_L=2.0 has been recorded.

Table 2-2 Induced seismic events (source: KNMI) of the Groningen field with M_L>2.0 for the period January 2014-March 2016

Event	Date	M_L
Leermens	13-02-2014	3.0
Schildwolde	11-03-2014	2.3
Rottum	18-03-2014	2.1
Slochteren	02-07-2014	2.1
Froombosch	01-09-2014	2.6
Garnerwolde	30-09-2014	2.8
Zandeweer	05-11-2014	2.9
Woudbloem	30-12-2014	2.8
Wirdum	06-01-2015	2.7
Appingedam	25-02-2015	2.3
Appingedam	24-03-2015	2.3
Thesinge	07-07-2015	2.1
Hellum	30-09-2015	3.1
Meedhuizen	30-10-2015	2.3
Froombosch	25-02-2016	2.4

Events in 2014

In previous rapports (TNO 2014a, b; 2015a, b) events with a $M_L \geq 2.0$ were described in relation to the production reduction in the Loppersum area. Production reduction in the Loppersum area will have influenced the pressure decline in that part of the field. This has influenced the number and possibly the magnitude of the events. A reduction in production will not lead to an immediate response of the reservoir due to the time it takes for a pressure wave (in the gas phase) to travel through the reservoir. Therefore the events above magnitude 2.0 (Table 2-2) occurring in February and March 2014 are not likely to have been influenced by the reduction of production in January 2014. The underlying assumption is the pressure diffusion model, which was presented in TNO (2014b).

The events in Garnerwolde and Woudbloem occurred in the southwest region of the field, not affected (yet) by the production reduction in the center of the field. In TNO (2014b) the southwest region has been described in more detail.

The Zandeweer event occurred in the north of the field in November 2014. At that time this part of the field had not yet been influenced by the production reduction of the Loppersum clusters (TNO, 2014b).

Events in 2015

Most of the events in 2015 were already discussed in previous rapports (TNO, 2015a-b), except for the event near Meedhuizen, which occurred after the publication of these rapports (October 30th 2014). The Meedhuizen event is close to the producing clusters of Amsweer (AMR), Siddeburen (SDB) and Tjuchem (TJM). For the Wirdum event we suggested the cause of the event might be the sudden increase in production in the near Ten Post (POS) cluster in December 2014. For the Appingedam events we concluded that the pressure wave associated with the continuing production in the nearby producing cluster(s) causes compaction which may explain the increase in seismic activity in this area. For both phenomena we concluded that it is too early to draw firm conclusions and more observations are

needed to enhance statistical significance. The event in Thesinge is close to the Eemskanaal (EKL) cluster which has been reduced in production since January 2015 to a maximum of 2 bcm per year.
The Hellum event on September 30th 2015 with a magnitude of M_L=3.1 has the most southern location of all M_L>3.0 events until now. This events fits in the trend that the seismicity (number of events and magnitude) of the Groningen field is expanding in time over the field, as mentioned in NAM (2013). The Hellum event took place at a location where an increase in compaction was calculated and subsequently an increase in potential seismic moment with a factor of about 1.6 (period 2014 to 2017) for scenarios where production was limited to 42.5 bcm, and 40 bcm/year for 2015 and 2016 (TNO 2014a). It should be noted that no firm conclusion can be drawn from a single event (such as the Hellum event). Also, the validity of the 2014 prognosis of potential seismic moment depends on actual production rather than the production forecast or scenario.

2.3.2 Stacked histogram from M_L≥1.5

Figure 2-11 shows the stacked histogram for all events higher than or equal to magnitude 1.5 for the Groningen field between 1991 and 2015.

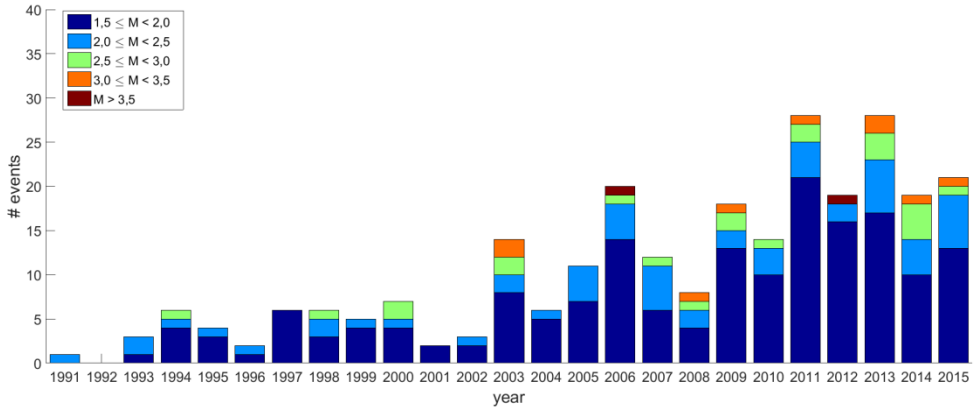

Figure 2-11 Number of events with magnitudes larger than or equal to 1.5 registered in the Groningen field from the start of seismicity in 1991 to 2015.

2.4 Event density maps

Figure 2-12 shows the event density for the period March 1st 2013 to March 1st 2016. The event densities were calculated using a Kernel Density (standard GIS application) with a radius of 5 km and a cell size of 50 m.
In general, event densities are lower in the period March 2015 to March 2016 than they were in both previous periods (Figure 2-13b). In January 2014 production was reduced in the center of the Groningen field. By comparing March 2013 – March 2014 with March 2014 - March 2015 a decrease in event density can be observed in the center and west part of the field.
An increase in event density can be observed in the southwest. The production of the southwest clusters was reduced in 2015. Comparing March 2014 – March 2015 with March 2015 - March 2016 a small increase in the event density is seen in the center of the field, while there is a decrease in event density in the area around the center and the southwest part of the field.

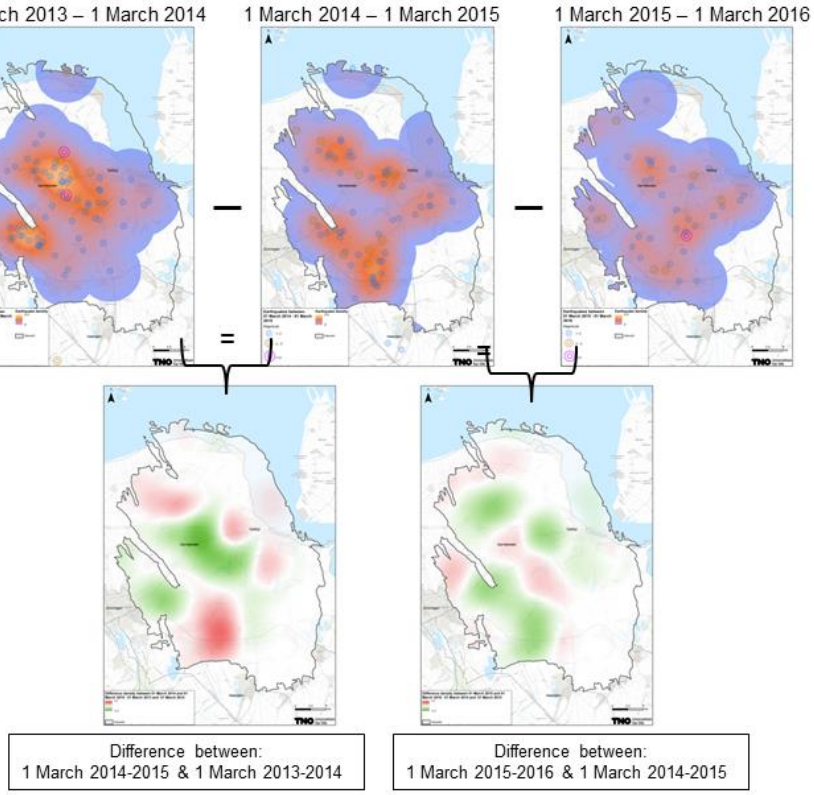

Figure 2-12 Top: Event density (number of events per km^2) 1 March 2013 to 1 March 2016 per year. The observed events and their magnitudes are indicated by the coloured small circles. Bottom: Difference in event density between the indicated periods. A negative difference (green) indicates a lower event density in the later period compared to the earlier period. A positive difference is indicated in red. Larger size figures are shown in Appendix A.

2.5 Production and seismicity: comparing 2015 to 2013

Figure 2-13a shows the total reduction in production, comparing 2015 to 2013. Production has decreased considerably in this period (from 54 bcm in 2013 to 30 bcm in 2015). Only in a small area in the southeastern part of the field production has been higher than in 2013.

Figure 2-13b shows event density comparing 2015 to 2013. The event density has decreased, especially in the center of the field. Slight increases are visible in the southwest and the very north. These increases are small (~0.1 event per km^2) and are caused by just a couple of events.

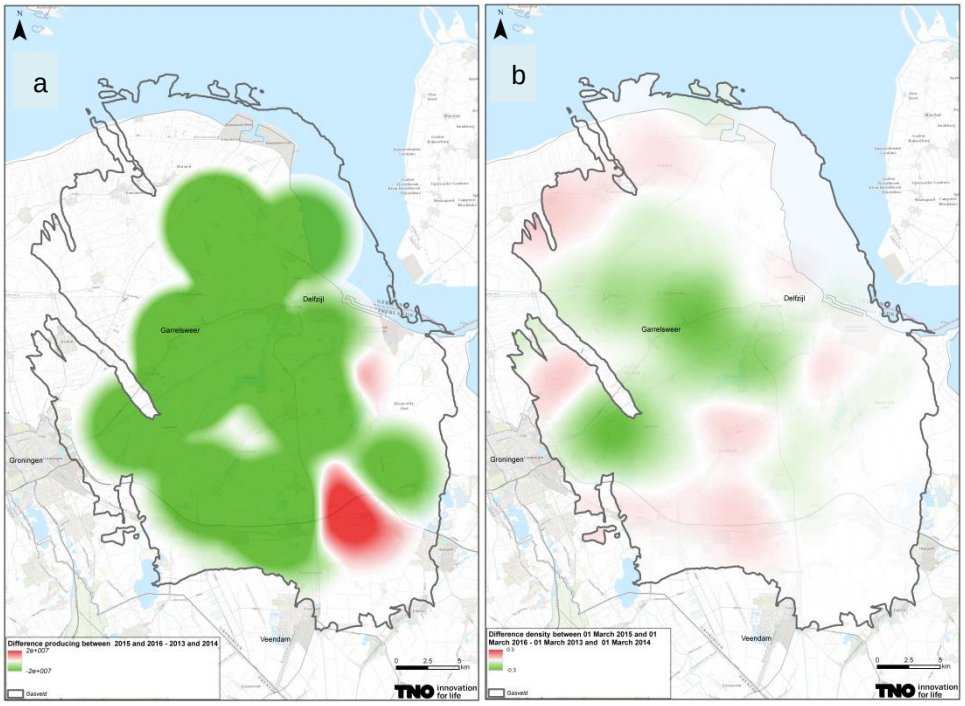

Figure 2-13a. The difference in production between 2015 and 2013 and b. The difference in event density in 2015 and 2013. Green indicates a lower level in 2015 compared to 2014, red a higher level.

3 Statistical data analysis

3.1 Magnitude of completeness of the Groningen field in the period 1995 to 2014

The ability to identify significant changes in event rates depends to a great extent on the size of seismic catalogue available for the statistical analysis.
To size of a catalogue for a fixed time interval depends on the magnitude of completeness. This is a threshold magnitude, above which it is assumed that all events are detected by the monitoring network. To maximize the catalogue size it is therefore important to determine a lower bound on the magnitude of completeness for the network.

The KNMI borehole geophone network for the monitoring of induced seismicity in the north of the Netherlands has been in operation since 1995. The network was initially designed to locate at least all earthquakes that could possibly be felt by the local population, i.e., earthquakes with local magnitudes of $M_L \geq 1.5$. The magnitude of completeness of the network has subsequently always been estimated at $M_{LC}=1.5$ (Dost, Goutbeek, van Eck, & Kraaijpoel, 2012). The initial network configuration contained 7 stations, with only one station on the Groningen field (see Figure 3-1). In the period 2009/2010 three more borehole stations were added (see Figure 3-2), to the northern Netherlands network, of which only one is on the Groningen field itself.

The catalogue of events and associated phase readings recorded on the network provides the empirical basis for a probabilistic analysis of the catalogue completeness, as explained in detail in Appendix B.
The results of the probabilistic analysis for the magnitude of completeness are shown in Figure 3-1 and Figure 3-2, for the periods before and after 2010 respectively. In the latter case the magnitude of completeness is estimated at 1.3 for the entire field, and at 1.2 for the most active areas.

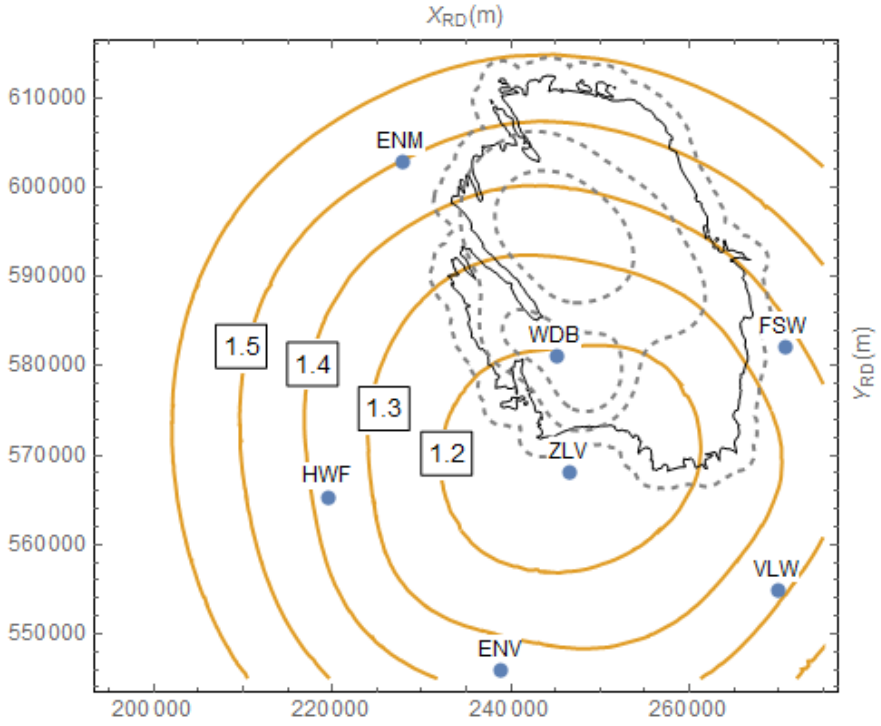

Figure 3-1. Magnitude of completeness contours for the Groningen borehole network in the period 1996-2010, based on a probabilistic model for event detection. Magnitude of completeness is defined to be the lowest magnitude that has a 95% probability of being detected in 3 or more borehole stations.

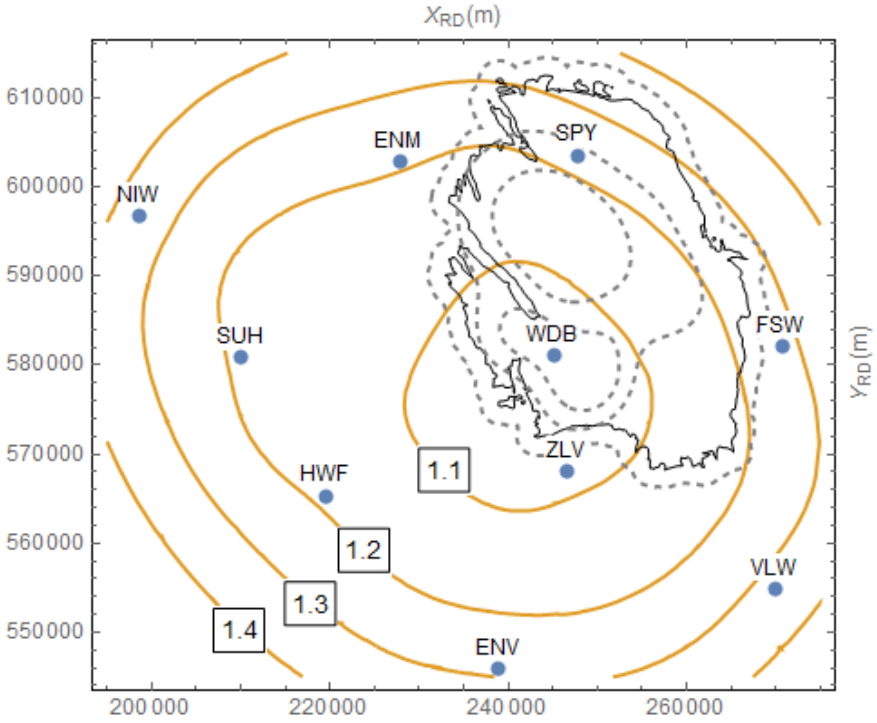

Figure 3-2 Magnitude of completeness contours for the Groningen borehole network in the period 2010-2014, based on a probabilistic model for event detection. Magnitude of completeness is defined to be the lowest magnitude that has a 95% probability of being detected in 3 or more borehole stations.

3.2 Bayesian change point analysis

Change point models are used to detect changes in rates of recorded seismic events. They have been used previously on the change in the seismicity rate for Oklahoma, U.S. (Gupta and Baker 2015) and for Groningen (TNO 2014b, 2015a, b). The unknown parameters in this model are the date of change in seismicity, the event rate before the change and the event rate after the change. In this section Bayesian statistics are performed for the seismicity data up to March 2016. The findings on the changes in seismicity rate of TNO (2014b, 2015a, b) are also listed (part of Table 3-1) and used for the further analysis.

Events catalogue
The events catalogue was obtained from the KNMI (http://www.knmi.nl/kennis-en-datacentrum/dataset/aardbevingscatalogus on 1st of March 2016).
For the update of Bayesian change point analysis all seismic events with a magnitude (M_L) larger than 1.0 within the contours of the Groningen field were selected (as in TNO 2015a, b). Furthermore, since magnitude of completeness for the entire Groningen field (Figure 3-1) is 1.3, Bayesian change point analysis is also performed for that catalogue (see Figure 3-6).

The catalogue was declustered using the algorithm of Reasenberg (1985). This is a deterministic algorithm, where each event is classified either as a mainshock or as an after- or foreshock. The method identifies aftershocks by linking events to clusters according to spatial and temporal interaction zones. The temporal zone is based on Omori's law (for example Schcherbakov, 2004), while the spatial zone depends on the stress distribution near the mainshock. A declustered catalogue only shows the independent events (i.e. no aftershocks). This is very important since Bayesian statistics is only valid for Poisson processes (i.e., not related events).

Seismicity rate estimations
Probability of k events until time t is given by:

$$P(N(t) = k) = \frac{m(t)^k}{k!} e^{-m(t)} \text{ with } m(t) = \int_0^t \lambda(\tau) d\tau$$

When λ is independent of time we find the commonly used Poisson distribution; the Poisson process is said to be stationary. If λ is dependent on time, the Poisson process is called non-stationary.

The models we compare in the Bayesian change point analysis are stationary (Poisson process is stationary): the event rate is constant and it is not a function of time. For the Bayesian change point analysis two models are compared: one has a constant event rate during the entire observed time period T= [0,t], while the other model has a constant rate before the change point and a different, constant rate after the change point.

As explained previously in TNO (2014b, 2015a, b), there is an indication that event rate increases with time in Groningen, at least in the period 2003 - 2014. In the case of an increasing event rate (for example, Figure 3-1b), the Bayesian change point model will find a change point with a constant rate before and after (Figure 3-1) depending on the time interval. To check whether we are dealing with the situation

in Figure 3-3a or the situation in Figure 3-3b in which a third model with the rate depending on time (exponentially) would be more appropriate, we will perform the Bayesian point change analysis for different time intervals. Investigating various time intervals (that differ in length, starting and ending date) will give many different change points and stationary models with different constant rates in case the third model (Figure 3-3b) is indeed more appropriate than the other two.

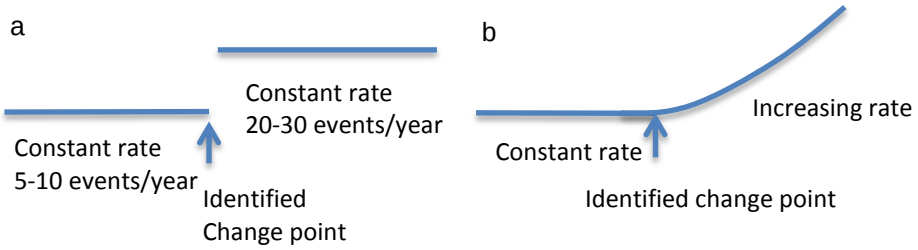

Figure 3-3a. Illustration of the Bayesian change point analysis in the case of a single step increase in event rate and (b) a gradually increasing event rate with time, as can be seen in the seismicity catalogue for Groningen. In case situation (b) occurs in reality, the Bayesian Change point model will find situation (a) for a single time window.

Results

Table 3-1 shows the results of the Bayesian change point analysis for different time intervals. For each time interval the Bayesian change point analysis tries to find a change point (CP), an event rate before the change point (pre rate) and an event rate after the change point (post rate). Also indicated is the Bayes factor where the proposed Change Point Model is compared to a constant-rate model over the whole period. A high Bayes factor (say, higher than 10, but for a truly decisive evidence about 100) indicates that the Change Point Model is more plausible than the constant-rate model. If the Bayes factor is up to 3, the evidence is considered inconclusive (Jeffreys, 1961).

In Figure 3-4, the results of this Bayesian change point analysis for several time intervals are summarized. At the center of each time interval the, most likely, event rate (pre or post rate belonging to that interval) is indicated. For example: in the first time interval (T_0) from Table 3-1 the event rate before the change point (9 events per year) is shown at the center (June 1999) of the time interval from the start time (January 1996) to the time of the change point (December 2002). The event rate after the change point (23 events per year) is shown at the center (June 2003) of the time interval from the time of the change point (December 2002) to the end of the selected time interval (January 2004). In this way 19 time intervals are obtained. The exponential fits in Figure 3-4 are meant as illustration. The fits are made without taking into account uncertainties of the change point, the pre and post event rates and the length of the time windows.

Conclusions

From Figure 3-4 it is evident that event rate has increased up to 2013. After 2013 the event rate is rapidly decreasing.

The first change point is identified in December 2002. The time accuracy of this change point is about one month. The last change point after which the event rate is still increasing is October 2008. The latest change point in May 2014 reveals that the event rate has significantly decreased.

Table 3-1. Overview of investigated time intervals and the resulting change points in event rate. The Bayes factor determines the odds of a change point model over one single constant rate model. Table includes results from TNO 2015b. Results highlighted in red are further elaborated in section 3.2.1.

Time interval	Pre rate (events/year)	Change point (CP)	Post rate (events/year)	Bayes factor
T_0: 1996 - 1.1.2004	~ 9	Dec 2002	~ 23	79
T_1: 1996 - 1.1.2011	~ 9	Dec 2002	~ 28	$5*10^{11}$
T_2: 1996 - 1.1.2012	~11	Oct 2004	~ 32	$1*10^{18}$
T_3: 1996 - 1.1.2014	~12	Jan 2005	~44	$1*10^{31}$
T_4: 1996 - 5.9.2015	~16	Oct 2008	~51	$1*10^{38}$
T_5: 15.11.2012 - 05.09.2015	~73	May 2014	~47	15
T_6: 1991 - 1.1.2012	~9	Dec 2002	~ 32	$3*10^{26}$
T_7: 1991 - 1.1.2014	~11	Jan 2005	~40	$6.*10^{44}$
T_8: 1991 - 1.3.2016	~11	Jan 2005	~42	$7*10^{54}$
T_9: 1996 – 1.3.2016	~16	Oct 2008	~49	$4*10^{37}$
T_{10}: 15.11.2012 - 01.03.2016	~73	May 2014	~44	200

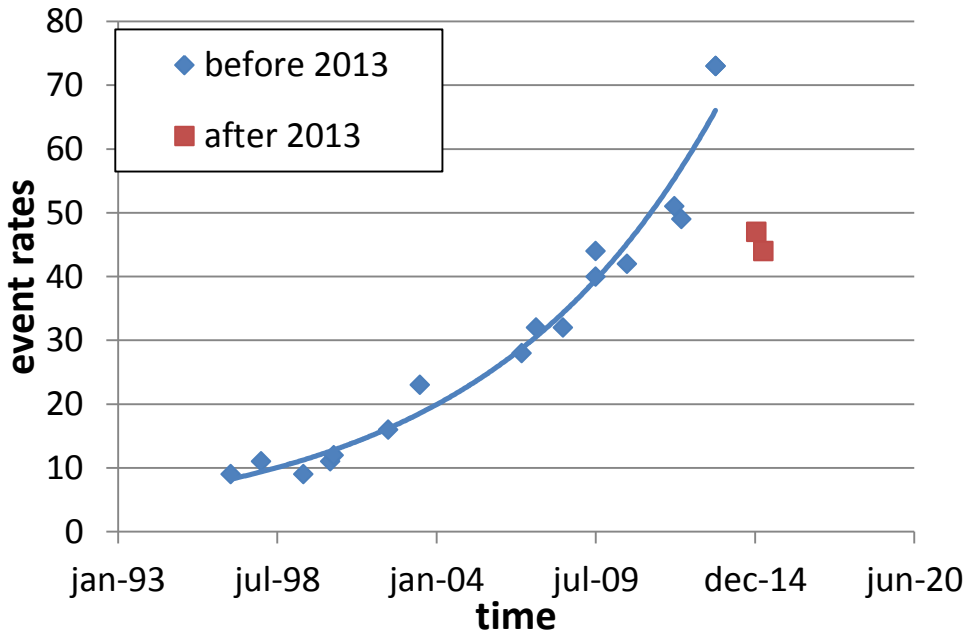

Figure 3-4. Event rates ($M_L \geq 1.0$) change with time for the entire Groningen field. The solid lines are the exponential fits trough the data before and after 2013. The data are shown in Table C-1 in Appendix C. The exponential fits are made through the data before and after 2013. However, the fits have been made without taking into account uncertainties and, thus, cannot be used to make conclusions on event rates for the Groningen field.

Discussion

The Bayesian change point analysis supports the earlier observation that event rates for the total Groningen field have been increasing after 2002 and decreasing after 2014 (TNO 2015a,b). It is noted that the Bayes factors reported indicate that in

all cases the Change Point Model is strongly favored over the model without any change in event rate.

3.2.1 Change point in May 2014

Results highlighted in Table 3-1 are further elaborated in this section. Gas production in the central part of the Groningen field has been reduced since January 2014. In this paragraph we analyze the result of the latest detected change point (for events of magnitude above 1.0, Table 3-1) to see whether seismicity has changed significantly since January 2014.

For the time interval T_5 (November 2012 to September 2015) investigated in (TNO 2015b), a change point was found in May 2014 (with the uncertainty of ~2 months). For this change point, a decrease in seismic event rate was found (TNO 2015 b, figure 3-5). The event rate before May 2014 is around 73 events per year and decreases to about 47 events per year after this change point.

The probability densities of the pre and post rate overlapped in TNO (2015b), indicating that this difference in event rate was (perhaps) not significant yet. Using the updated seismicity data until March 2016 (T_{10}: November 2012 to March 2016), the same change point is identified (May 2014). For this change point, the Bayes factor has increased from 15 to 200: the Change Point Model is even more favored over the constant-rate model than before. The event rate before May 2014 is 73, similar to TNO (2015b), but it decreases to about 44 events per year after the change point. The probability densities of the pre and post rate have moved apart and only overlap for 7% (Figure 3-5). Figure 3-5b shows the probability distribution of the change point in time. In comparison to the other identified change points this probability distribution is still broader, ranging from March 2014 to July 2014, with the highest peak in May 2014.

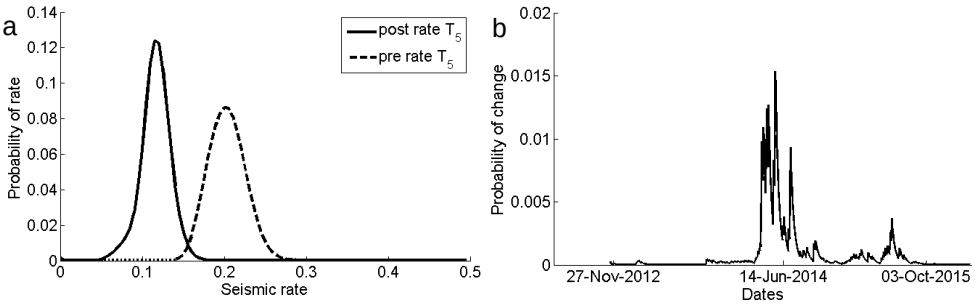

Figure 3-5a. Probability density functions for the pre change date event rate (in events/day) – dashed line and the post change date event rates (in events/day) for the change point of May 19th 2014 and (b) The probability density function of the change point in time over the period of 2012 up to now (March 2016).

Note: the probability density function of change point time (in Figure 3-5b) is calculated from the marginal posterior distribution of change time, and converted to probability by dividing the values for each day by the sum of values for all days in the observation period, such that the sum of probabilities equals one. The values of probabilities per day are rather small but this does not make the result statistically less significant.

3.3 Influence of the magnitude of completeness in Groningen

According to the magnitude of completeness analysis (section 3.1) the magnitude of completeness for the Groningen field is M_C=1.3. Since the Bayesian change point analysis has taken into account magnitudes (M_L) larger than or equal to 1.0, which is below Mc, the influence of this on the results of the Bayesian Change Point analysis has to be analysed.

3.3.1 Events catalogue

The declustered seismic catalogue for M_L≥1.0 is shown in Figure 3-4a, the declustered seismic catalogue for M_L ≥1.3 is shown in Figure 3-4b. As can be seen, the number of events is significantly smaller if only events with magnitudes larger than or equal to 1.3 are considered. Also, the decrease in number of events from 2014 is less visible. Note that 2016 is shown only with the number of events in the first two months of the year (January and February 2016).

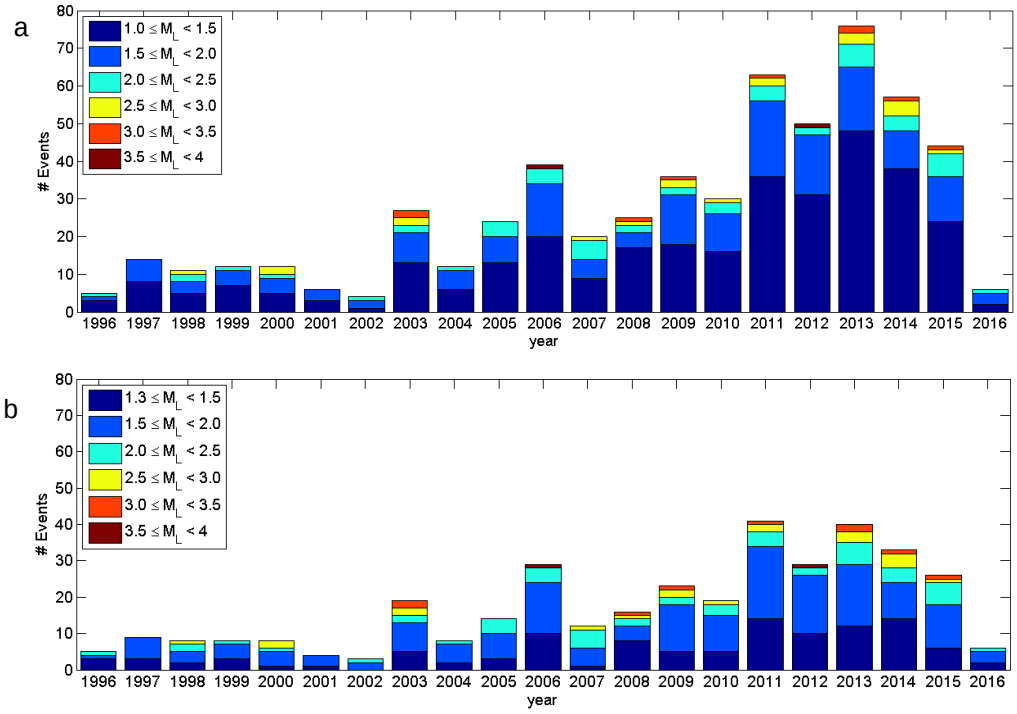

Figure 3-6a. Histogram of declustered seismic data for Groningen field and events M≥1.0 and b. for declustered seismic data for the Groningen field and events M≥1.3.

3.3.2 Results and Discussion

Due to the low number of seismic events with M_L≥1.3 the Bayesian change point analysis for the entire Groningen field could not identify a change point at the beginning of 2014. For a patch in the centre of the field (where production is decreased), using a radius of 10 km where the magnitude of completeness is 1.2 (M_c=1.2) (section 3.1), a change point is identified in April 2014. The event rate before the change point is around 37 events per year (with magnitudes larger than or equal to 1.2), while the event rate after the change point declines to about 20 events per year (with magnitude larger than or equal to 1.2). The Bayes factor for

this change point is 16, which is lower than the analysis for magnitudes $M_L \geq 1.0$ but still significant.

Table 3-2. Overview of investigated time intervals and the resulting change points in event rate for events of $M_L \geq 1.3$. The Bayes factor determines the odds of change point model above one single constant rate model. The latest investigated time interval includes only events in 10 km radius around central point (latitude 53.297 and longitude 6.782) in the Loppersum area with magnitudes $M_L \geq 1.2$, since this is the magnitude of completeness for this area (section 3.1).

Time interval	Pre rate (events/year)	Change point (CP)	Post rate (events/year)	Bayes factor
T_1: 1991-1.1.2006	~5.8	Jan 2003	~8.5	544
T_2: 1996-1.1.2011	~7	Jan 2003	~18	$6*10^6$
T_3: 1.1.2001-1.1.2014	~14.3	Jan 2011	~33	$9*10^8$
T_4: 1991 - 1.3.2016	~7.3	Jan 2006	~25.5	$4*10^{30}$
T_5: 1996 - 1.3.2016	~8.4	Jan 2006	~26	$3*10^{19}$
T_6: 1.1.2001-1.3.2016	~14	Jan 2011	~30	$2*10^{10}$
T_7: 15.11.2012-1.3.2016	~37*	April 2014	~20*	16

*10km radius and $M_L \geq 1.2$

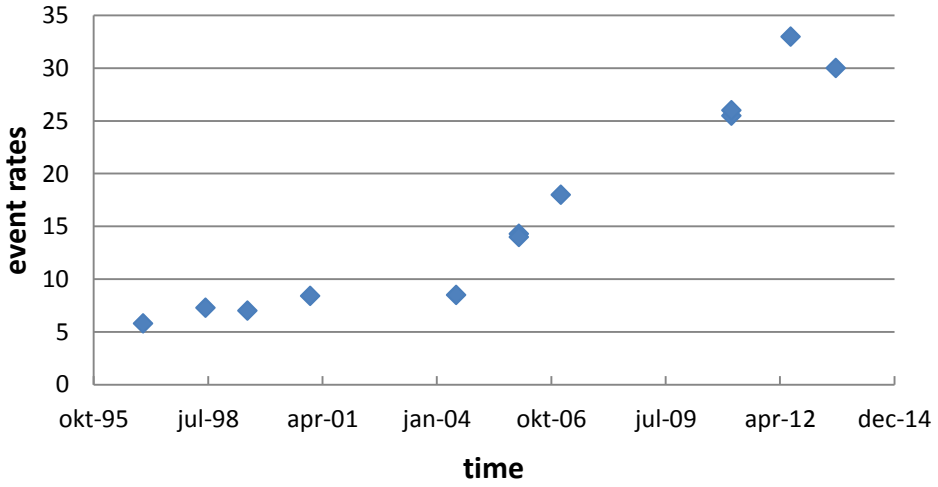

Figure 3-7. Event rate change with time for the entire Groningen field and all magnitudes above 1.3. The data are shown in Table C-2 in Appendix C.

Figure 3-7 summarizes the Bayesian analysis of Table 2-2. For events with magnitudes larger than or equal to 1.3, the exponential growth of the events rate with time is clearly visible. Although Bayesian Change Point analysis has not been

able to detect any change point after 2014 for $M_L \geq 1.3$, the decreasing trend is still visible. Comparing the event rates after the change point for time intervals T3 and T6 shows that including recent data (up to March 2016) has lowered the event rate from 33 events per year to 30 events per year with a magnitude larger than or equal to 1.3.

4 Compaction as a proxy for seismicity

In this chapter compaction is examined with regard to its use as a proxy for the occurrence of seismicity in the Groningen field (NAM 2013). Recent insights (TNO 2015b) have indicated that the presence of faults is more important than thought earlier. To examine the use of compaction as proxy for seismicity a geomechanical model is used which examines the stresses on the faults in the reservoir.

Introduction

Reduction of pressure in the reservoir causes compaction as well as changes in stress on faults in the reservoir (Figure 4-1). Reservoir compaction leads to subsidence at the surface. Changes in stress on faults lead to seismic events. It is technically more feasible to compute compaction which is why reservoir compaction has been used as a proxy for the occurrence of seismic events in Groningen (NAM 2013, TNO 2013). However, as indicated in TNO (2015b, c) the presence of faults is more important for the seismicity than compaction. This was first substantiated by the difference between the pattern of seismicity and the compaction pattern over the field in TNO (2015b).

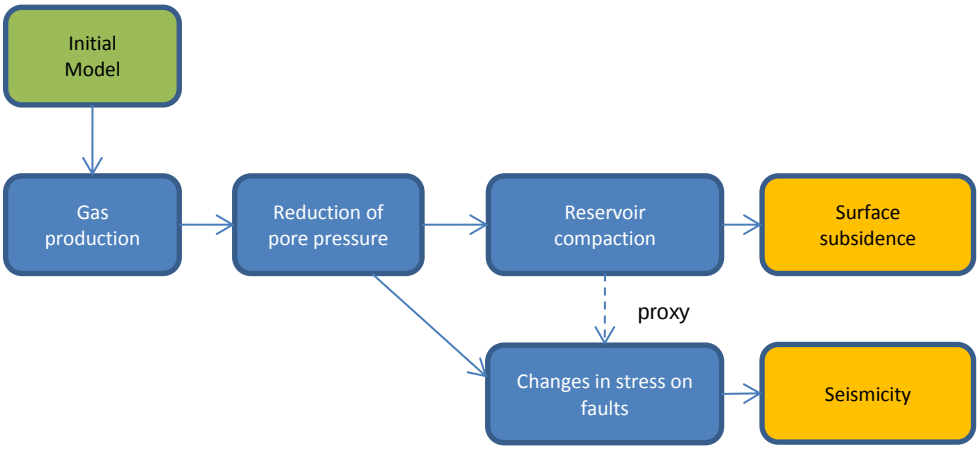

Figure 4-1. Schematic of the relation between gas production and seismicity

In TNO 2015c it was concluded that the effect of existing production measures (in particular those of January 2014) on seismic events has resulted in a decreased rate of seismic events in the center of the field in the period 2014 to September 2015. This was based on the agreement between observations, statistical tests and geomechanical modelling. The compaction models with time dependent compaction could not explain these observations.

Geomechanical modelling

In Appendix D the use of reservoir compaction as a proxy for the occurrence of seismicity is investigated using geomechanical modelling. This appendix was submitted in December 2015 as an article to the Journal of Geophysical Research: Solid Earth.

Results

Geomechanical models, using time-dependent compaction, predict that the relationship of compaction and seismicity breaks after a production stop. Indeed, the seismic moment is in the order of 3 to 10 times less than the values predicted by Bourne et al. (2014) where an observational relation between seismic moment and compaction is used. As such, the model supports low seismicity observed in the central area of the Groningen Field, where production has been reduced by 80%, since January 17 2014.

Findings

Time-dependent compaction models thus fit the observed subsidence (TNO 2013) but cannot explain the occurrence of seismicity. Linear compaction models, on the other hand, do not fit the observed subsidence, but can explain the occurrence of seismicity due to their instant reaction to a production change. After, for example, a production stop, linear compaction models will cease compaction immediately. Hence, if this form of compaction is used as a prediction for the occurrence of seismicity, the relation of Bourne et al. (2014) will predict immediate cessation of seismicity. In the, more recent, strain thickness model (Bourne and Oates, 2015), compaction is still used as a proxy but offsets are taken into account as well. The resulting seismic moment will, therefore, also be overestimated in case a time dependent compaction model is used.

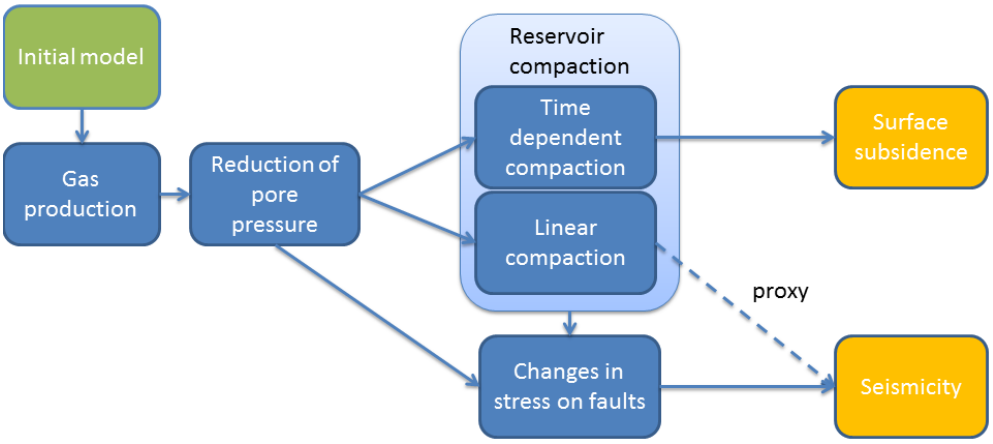

Figure 4-2 Improved schematic of the relation between gas production and seismicity

In conclusion, instead of Figure 4-1 an improved schematic can be made in Figure 4-2, where time dependent compaction can explain the surface subsidence and linear compaction can be used as proxy (Bourne et al., 2014, Bourne and Oates, 2015) to predict induced seismicity in the absence of a physical model.

The geomechanical model findings of Appendix D support scope for mitigating induced seismicity through adjusting production scenarios, as the seismicity rates are expected to be correlated primarily with rates of pressure change.

5 Findings

A production plan for the Groningen field was submitted in 2013. In 2016 submission of an updated production plan for the Groningen field is expected.

State Supervision of Mines (Staatstoezicht op de Mijnen, SodM) has requested the following technical evaluations from TNO-AGE:

- Update on production and seismicity of the Groningen field
- Update of event density maps

New results on statistics and physical understanding are to be discussed in the light of mitigation of seismic hazard of the Groningen field.

These activities have been performed within the framework of the yearly work plan for the Ministry of Economic Affairs (reference AGE 16-10.009).

Production and seismicity of the Groningen field

Some major changes in production and seismicity of the Groningen field have occurred since EZ launched a dedicated research program in 2013 (TK 2012-2013 33529, no. 2). An overview is presented of production reduction measures and trends in seismic events.

Production

Since 2014 there have been a number of production reduction measures (Table i).

Table i. Overview of production reduction measures in the Groningen field

Date	Reduction measures by the Minister of Economic Affairs
17 January 2014	○ A maximum field production of 42. bcm for 2014 ○ Maximum 3 bcm for the Loppersum clusters
December 2014	○ A maximum production of 39.4 bcm for 2015 ○ Maximum 3 bcm for the Loppersum clusters ○ Maximum 9.9 bcm for the clusters close to Hoogezand-Sappemeer for the period 1st October 2015 until 30th September 2016 ○ Maximum 2 bcm for the Eemskanaal cluster
February 2015	○ Maximum field production of 16.5 bcm for the first six months of 2015
14 April 2015	○ Limit production from Loppersum clusters to necessity for the security of supply
23 June 2015	○ Maximum field production of 13.5 bcm for the last six months of 2015
18 November 2015	○ Maximum field production of 27 bcm for the gas year 2015/2016

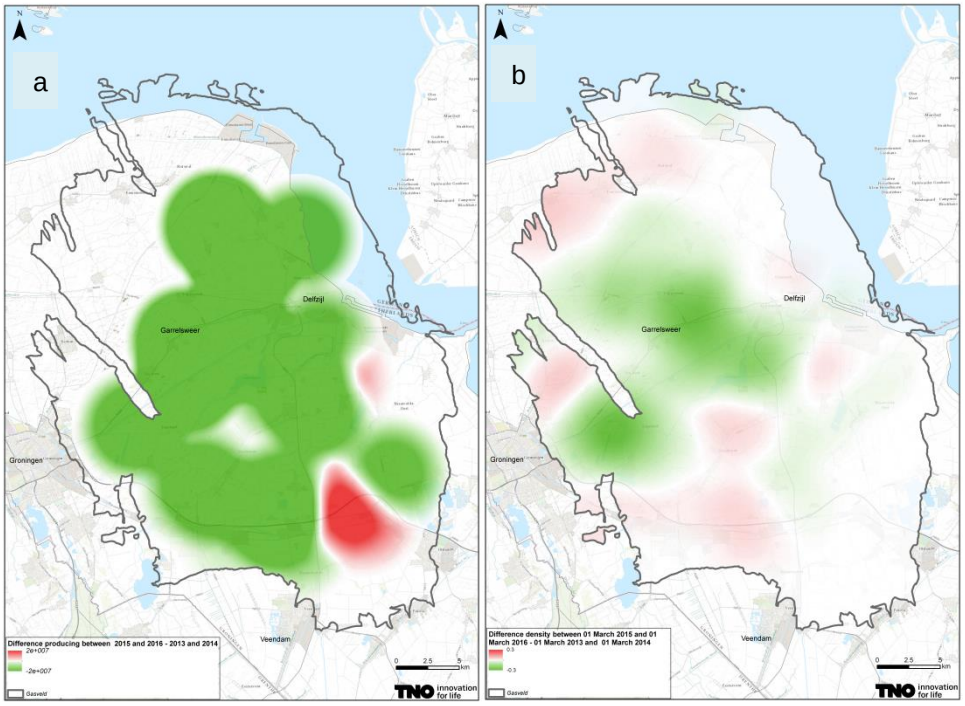

Figure i a. The difference in production between 2015 and 2013. Green indicates a lower level in 2015 compared to 2014, red a higher level, both with a maximum of $2 \cdot 10^7$ Nm^3. The red area is caused by production of Scheemderzwaag (SZW) and de Eeker (EKR). The densities were determined using a Kernel Density (standard GIS application) with a radius of 5 km and a cell size of 50 m.

b. The difference in event density between 2015 and 2013. Green indicates a lower level in 2015 compared to 2014, red a higher level, both with a maximum of 0.3 events per km^2. The densities were determined using a Kernel Density (standard GIS application) with a radius of 5 km and a cell size of 50 m.

NAM has complied with these production reduction measures. As a result production in the field has fallen considerably compared to 2013 (Figure i-a). Additionally, production has been distributed differently over the field.

Seismicity

Seismicity of the Groningen field has dropped considerably since 2013 (Figure i-b). Compared to 2013 there are less seismic events in the Loppersum area. Statistical analysis for the entire field shows a lower seismic event rate since May 2014[2]. Event rates have decreased rapidly since 2013 (Figure ii). These findings are statistically more meaningful compared to earlier studies (TNO 2015b, c).

[2] about 44 events per year with magnitudes larger than or equal to 1.0 ($M_L \geq 1.0$).

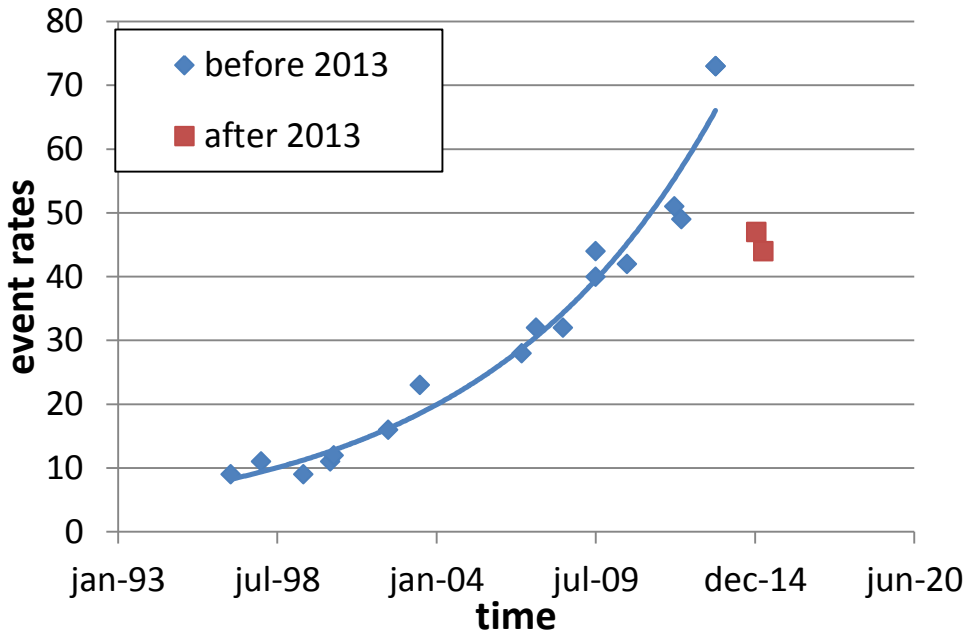

Figure ii. Event rate ($M_L \geq 1.0$) change with time for the entire Groningen field according to the Bayesian change point model results. The solid lines are meant as illustration. The exponential fits are made through the data before and after 2013. However, the fits have been made without taking into account uncertainties and, thus, cannot be used to make conclusions on event rates for the Groningen field.

Physical understanding of the cause of seismicity

In 2013 (NAM 2013), compaction was used as a first order approximation for the short term prognosis of seismicity in the Groningen field. Observations of induced seismicity since 2014, after the reduction of production in the Loppersum clusters, showed that the relation is more complex (TNO 2015b, c). Time dependent compaction models, which fit the observations of subsidence best, do not explain the drop in seismicity since 2014. Geomechanical models predict that the relationship of compaction and seismicity breaks since 2014. Consequently, time dependent compaction does not lead to additional seismicity Linear compaction models, on the other hand, do not fit the observations of subsidence, but can explain the occurrence of seismicity due to their instant reaction to a pore pressure (or stress) change (Figure iii).
In summary, compaction can be used as a proxy for seismicity, in the absence of a proper physical model and in case no significant changes (like production reduction measures) occur.

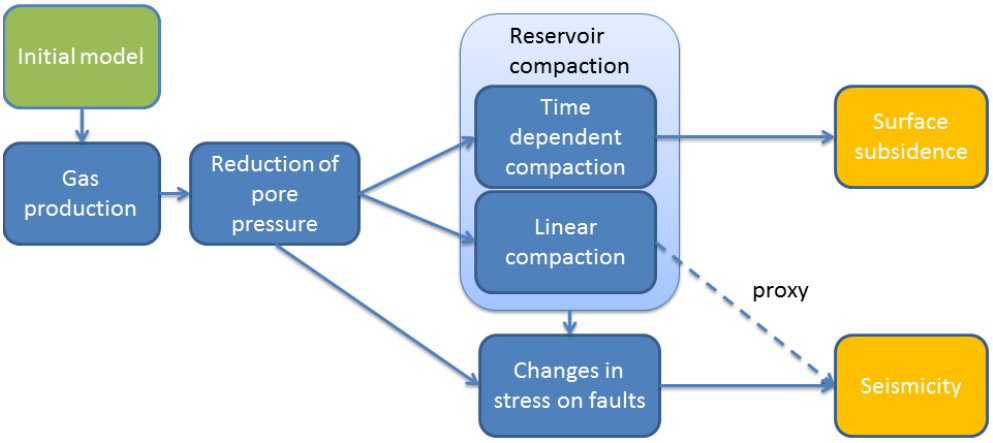

Figure iii Improved schematic of the relation between gas production and seismicity

Scope for mitigation of seismic hazard

In 2013 (NAM 2013) compaction was used as a proxy for the occurrence of seismicity for the next 2 to 3 years. There was not a clear correlation between estimated event locations and mapped faults. It was expected that any beneficial changes in seismicity due to production reduction measures would be temporary.

Now, in 2016 we have learned that seismicity is not primarily caused by compaction. Faults play a major role. Observations of seismic events recorded in borehole stations indicate that events occur on known faults (NAM 2015). Faults in the Loppersum area are likely more prone to movement caused by increasing stresses on the faults due to their favorable orientation in the stress field, in conjunction to stress changes caused by pressure reduction, compaction, geometry and geological characteristics of the fault. Improved physical understanding indicates that seismicity rates are expected to be correlated primarily to rates of pressure change. These findings support scope for mitigation of induced seismicity adjusting production scenarios.

6 References

Bourne et al., 2014 Bourne, S. J., S. J. Oates, J. van Elk, and D. Doornhof (2014), A seismological model for earthquakes induced by fluid extraction from a subsurface reservoir*, Journal of Geophysical Research: Solid Earth, 119*(12), 8991-9015, doi: 10.1002/2014JB011663.

Bourne & Oates 2015 An activity rate model of induced seismicity within the Groningen field (part 1 and part 2). NAM report July 2015.

Gupta and Baker 2015 A. Gupta, and J. Baker, A Bayesian change point model to detect changes in event occurrence rates, with application to induced seismicity, *12th international Conference on Applications of Statistics and Probability* in Civil Engineering ICASP12, Vancouver, Canada, July 12-15, 2015.

NAM 2013 Wijziging winningsplan Groningen 2013, inclusief technische bijlage Groningen winningsplan 2013. Versie 29 november 2013.

NAM 2015 M. Pickering, An estimate of the earthquake hypocenter locations in the Groningen gas field, NAM report June 2015.

Reasenberg, P. 1985 Second-order moment of central California seismicity, 1969-82, J. Geophys. Res., 90, 5479-5495.

Schcherbakov 2004 R. Schcherbakov, D.L. Turcaotte, J.B. Rundle, A gerneralized Omori's law for aftershock decay, Geophys. Res. Lett., doi: 10.1029/2004GL019808, 2004.

TNO 2013 Toetsing van de bodemdalingsprognoses en seismische hazard ten gevolge van gaswinning van het Groningen veld. TNO report 2013 R11953, 23 December 2013.

TNO 2014a Technisch rapport behorende bij "Effecten verschillende productiescenario's op de verdeling van de compactie in het Groningen veld in de periode 2014 t/m 2016". TNO report 2014 R10426, 7 March 2014.

TNO and CBS 2014 Vergelijking van statistische methoden, AGE 14-10.078, 19 november 2014.

TNO 2014b Recent developments of the Groningen field in 2014 and, specifically, the southwest periphery of the field. TNO report 2014 R 11703, 9 December 2014.

TNO 2015a Plaatsgebonden individueel risico van panden in het invloedsgebied van het Groningen veld (EN: Local individual risk of buidlings in the influence area of the Groningen field), kenmerk 0100285823, 26 mei 2015.

TNO 2015b Recent developments on the seismicity of the Groningen field in 2015. TNO report 2015 R10755, 29 May 2015.

TNO 2015c Response of induced seismicity to production changes in the Groningen field. TNO report 2015 R11367, 10 November 2015.

KNMI & TNO 2015 Notitie over Hazardkaarten (EN: Note on hazard maps). AGE 15-10.067, KNMI-2015/3209, 23 November 2015.

TNO 2015d Notitie over het Effect van productie-variaties en fluctuaties op de seismiciteit van het Groningen veld (EN: Note on the effect of production fluctuations on the seismicity of the Groningen field.) AGE 15-10.070, 30 November 2015.

7 Signature

Utrecht, 14 april 2016 TNO

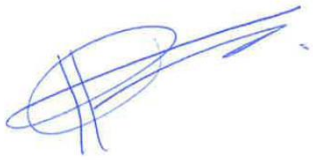

Head of department

Authors

Karin van Thienen-Visser, Danijela Sijacic, Jan-Diederik van Wees, Dirk Kraaijpoel, Joost Roholl

A Figures production and event density

In this appendix the figures from Figure 2-9, Figure 2-12 and Figure 2-13 are shown in a larger format. The figures are repeated from left to right and top to bottom.

A.1 Enlargement Figure 2-8

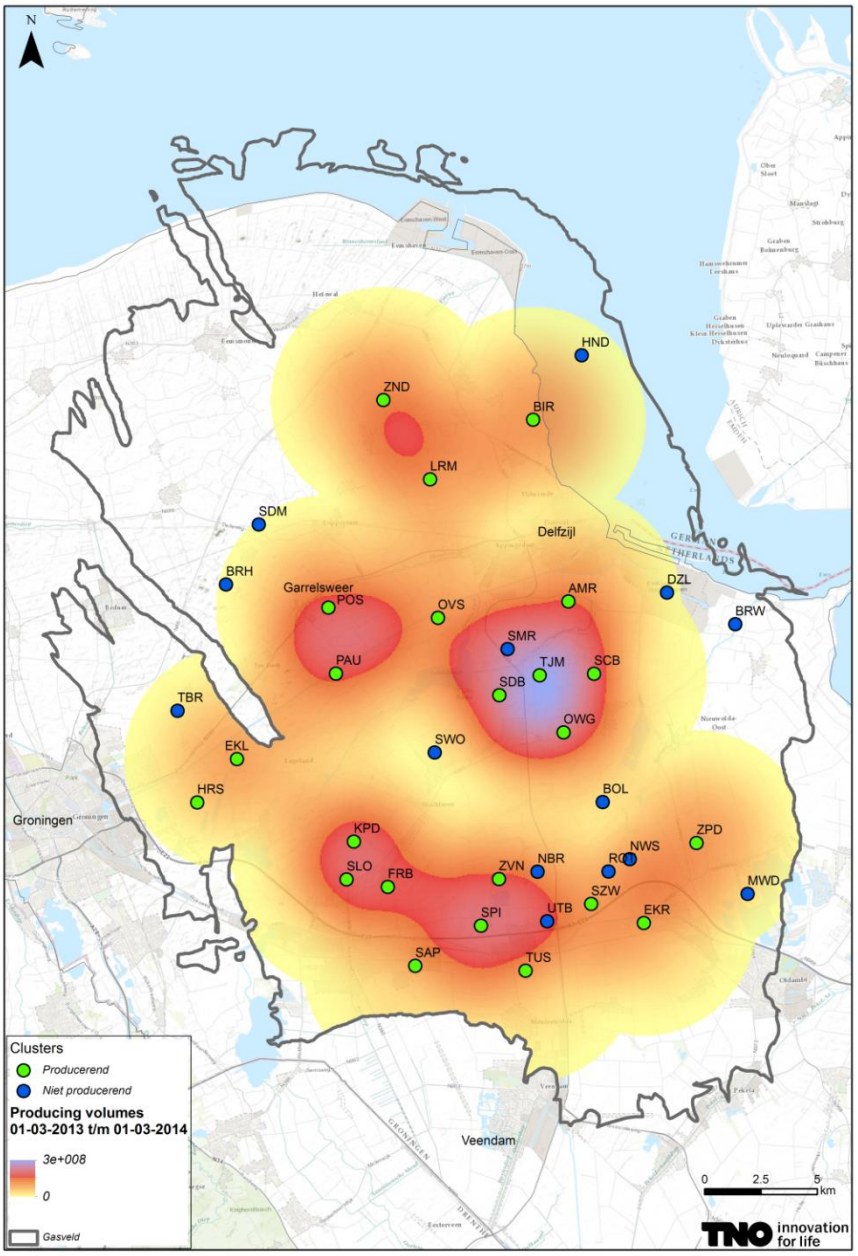

Figure A-1 Density of production (Nm3 per km^2) from March 1st 2013 to March 1st 2014. The densities were determined using a Kernel Density (standard GIS application) with a radius of 5 km and a cell size of 50 m. The producing/non-producing clusters are indicated by the colored small circles (green indicates producing, blue indicates non-producing).

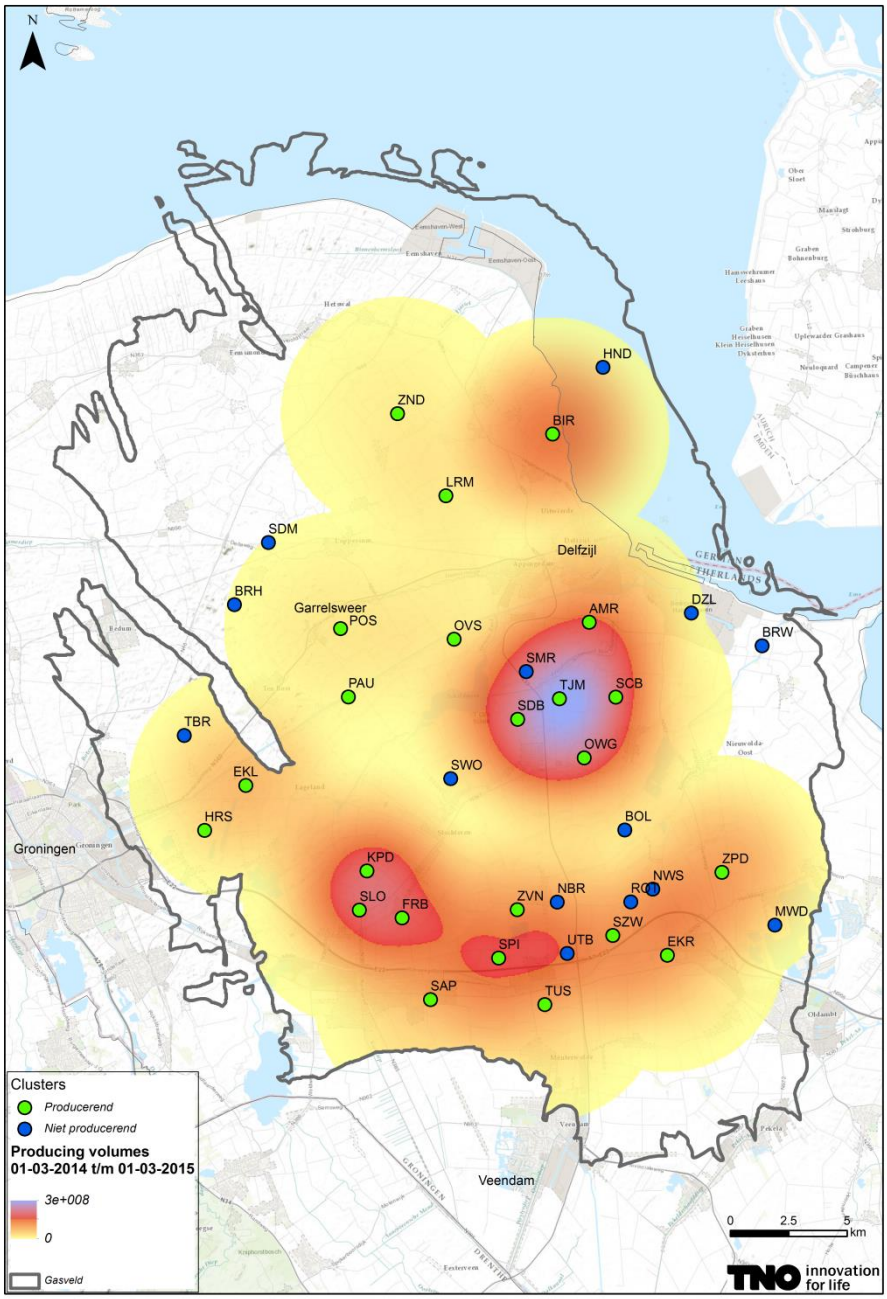

Figure A-2 Density of production (Nm^3 per km^2) from March 1st 2014 to March 1st 2015. The densities were determined using a Kernel Density (standard GIS application) with a radius of 5 km and a cell size of 50 m. The producing/non-producing clusters are indicated by the colored small circles (green indicates producing, blue indicates non-producing).

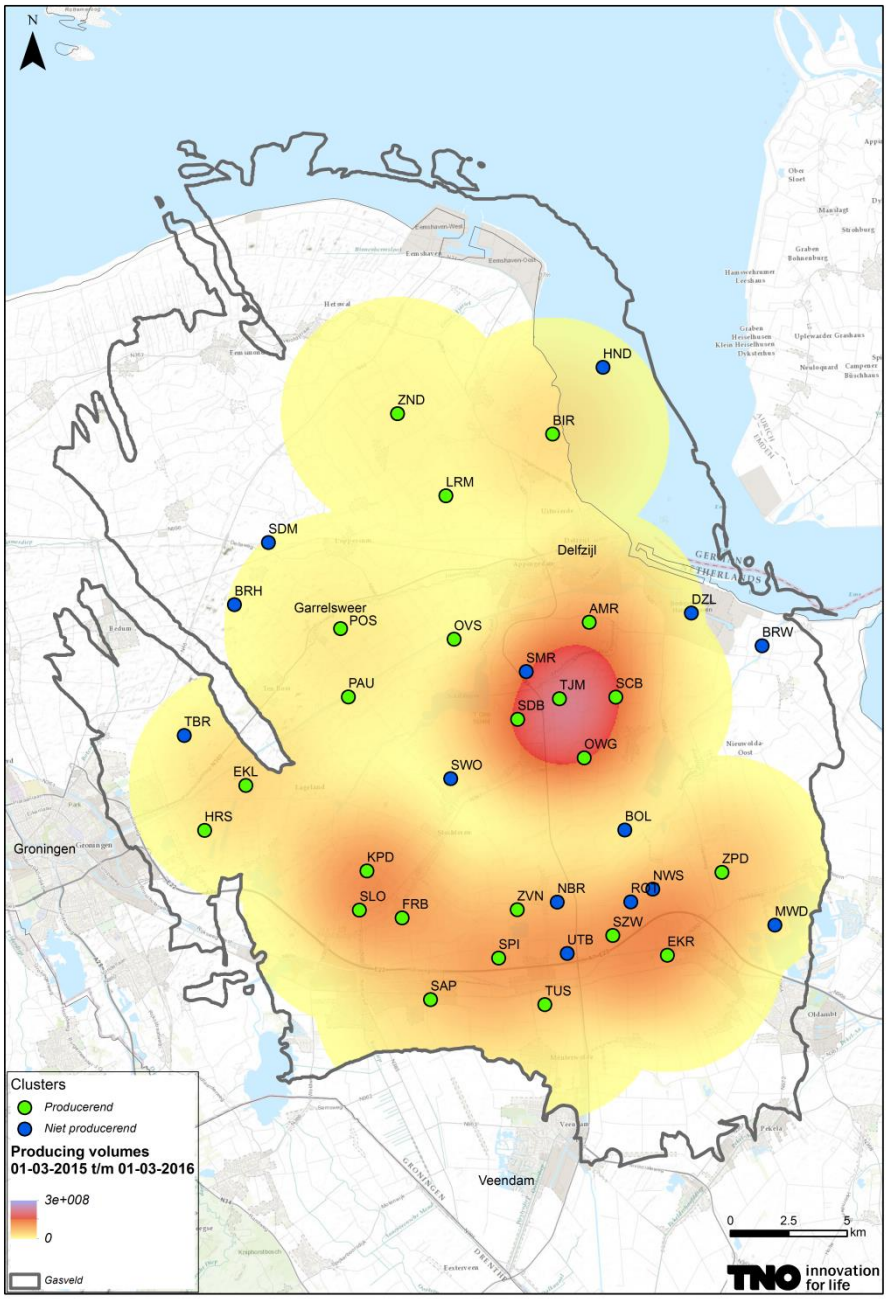

Figure A-3 Density of production (Nm^3 per km^2) from March 1st 2015 to March 1st 2016. The densities were determined using a Kernel Density (standard GIS application) with a radius of 5 km and a cell size of 50 m. The producing/non-producing clusters are indicated by the colored small circles (green indicates producing, blue indicates non-producing).

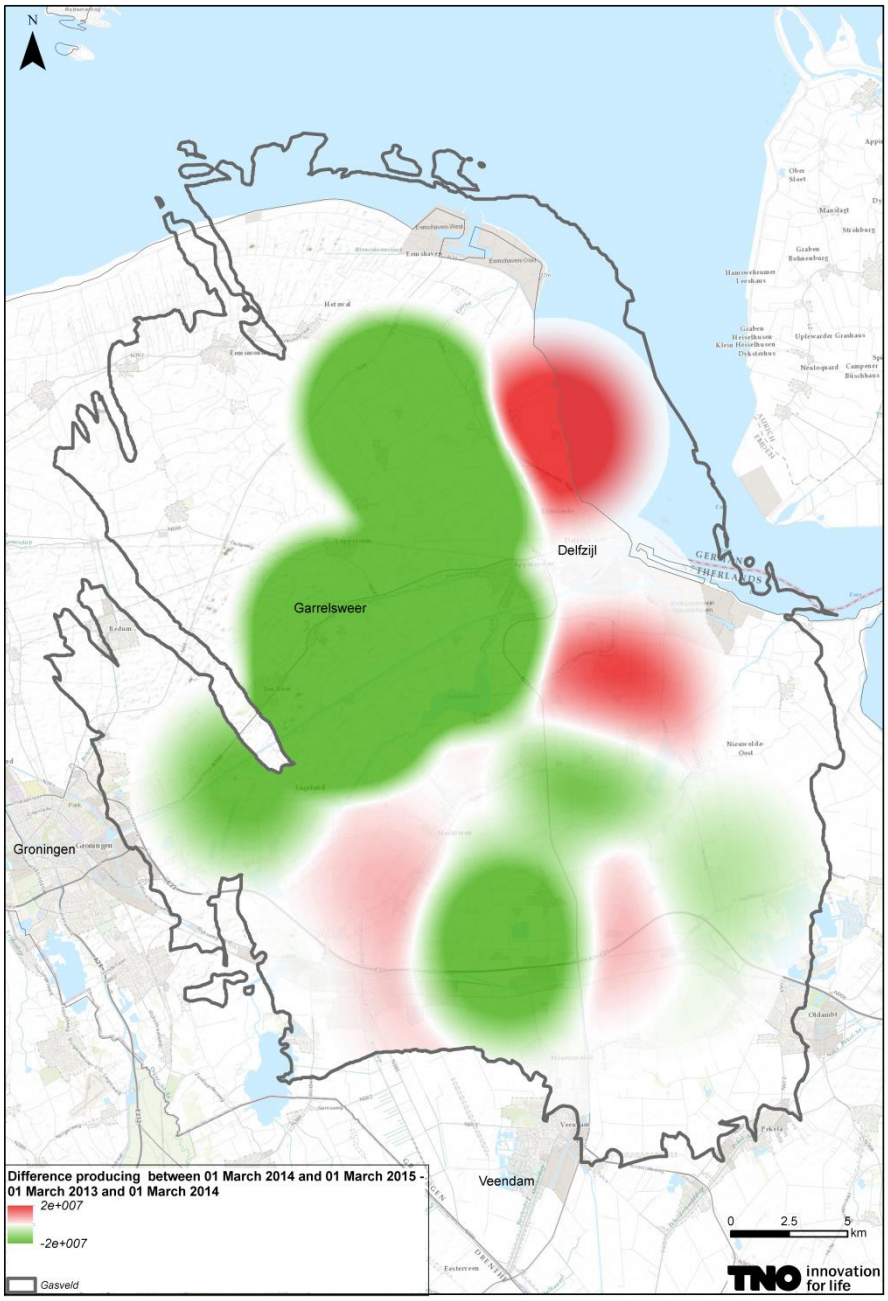

Figure A-4 Difference in production (in Nm^3 per km^2) between March 1st 2014-March 1st 2015 and March 1st 2013- March 1st 2014. A negative difference in production, shown in green, indicates a lower production between in the later period compared to the earlier period.

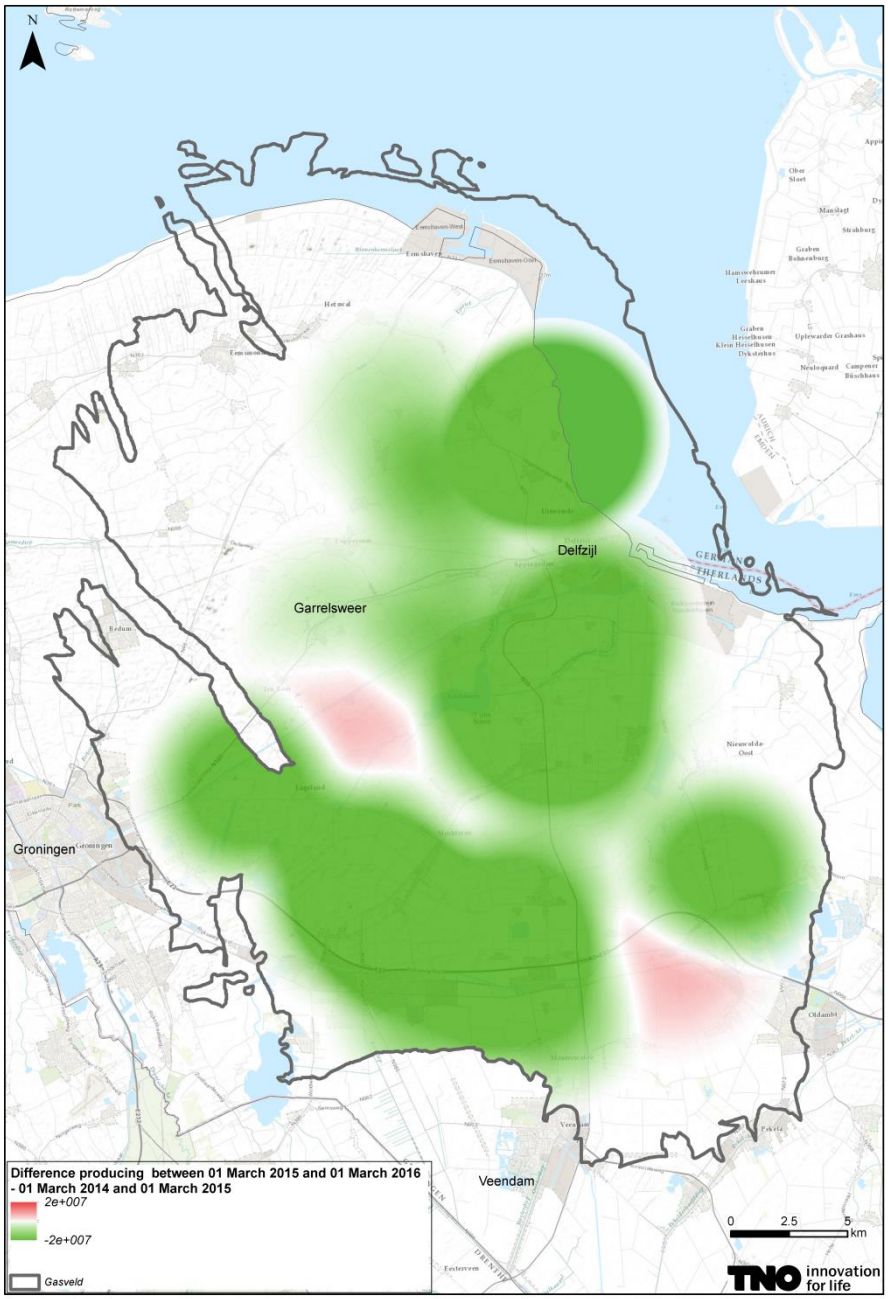

Figure A-5 Difference in production (in Nm^3 per km^2) between March 1st 2015-March 1st 2016 and March 1st 2014- March 1st 2015. A negative difference in production, shown in green, indicates a lower production between in the later period compared to the earlier period.

A.2 Enlargement Figure 2-11

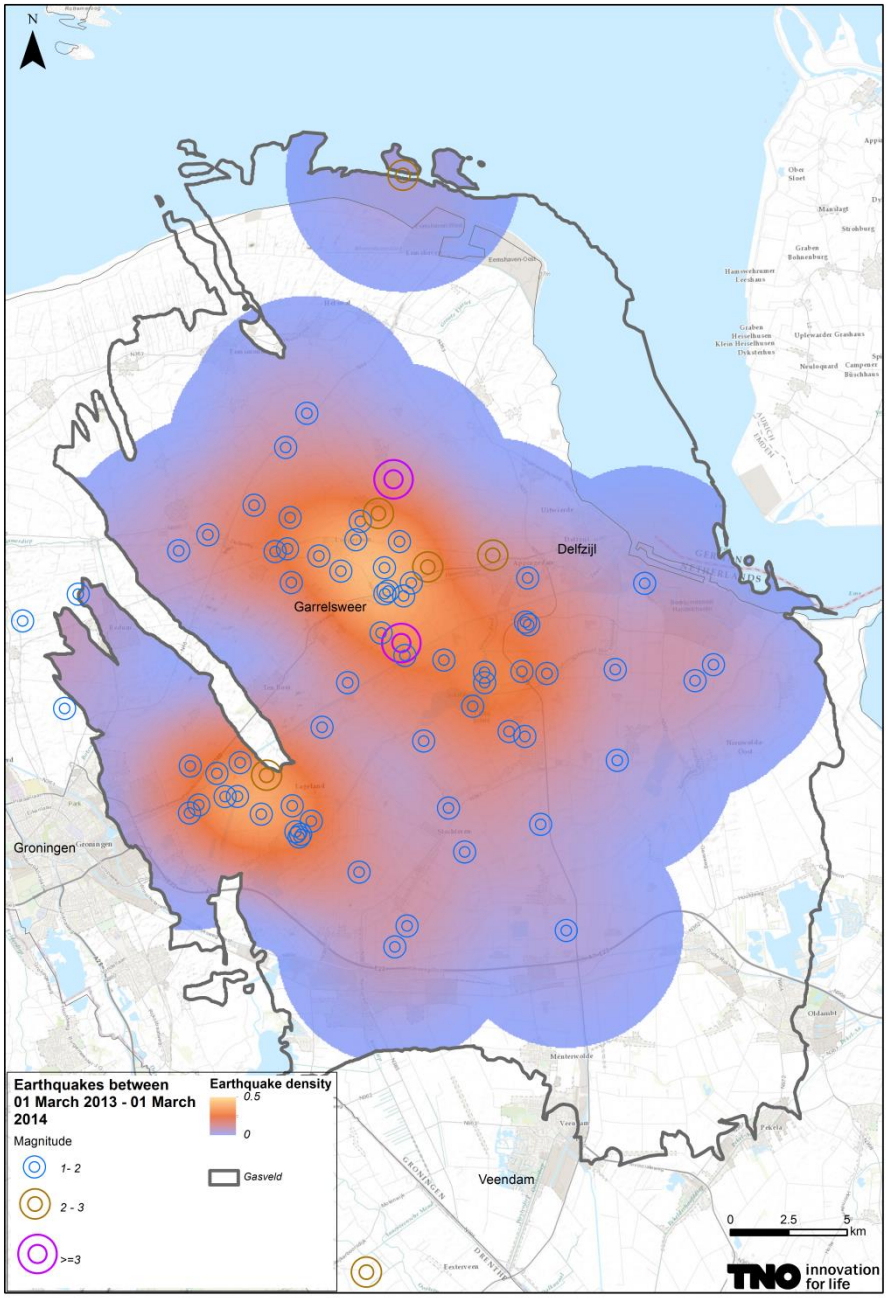

Figure A-6 Event density (number of events per km^2) March 1st 2013 to March 1st 2014 per year. The densities were determined using a Kernel Density (standard GIS application) with a radius of 5 km and a cell size of 50 m.The observed events and their magnitudes are indicated by the coloured small circles.

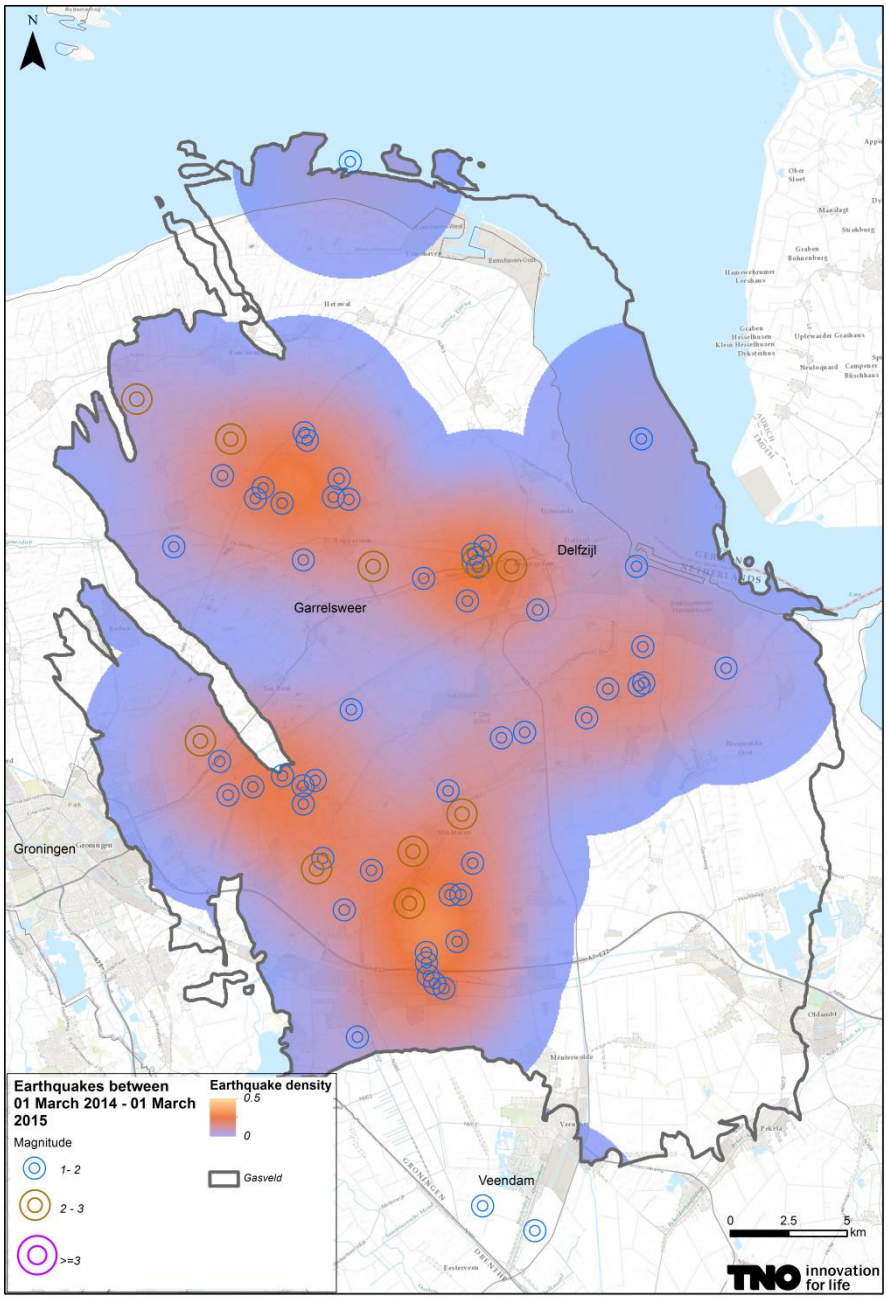

Figure A-7 Event density (number of events per km^2) March 1st 2014 to March 1st 2015 per year. The densities were determined using a Kernel Density (standard GIS application) with a radius of 5 km and a cell size of 50 m.The observed events and their magnitudes are indicated by the coloured small circles.

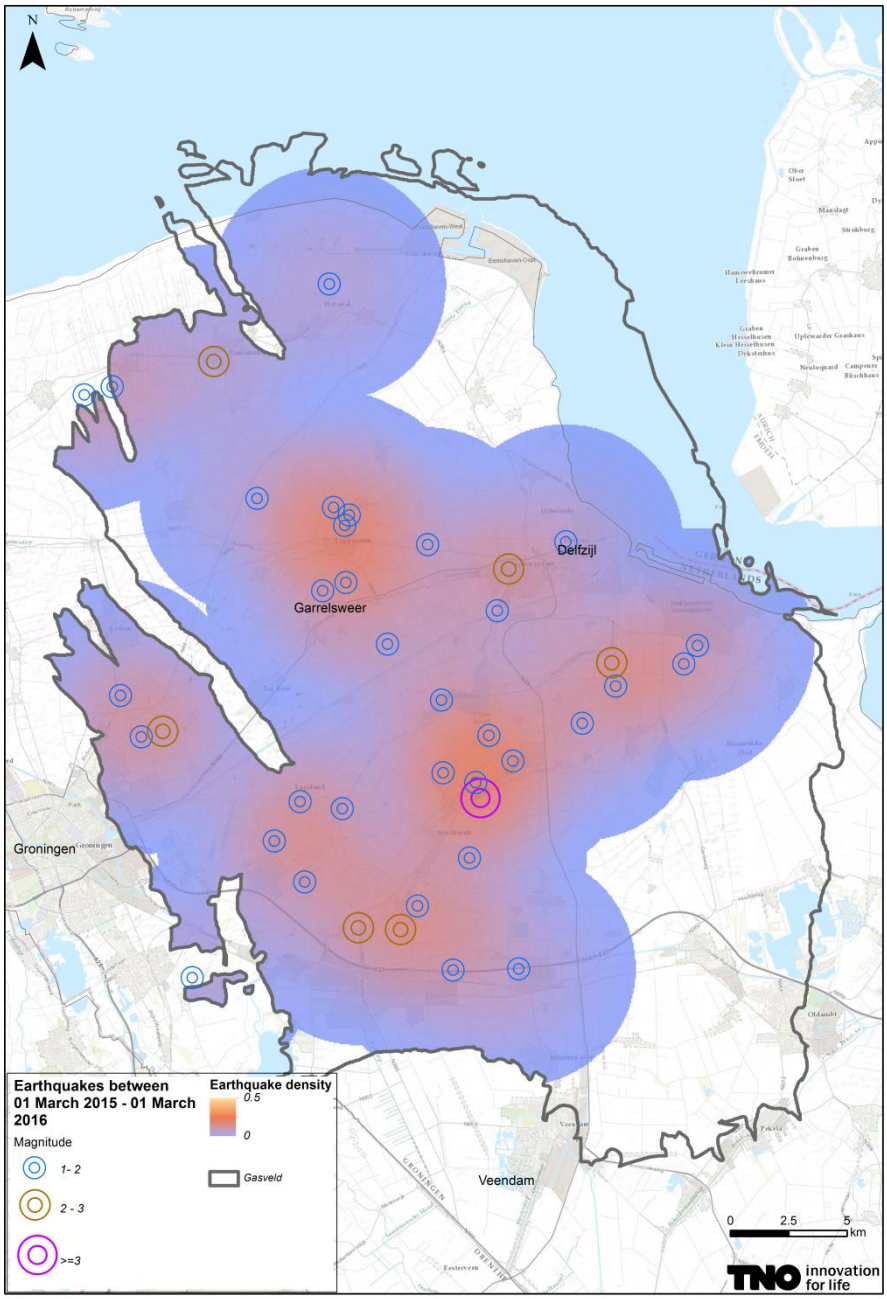

Figure A-8 Event density (number of events per km^2) March 1st 2015 to March 1st 2016 per year. The densities were determined using a Kernel Density (standard GIS application) with a radius of 5 km and a cell size of 50 m. The observed events and their magnitudes are indicated by the coloured small circles.

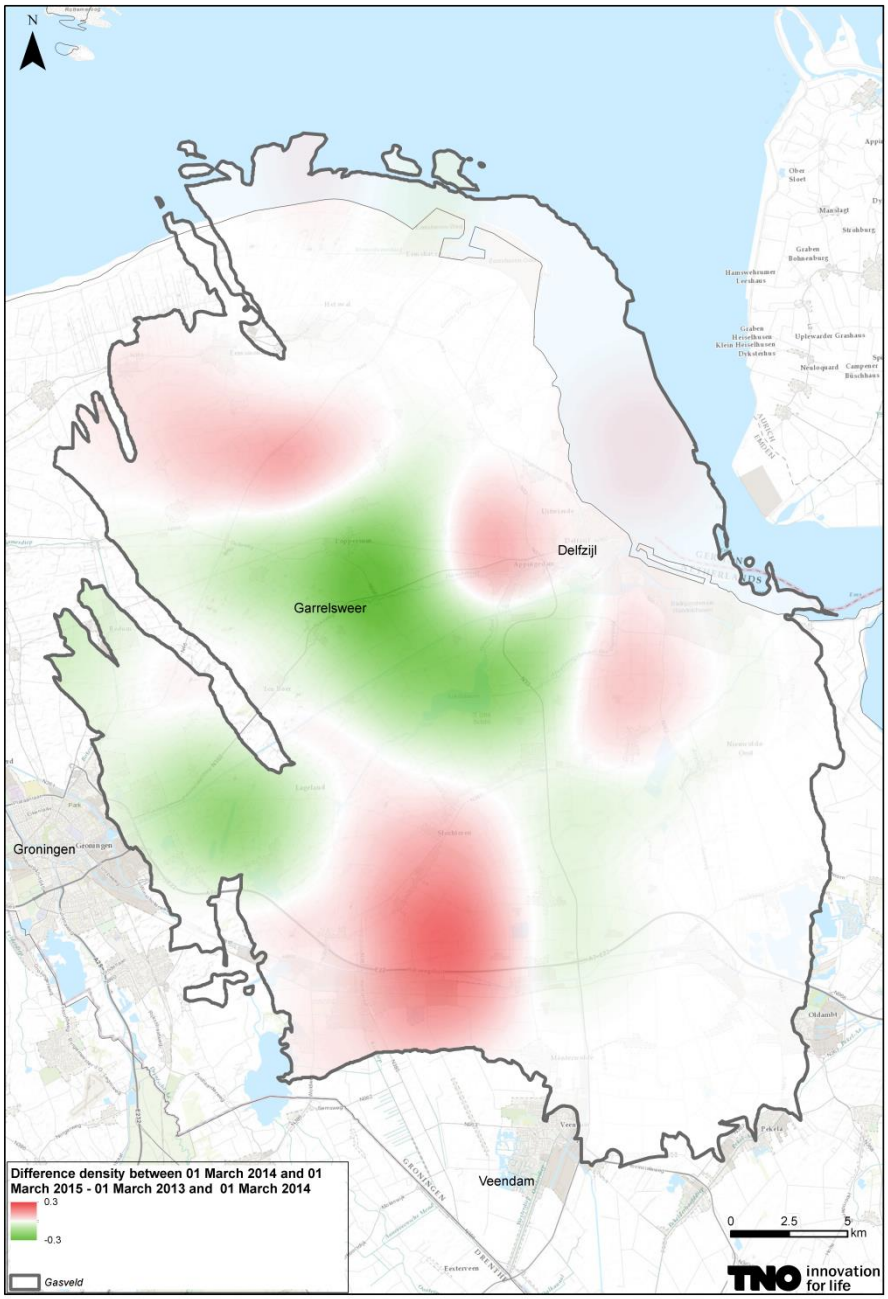

Figure A-9 Difference in event density between March 1st 2014-March 1st 2015 and March 1st 2013-March 1st 2014. A negative difference (green) indicates a lower event density in the later period compared to the earlier period. A positive difference is indicated in red.

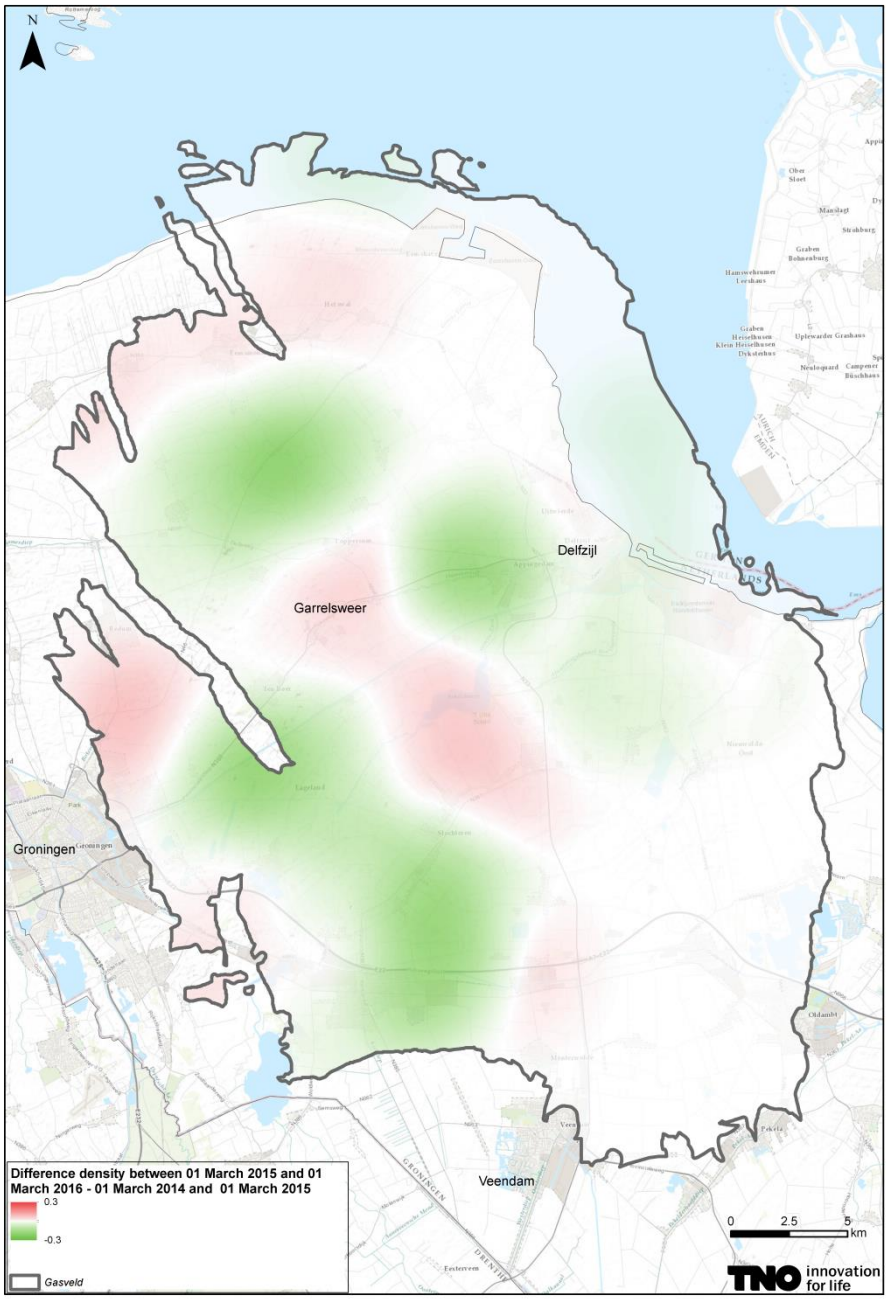

Figure A-10 Difference in event density between March 1st 2015-March 1st 2016 and March 1st 2014-March 1st 2015. A negative difference (green) indicates a lower event density in the later period compared to the earlier period. A positive difference is indicated in red.

A.3 Enlargement Figure 2-12

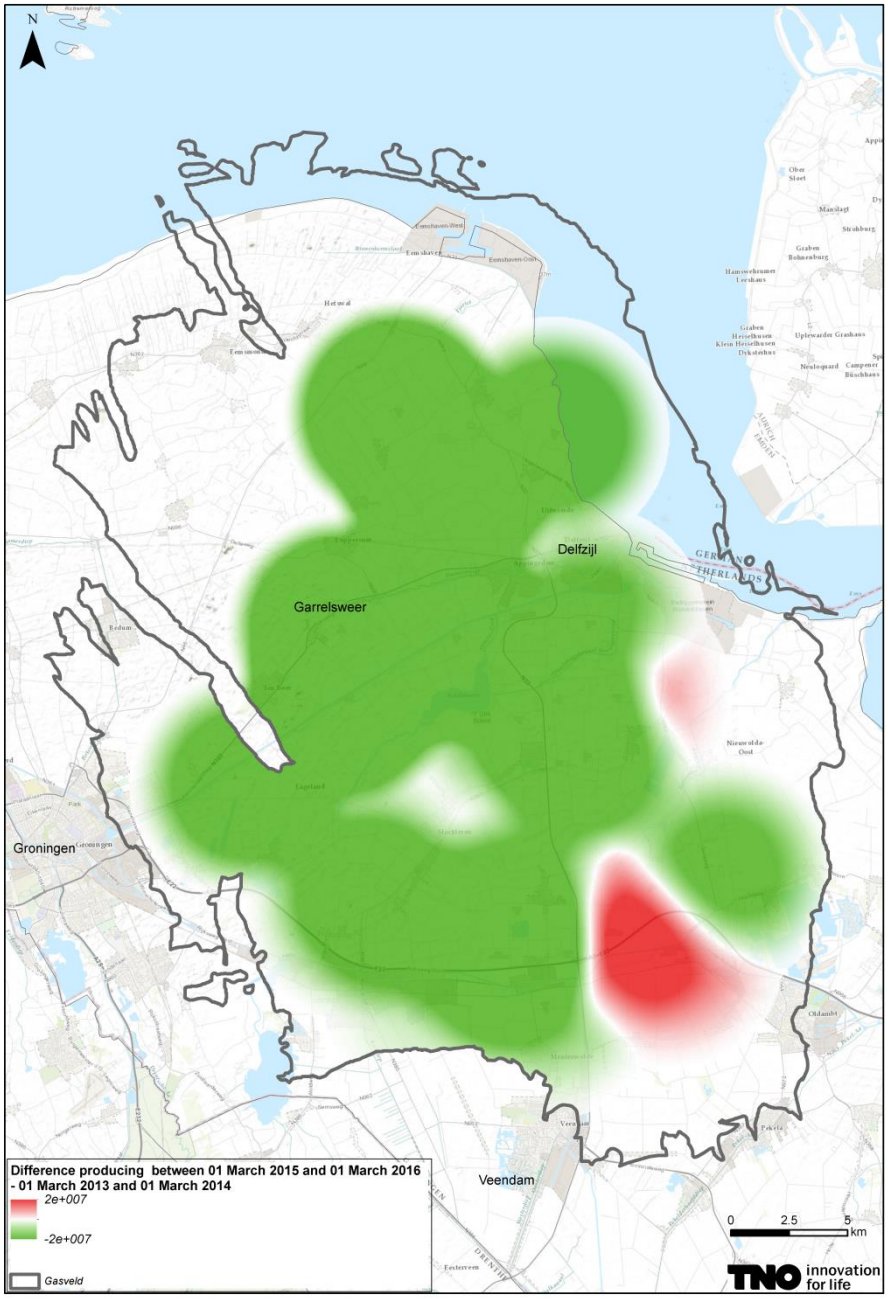

Figure A-11 Difference in production (in Nm^3 per km^2) between March 1st 2015-March 1st 2016 and March 1st 2013- March 1st 2014. A negative difference in production, shown in green, indicates a lower production between in the later period compared to the earlier period.

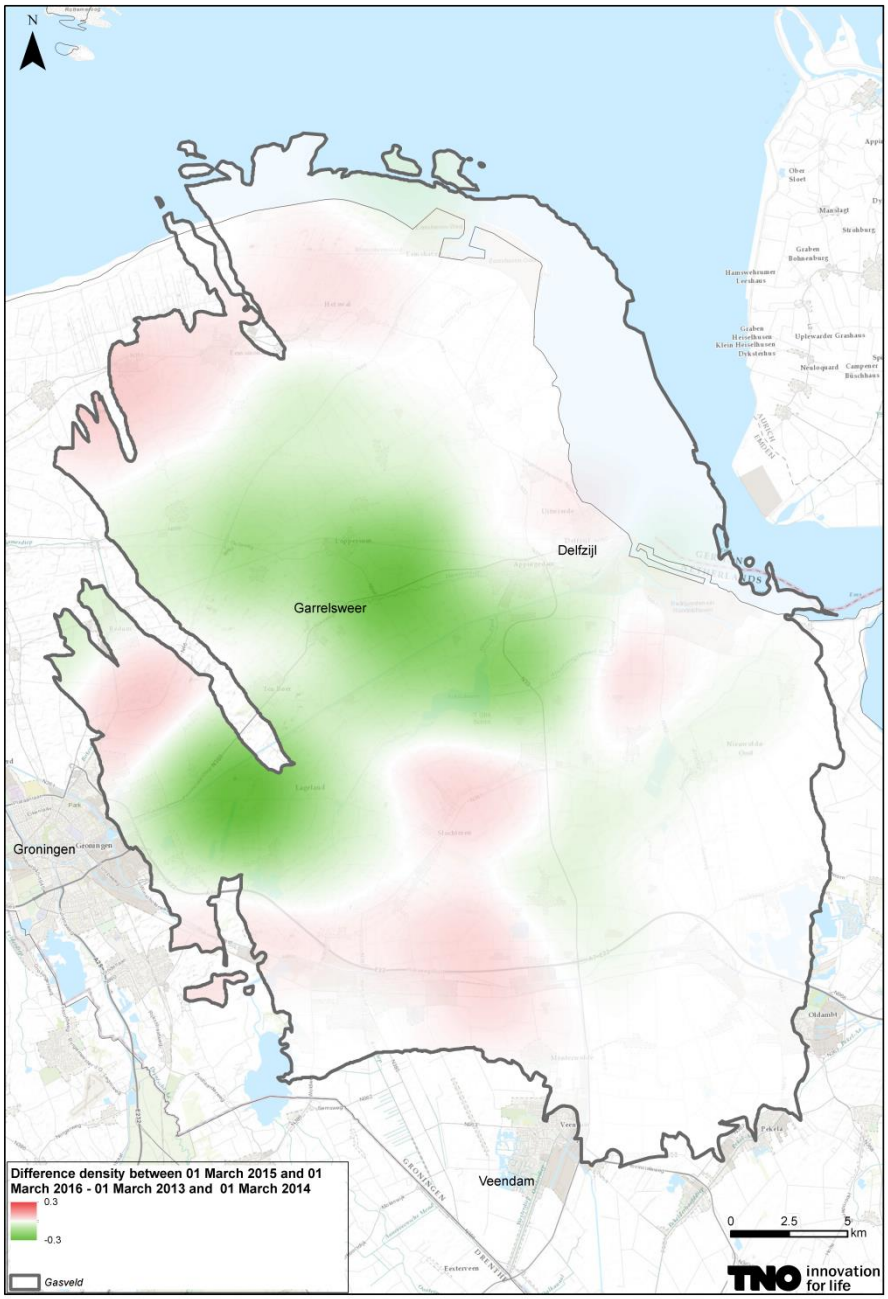

Figure A-12 Difference in event density between March 1st 2015-March 1st 2016 and March 1st 2013-March 1st 2014. A negative difference (green) indicates a lower event density in the later period compared to the earlier period. A positive difference is indicated in red.

B Catalogue completeness analysis for the Groningen borehole seismic network (from 1996 until extension in fall 2014)

Introduction

The KNMI borehole geophone network for the monitoring of induced seismicity in the Groningen gas field has been in operation since 1995. The network was initially designed to locate at least all earthquakes that could possibly be felt by the local population, i.e., earthquakes with local magnitudes of $M_L \geq 1.5$. The magnitude of completeness of the network has subsequently always been estimated at $M_{LC}=1.5$ (Dost, Goutbeek, van Eck, & Kraaijpoel, 2012)

The rate of regional earthquakes above this magnitude threshold is limited. In the direct vicinity of the Groningen Field, the recent average is of the annual number of events is around 20, peaking at 27 in 2013 **(**Figure B-1). Due to the low event rate for magnitudes above 1.5, statistical analyses aimed at detecting changes in catalogue properties such as event rates, spatial distributions and magnitude-frequency relations (e.g., b-values), require relatively long time frames to reach statistical significance. Under the assumption of scale independence, a reduction of the magnitude of completeness promises faster and/or more robust statistical inference. Therefore, part of the reason to enhance the regional network in recent years has been to decrease the current and future magnitude of completeness. With regard to the past it is important to determine a lower bound on the magnitude of completeness, such that as much data as possible can be utilized.

This study analyses the completeness of the Groningen borehole seismic network using an empirical, probabilistic approach. In a probabilistic sense there is no absolute certainty of completeness for any magnitude. Therefore, the magnitude of completeness is defined here in a probabilistic sense as the lowest magnitude that has a probability of more than 95% to yield three or more good quality P-wave picks, such that a location can be calculated.

Data

We use data from the KNMI regional borehole network, as it has been in operation since 1995, including the stations that have been added in the period 2009-2010, a total of 10 stations (see Table B-1,Figure B-1). De dataset consists of the KNMI catalogue of earthquake locations (Figure B-1) and magnitudes as well as the individual phase picks at the borehole stations that contribute to the location of each earthquake. Each pick associates a station to an earthquake. In this way, per pick a magnitude and an epicentral distance from the station to the event is defined. The collection of all the magnitude-distance-pairs associated to the picks we refer to as “hits”. We deliberately use the term “hit”, rather than the more specific “detection”. The reason is that the catalogue consists of only the events that have been located. An unknown number of unassociated single station detections have been left out. Additional to the P-wave picks, we also have information on the quality of the picks. We select only the P-wave picks that have an uncompromised quality and have, thus, not been down weighted in the location procedure.

Station	Installation	x (m)	y (m)
ENM	**1995-04-12**	**227789**	**602786**
ENV	**1995-09-09**	**238883**	**545977**
FSW	**1992-08-01**	**270718**	**582156**
HWF	**1995-06-02**	**219611**	**565337**
NIW	**2009-05-20**	**198667**	**596689**
SPY	**2010-07-08**	**247872**	**603512**
SUH	**2009-08-26**	**210036**	**580834**
VLW	**1995-05-23**	**269876**	**554827**
WDB	**1995-04-12**	**245080**	**581028**
ZLV	**1995-04-12**	**246514**	**568121**

Table B-1: Station installation date and coordinates. Coordinates in RD/Amersfoort reference system, EPSG:28992.

Complementary to the “hits”, we define the “misses”. These are magnitude-distance-pairs corresponding to earthquake-station pairs for the stations that did not contribute to the location of the earthquakes in the catalogue.
For each station we only consider earthquakes that occurred during the period of installation of the station. However, we do not check whether the station was actually recording at the time of the earthquake, as this information is not available in the catalogue.
In combination, the “hits” and “misses” collection provide a binary dataset (“hit”=1, “miss”=0) as function of two control parameters, being magnitude and epicentral distance. The dataset is visualized in Figure B-2 and Figure B-3.

Analysis

The analysis of consists of two stages. In the first stage we aim to establish an activation function that describes the probability of scoring a “hit” as a function of magnitude and epicentral distance. This refers to the probability of being able to pick a good quality P-wave travel time that is subsequently used to calculate an earthquake source location. The second stage is to combine the activation functions for all stations in the (greater) Groningen area and to deduce the probability of scoring three or more hits as a function of location and magnitude. This represents the probability of the event being localized by the network. The completeness can be visualized in a map.

Stage 1: Derive activation function

In practice, the ability to pick a good quality P-wave travel time depends on properties of both signal and noise. One possible approach to derive an activation function is to describe, in a probabilistic sense, the variabilities in both signal and noise, and model the probability of exceedance for a certain signal-to-noise ratio level. In this study, however, we choose an empirical approach using the existing local dataset described in the previous section. This has the advantage that there is no need to define a signal-to-noise threshold level.
We recognize that the dataset consists of the results of many binary Bernouilli trials (“unfair-coin tosses”), with probabilities conditioned on magnitude and distance. Therefore, using statistics we are able to constrain the underlying probability (or activation) function empirically. We realize that we have limited data in the range of

smaller magnitudes, precisely in our range of interest. In particular, we know that we have a shortage of “misses” in this range. This is simply because if a small magnitude event is missed by the nearby stations, it will most likely not be detected at all, and the “misses” will not be registered.
Therefore, we make an important next step by assuming that the dominant influence of both magnitude and distance on the activation probability enters through the signal amplitude. The translation from magnitude and distance into amplitude is done using the attenuation relation that was derived for induced seismicity and borehole stations in The Netherlands by (Dost, van Eck, & Haak, 2004):

$$\log_{10} A = M - 1.33 \log_{10} R - 0.00139\, R \; - \; 0.424,$$

where amplitude A is Wood-Anderson displacement in mm, M is (local) magnitude and R is hypocentral distance in km (where we assume source depth at 3km). The attenuation relation provides the median of a distribution that is usually assumed to be lognormal. See Figure B-4 for a histogram of the spread of observed amplitudes in the catalogue around the median as predicted by the attenuation relation. The maximum likelihood lognormal distribution for this dataset is shown as well.
Figure B-5 shows the “hits” and “misses” for a single station (WDB) and all stations combined against the background of equal-amplitude contours according to the attenuation relation.
We choose to derive a single activation function that represents all stations in the network. The reason is simply that there are not sufficient data points to apply this method to all individual stations. The consequence is that the activation function is now predominantly based on the stations with most data points, being WDB, ZLV, FSW and ENM.
After converting all magnitude-distance pairs to amplitudes according to the attenuation relation, the full dataset can be represented by histograms as shown in Figure B-6. The histograms reveal the increasing probability of scoring a hit with increasing amplitude. To interpret the histograms we can make the following simplifying assumptions: (a) a successful detection requires a minimal (threshold) signal-to-noise ratio, (b) signal amplitude variations are distributed log-normally, and (c) noise levels are practically either constant, or also distributed log-normally. Under this circumstance we expect the activation function to be a cumulative log-normal distribution function. The envelope of the fractional hits histogram in the bottom panel of Figure B-6 seems to confirm this. The next step is to determine the activation function. We use regression using a probit model.
In the dataset we do not have information on the operational status of the individual borehole stations. Therefore, in case of a miss it is not clear whether this is due to insufficient signal-to-noise ratio, or due to a station failure, or some other reason, such as interpretation issues. In case of a station failure the miss probability is independent of the amplitude level. The effect of the false misses is most prominent at the higher amplitudes, where the true miss probability is expected to be low. From the histograms (Figure B-6) we can see the largest deviations from the expected shapes there. Therefore, we do a probit regression not only on the full dataset, but also on the dataset with a maximum displacement truncation. We have set the truncation level at exp(A)=-2, or A~0.135 mm. Figure B-7 shows the histograms for the dataset after truncation.

The resulting activation functions of both probit analyses are displayed in Figure B-8. Also shown is the step function that (Dost, Goutbeek, van Eck, & Kraaijpoel, 2012) define as the detection threshold to assess the network completeness. This last approach is not probabilistic: it underestimates the hit probability for smaller amplitudes, and it overestimates the probability for larger amplitudes.
The translation of the derived activation functions from amplitudes back to magnitude/distance pairs is show in Figure B-9.

Stage 2: Completeness map construction
Once the hit probability has been defined as a function of magnitude and distance, the catalogue completeness of the network can be analysed. For a given location in the region, the distances to all stations in the network are fixed. Then, for a given magnitude the hit probability for each station is fixed. Each hit or miss is then basically the outcome of a Bernoulli trial. The probability of scoring n hits in N independent Bernoulli trials is described by the Poisson binomial distribution.
Figure B- 10 displays the probability of scoring 3 or more hits in any combination of the 10 available stations. Curves are shown for two arbitrary locations. Also shown is the 0.95 probability level that implicitly defines the magnitude of completeness for each location.
Figure B-11 shows the result of evaluating the magnitude of completeness for the entire Groningen region by means of contours. Contours are shown for both probit models of Figure B-8. It turns out that the full range probit model leads to a slightly more conservative estimate. A comparison between the limited range probit model and the threshold model is displayed in Figure B-12. The threshold completeness map has much more detail, but since the model is not probabilistic it should not be over-interpreted. In general, the threshold model is a bit less conservative than the probabilistic model. Almost the entire Groningen Fields falls within the 1.2 contour.

Discussion

We have analysed the completeness of the Groningen seismic catalogue using a probabilistic method based on empirical detection probabilities. For the period after 2010 the completeness of the Groningen catalogue is estimated at 1.3 for the entire field and 1.2 for the most active areas.
In a probabilistic sense the magnitude of completeness is not an unambiguous concept. In fact, according to the model there is no absolute certainty of detection for any magnitude. In this report a probability of 95% was chosen as the threshold value for defining completeness. It must be said that there is some arbitrariness in this choice.
Our plan for future is to step away from the concept of a magnitude of completeness. Instead we propose utilize the full catalogue completeness information as a function of space, time and magnitude in the statistical assessment of catalogue parameters.

Bibliography

Dost, B., Goutbeek, F., van Eck, T., & Kraaijpoel, D. (2012). *Monitoring induced seismicity in the North of the Netherlands: status report 2010.* De Bilt: KNMI.

Dost, B., van Eck, T., & Haak, H. (2004). Scaling of peak ground acceleration and peak ground velocity recorded in the Netherlands. *Bolletino di Geofisica ed Applicata*, 153-168.

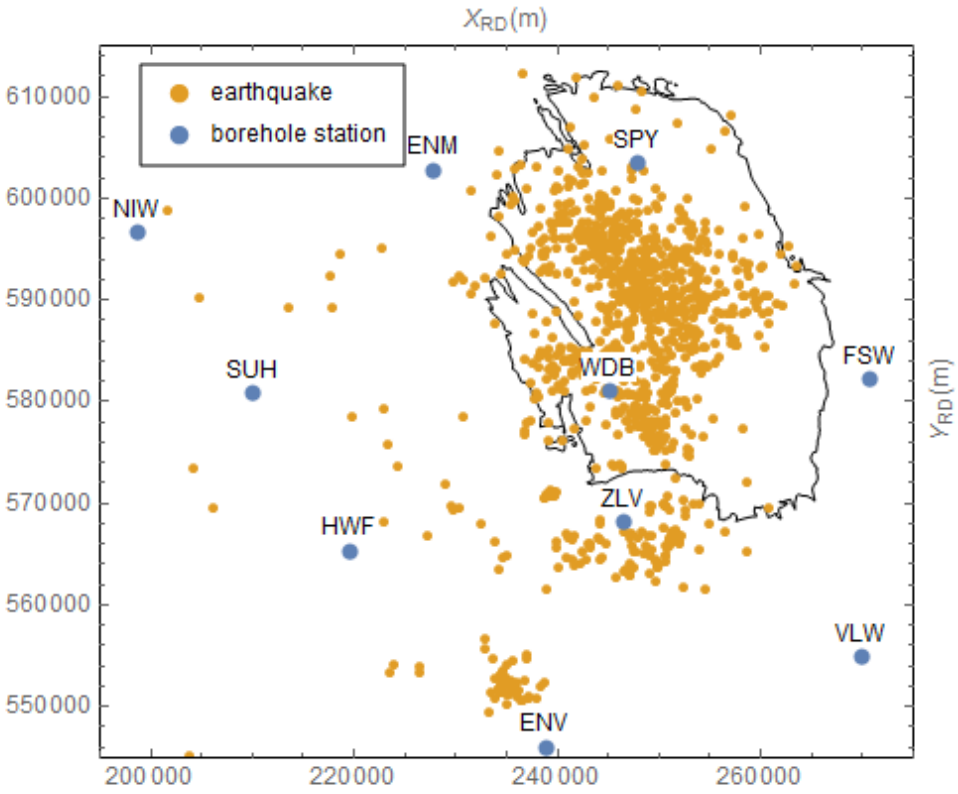

Figure B-1 Earthquake locations and borehole stations in the study region.

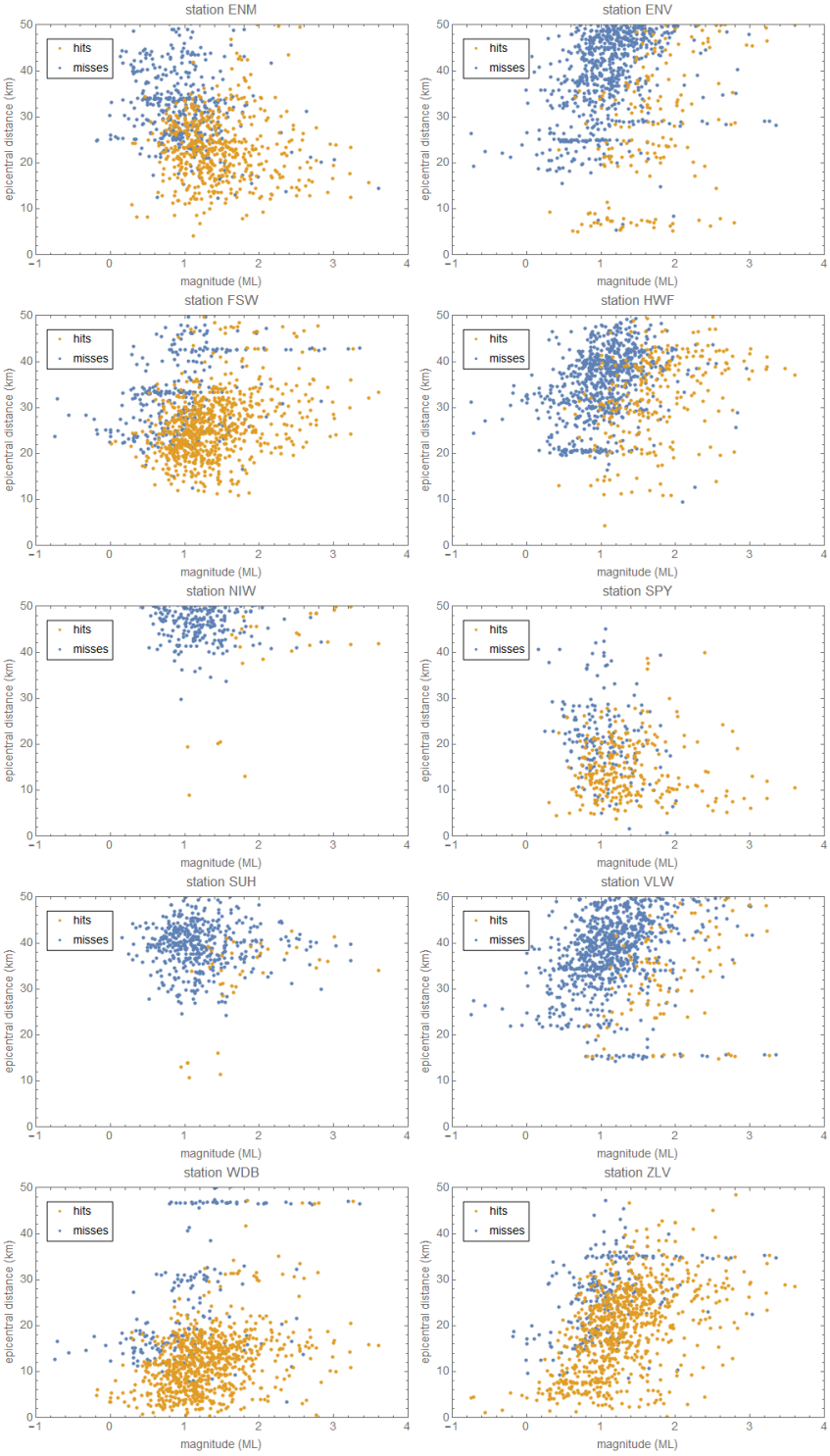

Figure B-2 Collection of hits and misses for all 10 stations in the Groningen borehole network Figure B-1.

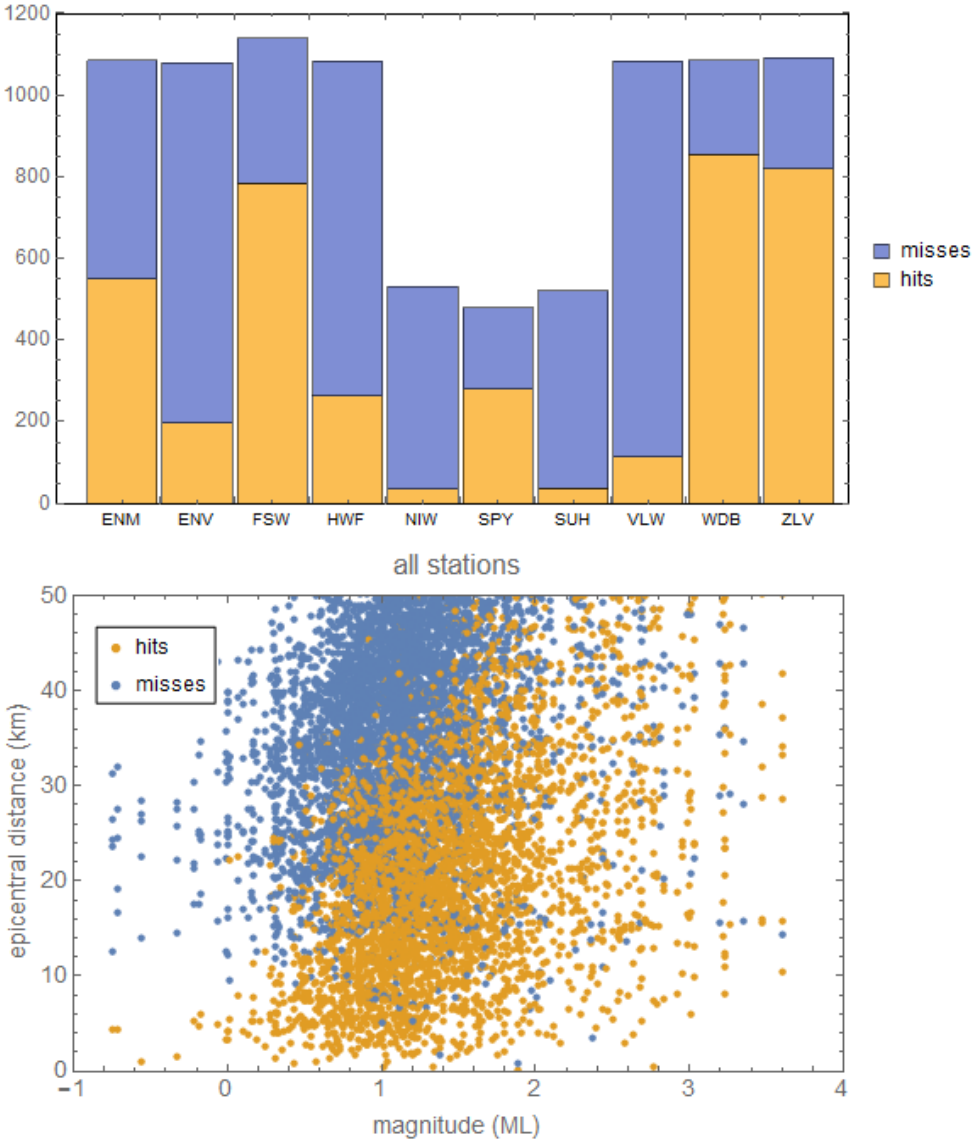

Figure B-3 Aggregate of Figure B-2

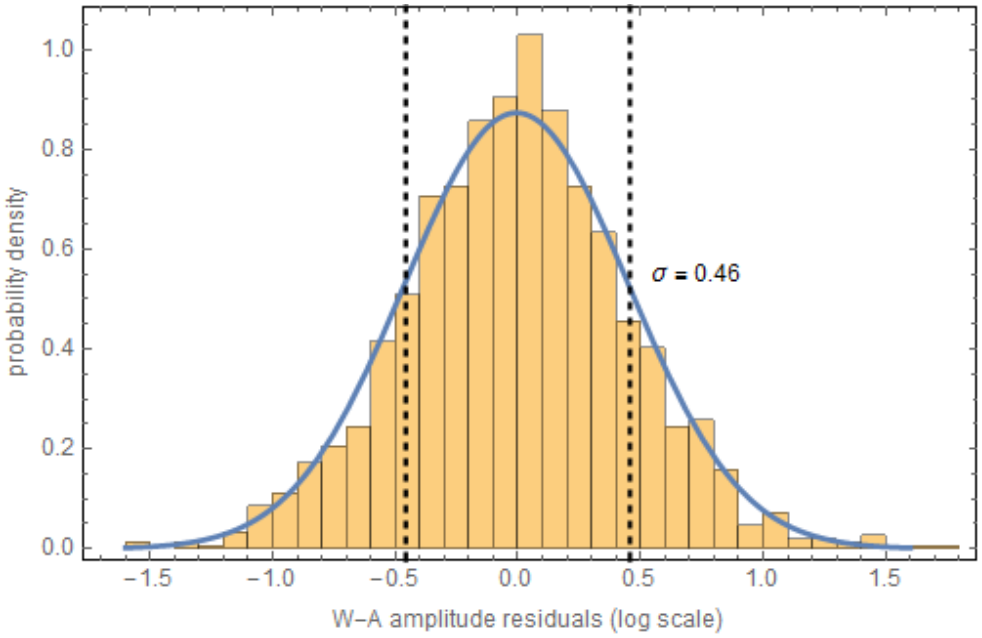

Figure B-4: Spread (residuals) of observed Wood-Anderson displacements in natural logarithmic scale with respect to the attenuation relation. The histogram and estimated (maximum likelihood) normal distribution confirm the expected log-normal distribution of amplitudes conditioned on magnitude-distance pairs. The histogram distribution is slightly more peaked than normal at 0.0 due to bias: with few observations the estimated magnitude for an earthquake is biased towards the individual station estimates.

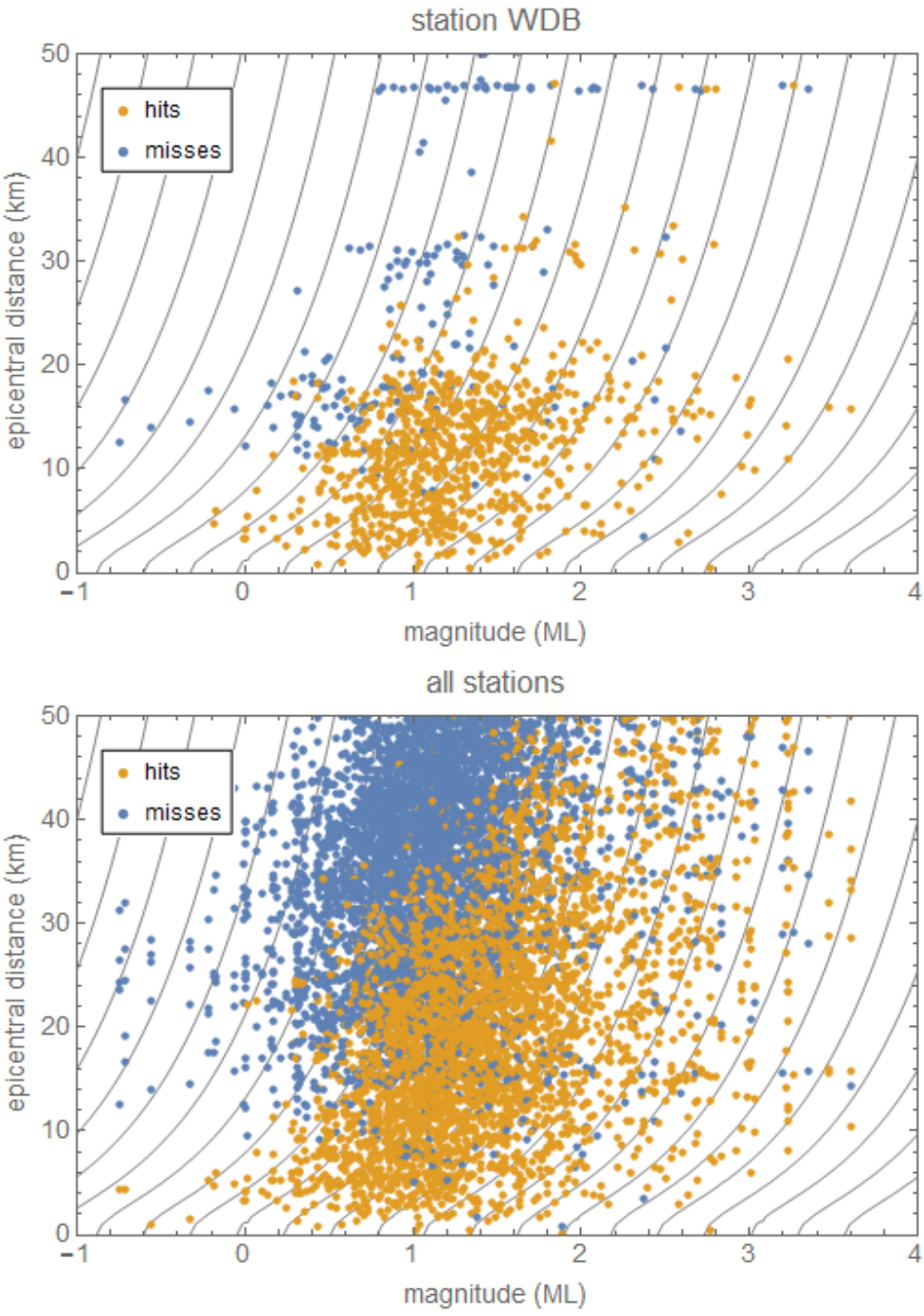

Figure B-5 Hits and misses for station WDB (top) and all stations combined (bottom), against a background of constant amplitude contours, according to the attenuation relation.

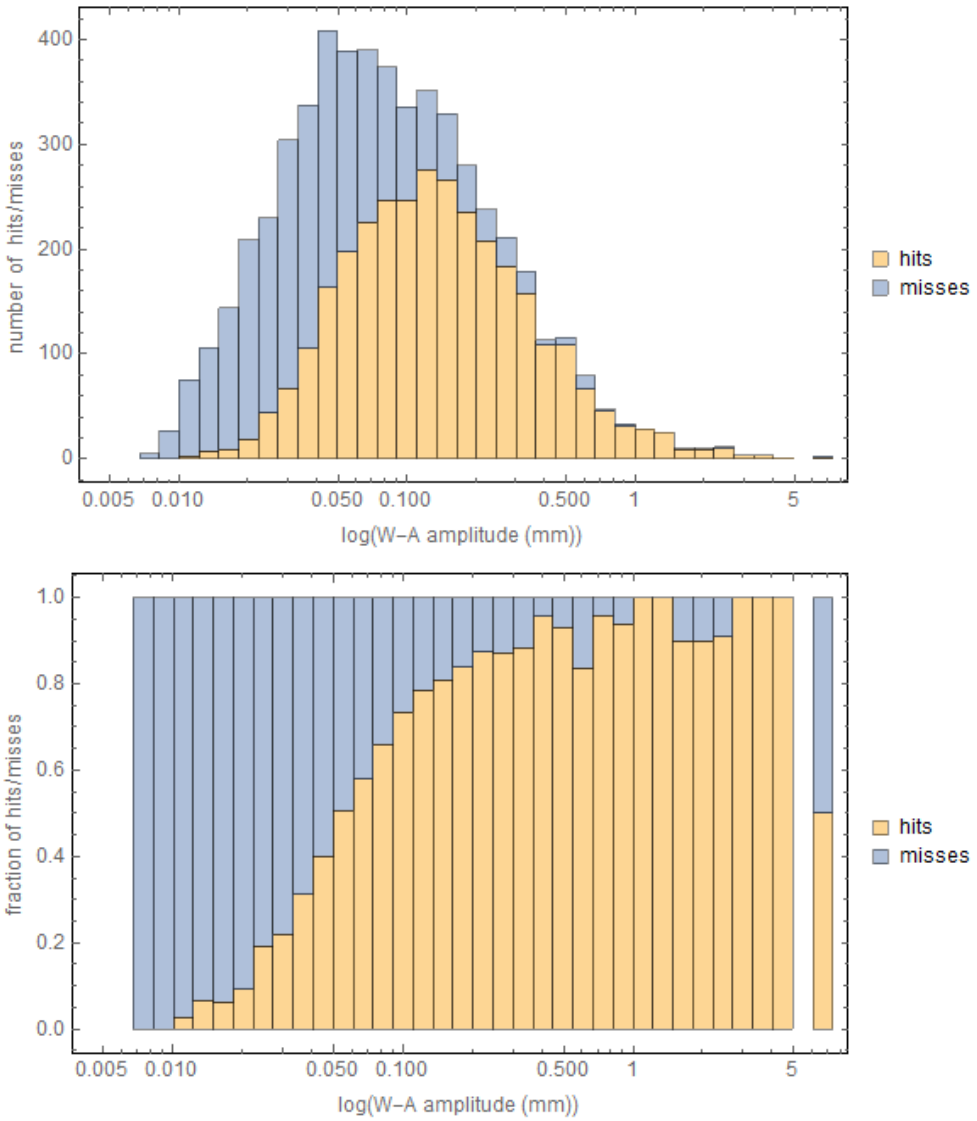

Figure B-6 Histograms of hits and misses as a function of signal amplitude as predicted by the attenuation relation (Wood-Anderson displacement in mm). Upper panel shows absolute numbers, lower panel shows fractions. Panels show all hits and misses for earthquakes with magnitudes between 0.5 and 2.0, distance maximized at 40 km

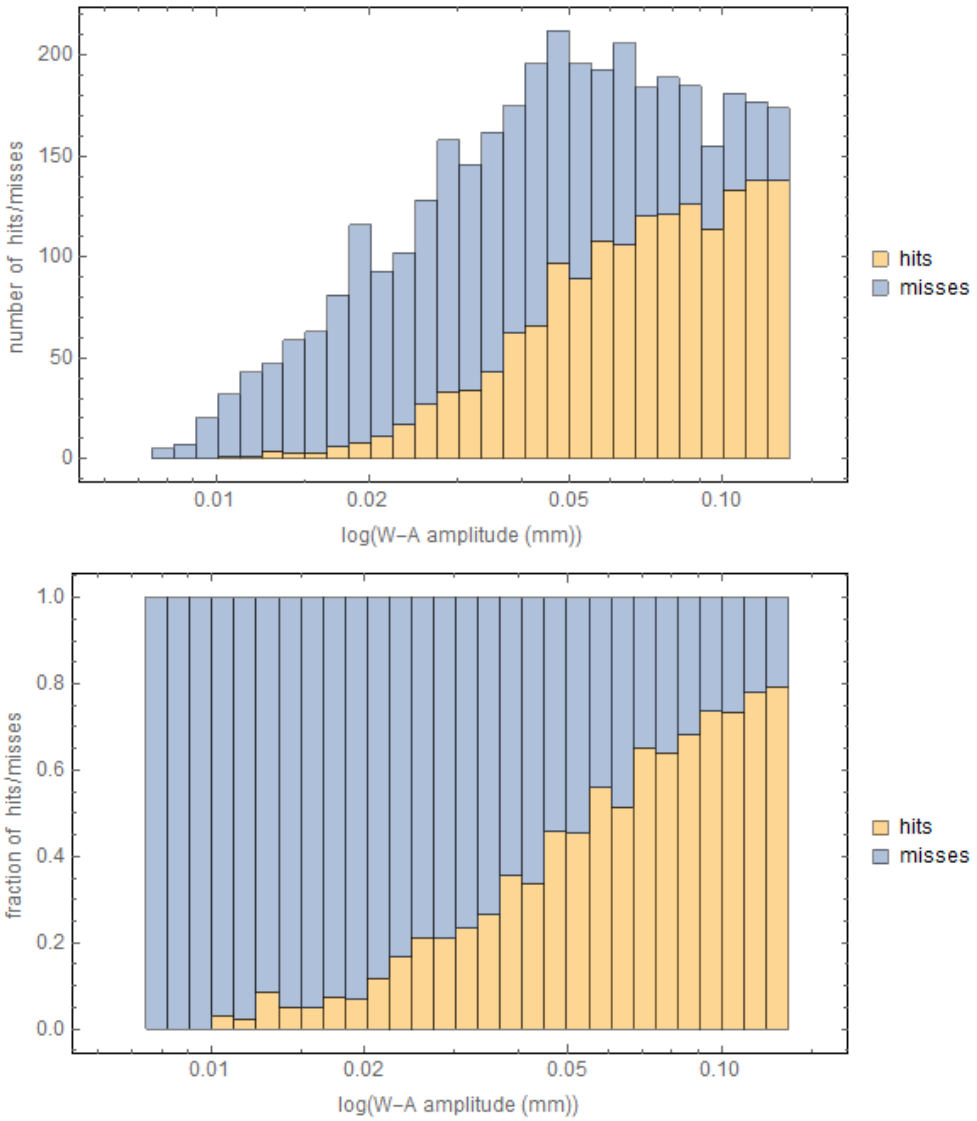

Figure B-7 Histograms of hits and misses as a function of signal amplitude as predicted by the attenuation relation (Wood-Anderson displacement in mm). Upper panel shows absolute numbers, lower panel shows fractions. Panels shows same data as Figure B-6, except now with an amplitude cut-off at 0.135 mm.

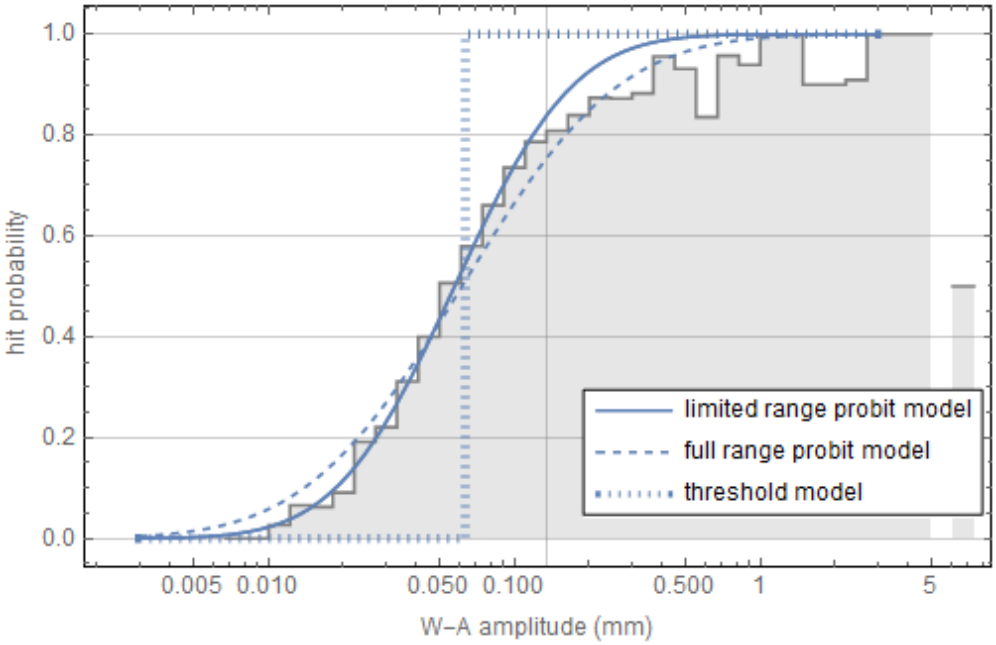

Figure B-8 Three models for hit probability as a function of (median) signal amplitude as predicted by the attenuation relation (Wood-Anderson displacement in mm). Two models are derived empirically from the catalogue data using probit regression. The first (dashed line) is based on the full range of hit/miss data as displayed in Figure B-6 the second one (full line) is based on the limited range displayed in Figure B-7. The extent of the limited range is shown using the vertical grid line (at 0.135 mm). The limited range model is preferred due to its better fit with the (low amplitude) data, as represented by the grey histogram envelope curve, borrowed from Figure B-6. The third model shown is the model used by KNMI in Dost et al. (2012). This model defines a hard detection threshold (at 0.063 mm) and is not probabilistic. It underestimates and overestimates hit probabilities for lower and higher amplitudes respectively.

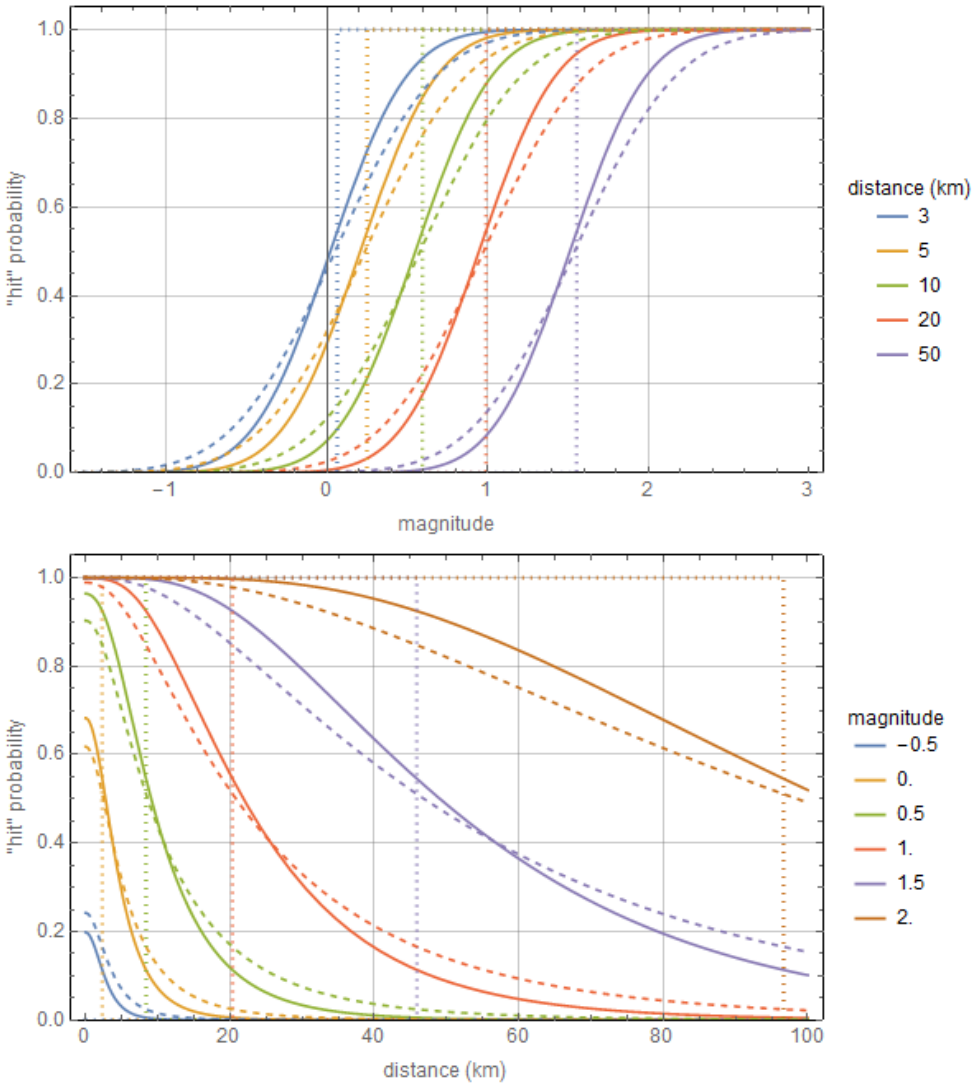

Figure B-9 Representation of the hit probability models of Figure B-8 in terms of magnitudes and distances. Line styles correspond to Figure B-8: solids, dashed and dotted correspond to limited range probit, full range probit and KNMI threshold models respectively.

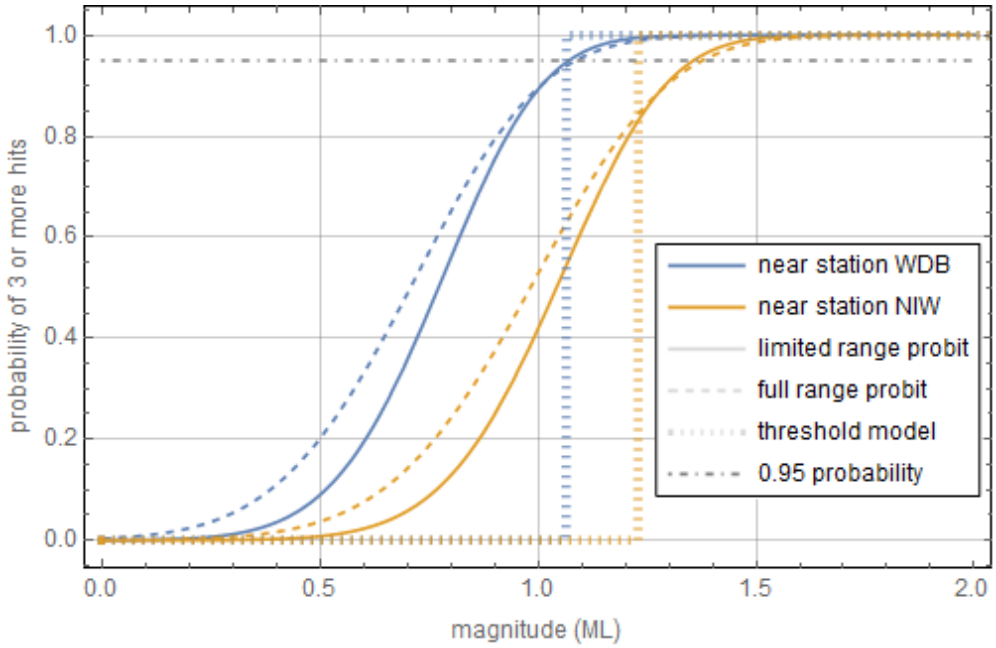

Figure B- 10 Probability of three or more hits - and a successful earthquake location - for earthquakes at two arbitrary locations near stations WDB and NIW respectively, according to the three hit probability models of Figure B-8. Line styles correspond to Figure B-8: solids, dashed and dotted correspond to limited range probit, full range probit and KNMI threshold models respectively. The 95% probability level is indicated. The magnitude of completeness as defined in this report can be determined by reading off the magnitude at the cross point of the activation function with this level.

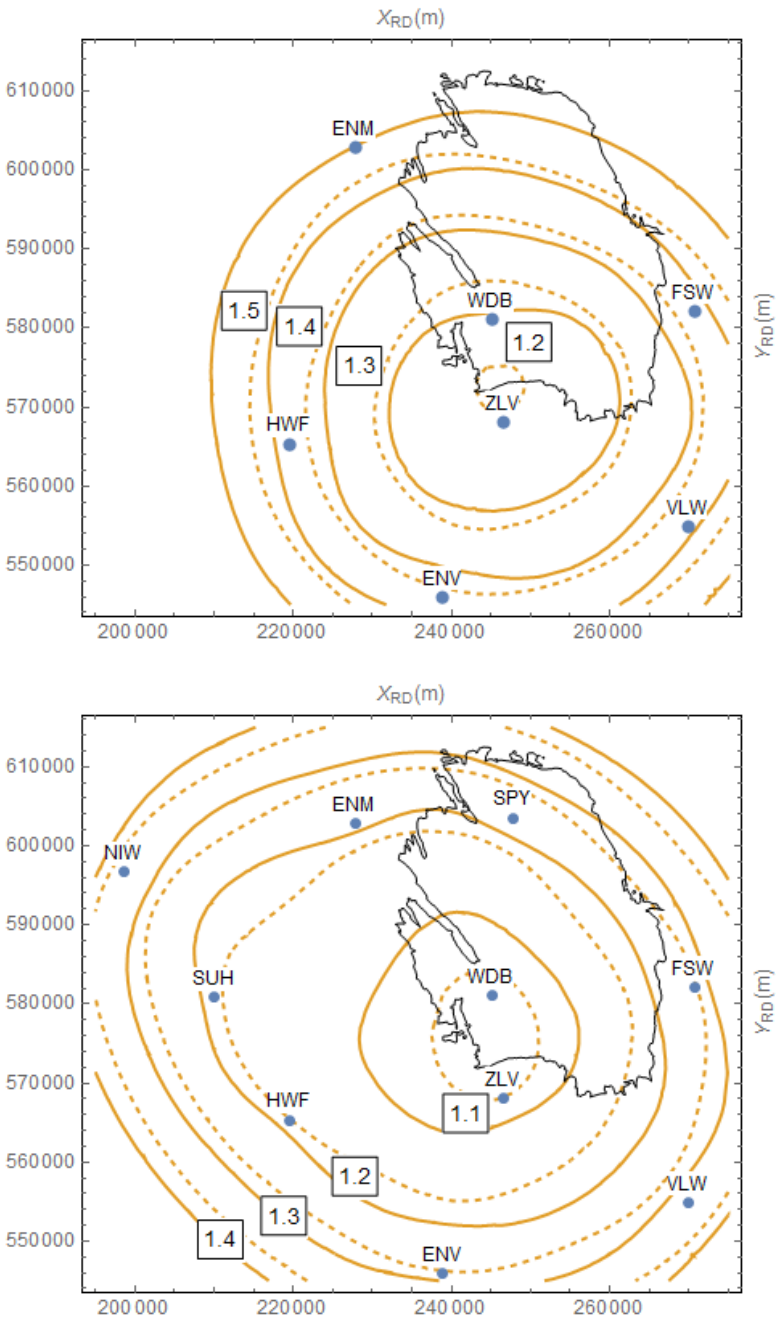

Figure B-11 Magnitude of completeness map for the two probit hit probability models. Solid and dashed lines represent the limited range and full range probit models respectively. Top panel corresponds to the situation before the network extension from 2009/2010. Bottom panel corresponds to the situation in the period 2010-2014. In both cases the full range probit model is a bit more conservative.

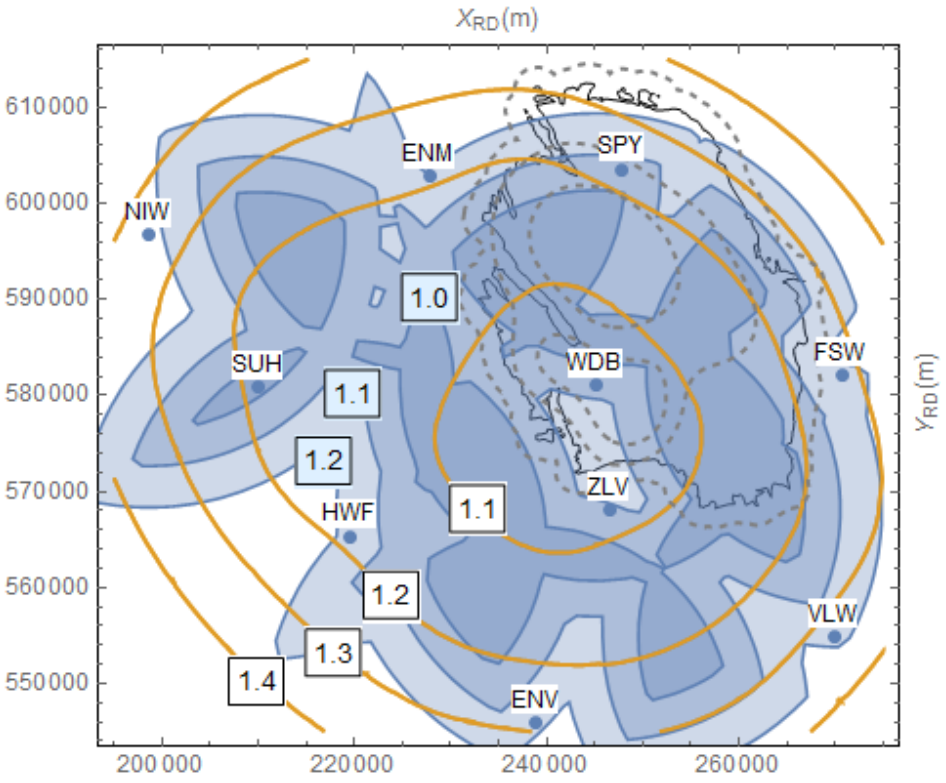

Figure B-12 Comparison of the limited range probit model completeness map with the threshold completeness map, displayed using blue shaded contours. The latter has much more structure and is a bit less conservative. The seismically active area falls almost completely within the 1.1 contour, although the patch between WDB and ZLV has a bit lower completeness.

C Appendix Bayesian change point

Table C-1 Data presented in Figure 3-4. Event change with time for the entire Groningen field and all magnitudes above 1.0

Nr.	Middle of the time period	Event rate
1	17-6-1999	9
2	17-5-2000	11
3	2-7-2000	12
4	17-5-2002	16
5	17-6-2003	23
6	16-12-2006	28
7	2-7-2009	44
8	19-3-2012	51
9	17-8-2013	73
10	11-1-2015	47
11	16-12-1996	9
12	17-6-2007	32
13	17-5-2008	32
14	1-1-1998	11
15	2-7-2009	40
16	1-8-2010	42
17	16-6-2012	49
18	17-8-2013	73
19	10-4-2015	44

Table C-2 Data presented in Figure 3-7. Event change with time for the entire Groningen field and all magnitudes above 1.3.

Nr.	Middle of the time period	Event rate
1	31-12-1996	5.8
2	2-7-2004	8,5
3	2-7-1999	7
4	1-1-2007	18
5	1-1-2006	14.3
6	2-7-2012	33
7	2-7-1998	7.3
8	31-1-2011	25.5
9	31-12-2000	8.4
10	31-1-2011	26
11	1-8-2013	30
12	1-1-2006	14

D Time dependent compaction and induced seismicity: inferences from geomechanical modelling of gas depletion

This appendix has been submitted as a research paper on 17 December 2015 to Journal of Geophycial Research: Solid Earth. The paper will be reviewed by external experts and, after revision, and resubmission published in the Journal.

Abstract

Induced seismic events occur in natural gas production and can be a major concern. A predictive model relating compaction strain to seismic moment has recently been proposed for depleting gas reservoirs (Bourne et al., 2014). For time dependent compaction following a production stop, this heuristic model implies that seismicity rates are significant and reduce slowly. Here we use geomechanical models to show that a break arises in the compaction strain-stress relationship, upon arrest of pressure change. Consequently, the seismic moment increase slows down after production stop. The geomechanical models predict up to one order of magnitude lower seismic rates after stop of production, compared to the heuristic approach, and is in agreement with low seismicity in the central area of the Groningen field immediately after reduction in production. The geomechanical model findings support scope for mitigating induced seismicity through adjusting rates of pressure change and production.

Key words: induced seismicity, gas depletion, compaction, geomechanics

Introduction

Time dependent compaction of hydrocarbon reservoirs is a well-known phenomenon. Laboratory experiments indicate that time-dependent compaction can amount to 100% or more of direct (elastic) compaction for clastic and shale reservoirs [*Hettema et al.,* 2000; *De Waal,* 1986; *Sone and Zoback,* 2014; *Pruiksma et al.,* 2015]. Results from subsidence inversion demonstrate that reservoir compaction rates are delayed relative to pressure drop, in line with laboratory data [*Fokker and Van Thienen-Visser,* 2015; *Mossop,* 2012; *Hettema et al.,* 2000]. Compaction of clastic reservoir rocks is predicted to continue for decades after a potential shut-in of production or end of field life, and creep may constitute a significant portion (up to 10%) of the compaction prior to cessation of production [*Pruiksma et al.,* 2015; *Mossop,* 2012]. In addition time-dependent strain of over and underburden rock as a function of creep and pressure diffusion can contribute to time dependent compaction and subsidence [*Orlic and Wassing,* 2013; *Chang et al.,* 2014; *Marketos et al.,* 2015].

Bourne et al [2014] introduced a heuristic predictive model for seismicity due to fluid extraction from hydrocarbon reservoirs, using compaction strains as a proxy for potential stress change and seismic moment, in analogy to the strain-stress–seismic moment proxy introduced by [*Kostrov,* 1974; *McGarr,* 2014]. This predictive model is based on an approximately linear relationship between the volume integral of reservoir compaction strains and the logarithm of expected cumulative seismic moments, and has been constrained with seismic data from the Groningen field in the Netherlands during production over many decades (Fig. 1). An outcome of their model is that the seismic hazard hardly decreases when halting or significantly lowering production rates. This is related to their forecasted increase of seismic moment after shutin of the production, which, depending on the decay rate of their time-dependent compaction model, could result in no noticeable reduction of seismicity rates in the first year after shutin. The outcome was unexpected to us, and did not agree with the most recent observations in the Groningen field. Therefore, we employed a simplified geomechanical model that disentangles the effects of pressure change and time dependent compaction, in order to test the results from the heuristic model and the field data from physics principles. It builds on geomechanical model approaches developed in the past decades for induced seismicity related to hydrocarbon extraction [*Segall,* 1989; *Van Eijs et al.,* 2006; *Suckale,* 2009; *Van Wees et al.,* 2014; *Bourne et al.,* 2014; *Segall et al.,* 1994; *Roest and Kuilman,* 1994].

We aim to evaluate the geomechanical model approach in view of Groningen field data, in which a significant cut in production rates in the central area was applied in 2014 [*van Thienen-Visser and Breunese,* 2015]. To this end we introduce in Section 2 the relevant data of the Groningen gas field and their significance in unravelling the control of pressure change and time dependent compaction on seismicity. Subsequently, in Section 3, we introduce the geomechanical modelling approach, which is based on a visco-elastic finite element solution for a typical two-dimensional reservoir section. The model predicts the stress response of the reservoir, including time-dependent reservoir compaction, and highlights the reduction of stress build-up upon termination of production. In Section 4, we analyze the results in terms of expected slip and seismic moment increase using a simple analytical approach to predict fault slip from the visco-elastic solution. We will show that the model predicts a significant reduction of seismic moment increase after production stop, in agreement with observations, and we argue that the findings of our study are expected to hold for depleting reservoirs in general, in similar reservoir conditions.

Groningen field data

The study of Bourne et al. considered gas depletion in the Groningen field until 2013. This is just prior to a 80% reduction at January 17 2014 of the production in the clusters in the central area of the Groningen field. This area, constituting over 25% of total field production prior to reduction (Fig. 1, Fig. 2), had shown the majority of induced events [*van Thienen-Visser and Breunese,* 2015]. The seismic data (Fig. 2) show a statistically significant reduction of seismic events [*van Thienen-Visser*

et al., 2015] and strongly suggest that the rate of seismic moment increase is considerably reduced after the production cut.
The reduction in massive production in the central area of the Groningen field, of which the effects are closely monitored via the recorded seismicity, provides a unique dataset documenting the break in trend of seismicity which can be attributed to relative change in rates of time dependent compaction and pressure change in the reservoir. Past studies and associated datasets on gas depletion in other fields do not provide such data for the following reasons:

1) A mid field-life production cut at the scale as applied in the central area of the Groningen field because of high seismicity levels, is exceptional.
2) Induced seismicity is generally not monitored by a dedicated local network prior to the occurrence of induced events leading to stop of production, such as in the case of the Rotenburg Field in Germany [*Dahm et al.,* 2007]. Therefore, seismic catalogues generally contain not enough events for a thorough statistical or meaningful mechanical analysis.
3) Well monitored producing fields are typically marked by a gradual decay in production and the associated pressure change prior to production stop. As a consequence, fields may show a gradual reduction of seismic rates in the tail of production, such as observed in Lacq in France [*Bardainne et al.,* 2008] and the Strachan field in Canada [*Baranova et al.,* 1999]. In fields where production has stopped seismicity rates appear to return to background rates, such as observed for the Strachan Field, and the Roswinkel and Bergermeer fields in the Netherlands, marked by 25 and 4 seismic events (M>1.5) during production and no events for 9 and 8 years after production stop respectively, in accordance with absence of natural seismicity [*Van Wees et al.,* 2014]. Because of the decay in pressure rate changes, there is abundant time to relax major part of time dependent compaction prior to production stop, which renders these cases not suitable for the analysis we pursue.
4) The abundance of natural seismicity and strong aquifer support resulting in equilibration of reservoir pressure on short timescales can render it difficult to analyze post production evolution.

In summary, the Groningen field is marked by a sharp and prolonged drop in production rates in the central area, of which the effects are well documented in the seismic catalogue (Fig. 2). The field is located in a tectonic quiet area, and characterized by limited aquifer pressure support, qualifying as excellent case study to disentangle the pressure-dependent and time-dependent compaction control on induced seismicity.

Geomechanical model

Geomechanical models demonstrate that a progressive increase in induced events relates to progressive stress perturbations due to depletion, and that the relative magnitude of stress perturbations is strongly dependent on initial stresses, pressure change, reservoir geometry [*Segall,* 1989; *Mulders,* 2003; *Roest and Kuilman,* 1994], time dependent compaction and creep [*Orlic and Wassing,* 2013].

In a geomechanical model, the expected evolution of cumulative seismic moment evolution (*M0*) can be determined from predicted slip on faults via:

$M0 = \int G\ u\ dA$ (eq. 1)

where *A* is surface area of faults, *u* is displacement, *G* is the shear modulus [ref]. The onset and subsequent amount of slip is a function of the change in Coulomb failure function (*ΔCFF*) in relation to the in-situ stress:

$\Delta CFF = \Delta\sigma_s - \mu\Delta\sigma_n'$ (eq. 2)

where σ_s is shear stress , σ_n' effective normal stress on the fault, and μ the friction coefficient. A numerical approach can include slip weakening effects and/or rate and state friction effects during rupture events [*Rutqvist et al.,* 2013; *Wassing et al.,* 2014; *Ruina,* 1983; *Dieterich,* 1994]. Part of the slip may occur aseismically. In our simplified approach, we discard effects of dynamic effects of slip and slip weakening and assume that all incremental slip is released seismically. In elastic models, *ΔCFF* scales linearly to pressure change ΔP through changes in the total stress tensor on the fault [*Soltanzadeh and Hawkes,* 2008; *Mulders,* 2003]:

$\Delta\sigma_{ij} = \gamma_{ij}\,\Delta P$ (eq. 3)

where σ_{ij} are the total stress tensor components, and γ_{ij} stress arching parameters, which vary over the fault surface. These models are well capable of predicting an accelerating increase of seismic moment as a function of pressure change [*Van Wees et al.,* 2014]. *Mulders* [2003] and *Van Eijs et al.* [2006] demonstrate that arching effects and *ΔCFF* get amplified with increasing contrast in elastic properties of reservoir and surrounding rock. In the Groningen field the pressure change is rather uniform [*Van Wees et al.,* 2014; *Bourne et al.,* 2014].

3.1 Adopting time dependent compaction

Insufficient consensus of the exact creep mechanism in the Groningen field is currently available to justify a particular choice for the time dependent compaction constitutive law [*Mossop,* 2012; *Pruiksma et al.,* 2015; *Hol et al.,* 2015]. We adopt the Kelvin-Chain model (Fig. 3), which should be considered a simplified constitutive law. It cannot take into account irreversible deformation, and stress paths in alternative constitutive models will be quantitatively deviating from our prediction. However, the relative change in stress response upon cessation of depletion is not likely to change significantly, as this is primarily driven by the break in loading mechanism after an arrest of pressure changes.

In the Kelvin-Chain the spring marked by stiffness *E* allows for an elastic stress response, which should be in accordance to the static Young's modulus. Lab measurements document *E* typically in the range of 8-25 GPa [*Pruiksma et al.,* 2015; *Hol et al.,* 2015].

The Kelvin chain component with spring constant E_1 and dashpot with Newtonian viscosity η_1 (Fig. 3) represents the time dependent compaction. For uniaxial strain, this component corresponds to the decay model proposed by *Mossop* [2012], in which compaction of the reservoir c(x,y,t) is constructed by the convolution:

$c(x,y,t) = f(x,y,t) * g(t)$ (eq. 4)

with

$$f(x,y,t) = H(x,y)\ C_{tinf}\ \Delta P(t)$$

$$g(t) = \frac{1}{\tau} e^{-t/\tau}$$

where *H(x,y)* is the thickness of the reservoir at location (x,y), C_{tinf} corresponds to time dependent compaction strain at pressure change ΔP at infinite time, and τ is the relaxation time of time dependent compaction. Physically, the decay function *g(t)* is interpreted to represent an effect of pressure diffusion of the reservoir [*Mossop,* 2012].
The Kelvin-Chain model has the convenient property that the stress strain matrix for a loading increment can be constructed by a pseudo stiffness (Young's modulus) E_p:
$E_p = \frac{\varepsilon_e}{\varepsilon_e+\varepsilon_c} E$ (eq. 5)
which scales to E according the ratio of elastic strain ε_e and total strain, which is the sum of elastic strain ε_e and time-dependent strain ε_c.
In order to evaluate the effects of time-dependent compaction, we considered three different scenarios of ratios of final time-dependent (creep) strain and elastic strain in the Kelvin-Chain model (table 2). The model parameters have been chosen such that the total final strain and therefore E_p at infinite time is in all models the same. The models with 50-100% time dependent compaction closely match laboratory experiments (e.g. *Hol et al.*[2015]; *Pruiksma et al*.[2015]), whereas the 500% case mimics the compaction model of Mossop, where time dependent compaction is more dominant than elastic deformation.
A convenient property of the Kelvin-Chain model is that it allows to relate relative stress responses to variability in time dependent compaction to the findings from elastic analysis based on the ratio of Young's modulus of reservoir and surrounding rock as E_{ratio}=E_p/E (c.f. *Mulders* [2003]).

3.2 Model geometry and parametrization

We construct a plane-strain elastic finite element model of a depleting gas reservoir and analyze the sensitivity of total stress scaling and *⊿CFF* to different Kelvin Chain parameters. The numerical model incorporates two reservoir compartments, separated by a fault with a throw of half the reservoir thickness (Fig. 4, Table 1), which can be considered representative for major fault zones in the central area of the Groningen field, in the vicinity of which most seismic events have occured (Fig. 1; *Bourne et al.* [2014]). Obviously, a single fault geometry cannot capture the complex response expected from many mapped faults in the area with variable throw, dip and strike (Fig. 1). Uncertainty in the location of seismic events hampers an allocation of seismic events to particular faults. It is clear that fault strike, dip, throw, natural stress variability, E_{ratio}, can all have a significant control on in-situ stress and spatial and temporal variability in seismicity but are not expected to have a prime control on the relative change in seismic response upon production stop, as these do not affect strongly the ΔCFF as a function of pressure change.
The plane-strain finite element model is adequate for capturing the dominant stress effects. More details of the finite element modelling procedure are given in *Orlic and Wassing* [2013]. The final depletion in the reservoir is 25 MPa, approximately in agreement with pressure depletion at present day in the field. Depletion is implemented to occur simultaneously, at the same rate, in both reservoir compartments in yearly load steps. Prior to depletion, the reservoir is overpressured relative to hydrostatic conditions [*Bourne et al.,* 2014]. The initial ratio of effective horizontal-to-vertical stress is set to $K0_{eff}$=0.45. The visco-elastic model is run for a

1000 years to settle for the gravity loading to produce the $K0_{eff}$. At the reservoir level, the initial stress predicted in the model deviates slightly from the $K0_{eff}$, due to geometric heterogeneities in the visco-elastic properties at reservoir level. To correct for these artefacts, the predicted stresses of the geomechanical model are presented relative to the initial stress of the geomechanical model. The fault zone is assumed to be subject to the reservoir fluid pressure when reservoir rock is present on both sides of the fault. For the portion of the fault where reservoir rock and surrounding rock are juxtaposed, we considered two scenarios for pressure in the fault: actual reservoir pressure or (initial) reservoir pressure.
In the model, the pressure depletion of 25 MPa is built up linearly in a time period of 60 years, followed by 40 years of no pressure change.

3.3 Coulomb failure function (∆CFF) evolution

Figure 5 shows the results for the three time-dependent compaction scenarios. During production the *∆CFF* increases almost linearly with production rate. The total *∆CFF* increase differs, depending on the relative contribution of time-dependent compaction and is in close agreement with the stress response in a pseudo-elastic approach based on E_{ratio}, adopting *E* from table 2 and creep strains from uniaxial Kelvin Chain assumptions (eq. 4) to calculate E_p. In the forty years after production, *∆CFF* increases only moderately by a few percent relative to the *∆CFF* build-up during production. Yearly changes in *∆CFF* decay quickly after production stop. They are lower than the change in *∆CFF* just prior to production stop for all cases considered – largest for the strongest time-dependent compaction scenarios. The moderate amount of total *∆CFF* change after production stop, and the abrupt change in *∆CFF* evolution, are easily understood from the fundamentally different mechanisms contributing to stress changes. Prior to production stop, both the pressure change (eq. 3) and progressive growth of E_{ratio} is contributing to *∆CFF*, whereas after production stop the only contribution to *∆CFF* is the moderate increase of E_{ratio} as a function of progressive compaction.

4. Seismic moment

The previous sections highlight the generic relationship between *∆CFF* with variations in time-dependent compaction. Its bearings on seismicity is evaluated in this section, in terms of the relative effect on seismic moment increase. We determine relative growth of seismic moment based on progressive increase of slip area and slip displacement starting from subcritical in-situ stresses. This is in agreement with the assumption that the Groningen field is located in a tectonically quiet area [*Van Wees et al.,* 2014]. Therefore, gas production is not likely to trigger tectonic seismic activity and seismic energy is considered limited to the strain energy generated by gas depletion (cf. *Bourne et al.* [2014]). Furthermore, it is likely that the initial in-situ stresses on the reservoir faults, which are subject to differential reservoir compaction, are subcritical as the faults are generally not favorably aligned in the present-day stress field, and induced events do not occur before 30-70% of their production depletion suggesting a significant ∆CFF change is required for slip [*Van Wees et al.,* 2014].

For moment prediction related to progressive fault slip we use a semi-analytical approach, which contributes to understanding the relationship between *⊿CFF* change and seismic moment. We refrain from incorporating plastic slip in the finite element model, for the following reasons:

a) an elastic model allows to analyze relative changes in *⊿CFF*, not accidentally biased to potential changes in response due to variability of in-situ stress, specific orientation of faults, and frictional properties
b) a semi-analytical approach based on conservation of fault area integral of *⊿CFF* before and after slip, provides a mechanically robust mechanism to propagate at any stage *⊿CFF* to seismic moment
c) in the analytical approach the variability in shear modulus (eq. 1) can be discarded, and it can be easily adopted in Monte Carlo techniques to asses variability of seismic response to uncertainty in underlying parameters
d) a fully visco-plastic approach would result in more subtle stress interactions relative to the Kelvin-Chain model, but would not change the first order effects of jump in stress response in the model, upon arrest of pressure depletion

For a circular fault area , a closed relationship exists between area *S*, radius *r*, average slip *u*, stress drop $\Delta\sigma$ and seismic moment *M0* [*Eshelby,* 1957; *Keilis-Borok,* 1959]:

$M0 = \frac{16}{7\pi}\Delta\sigma r S$ (eq.6)

This relationship was generalized for elliptic surfaces of fault slip [*Madariaga,* 1979]. In this case, the slip and moment are scaled by a correction factor which takes into account both the ellipticity and the slip direction on the fault. For plane-strain dip-slip faulting conditions the correction factor cancels the term $\frac{16}{7\pi}$, and considering a slipping fault section with *2r* strike and dip length, such that $S=4r^2$:

$M0 = \Delta\sigma 4r^3$ (eq. 7)

The fault moment density [N] per m strike becomes :

$M0_m = \frac{M0}{r} = \Delta\sigma 4r^2$ (eq. 8)

At the onset of slip, *2r* approximately corresponds to the portion of the fault where *⊿CFF* exceeds the Coulomb Failure Criterion. The excess stress of *⊿CFF* relative to the failure criterion is denoted by $\Delta\sigma$, and may be augmented by the stress drop related to dynamic friction [*Rutqvist et al.,* 2013; *Wassing et al.,* 2014].

After slip occurs, the $\Delta\sigma$ is redistributed beyond the tips of the fault slip polygon, such that the area integral of Coulomb Stress change on the fault upon slip remains unchanged [*Wassing et al.,* 2014; *Okada,* 1992], assuming no energy losses.

Numerically, we discretized the *⊿CCF* in patches corresponding to finite element spacing along the dip of the fault. The redistribution of stress is performed following a block-spring stress transfer, in which excess stress is transferred to the neighboring patches, until no more patches are marked by excess stress (cf. *Wassing et al.* [2014]). For faults which are entering slip, r is growing rapidly, resulting in fast growth of fault seismic moment density (c.f. *Van Wees et al.* [2014]). The onset of slip is critically dependent on the in-situ stress on the fault relative to the failure criterion. For prolonged slip with rather stable *r*, growth is more linear (eq. 8).

Post-production time dependent compaction and seismic moment increase

As mentioned in the previous section, time-dependent compaction after 60 years of production would result in a total increase of ΔCFF by 1-2 % relative to the ΔCFF which had been built up during production. It would also be marked by a very quick decay in the build-up of ΔCFF in the first few years after end of production. In figure 6 we plot the evolution of time-dependent compaction and fault seismic moment density (cf. eq. 8) normalized to its value at end of production, jointly with the moments predicted by the heuristic correlation of compaction strain and the logarithm of seismic moment increase (cf. *Bourne et al.* [2014]). The time dependent compaction in Fig. 6 for the 50% and 100% cases is marked by a discontinuity after production stop. This is supported by a clear discontinuity in GPS subsidence data in the central area of the Groningen field occurring 9 weeks after production stop [*Pijper and Van der laan,* 2015] . Markedly, the ratio of seismic moment increase after and before production stop in geomechanical models is approximately three to ten times lower than those predicted from the heuristic approach, for the first few years and decades after shut-in respectively. This holds for all three time-dependent compaction scenarios that are considered here, as well as for both the actual and initial pressure conditions on the fault. The geomechanical predictions are in accordance with the strong reduction of induced events after 80% cut in production rates in the central area in the Groningen field (Fig. 2, *Van Thienen-Visser and Breunese* [2015]). It supports the concept that production rate – through the rate of pressure change and its interplay with time dependent compaction (E_{ratio}) – bears a dominant controlling factor on seismicity.

5. Discussion

The simplified constitutive law for time-dependent compaction and geometry of the model does not allow to assess in depth the sensitivities of the results to variability in geometrical aspects of the reservoir and alternative creep behavior. However, the prediction of significant reduction of seismicity after cessation of production is expected to hold as well for alternative geometries and constitutive laws, as the first order effects are determined by the arrest in pressure change (e.q. 5) .
Apart from time-dependent compaction, other transient processes including creep of surrounding rocks and delayed pressure diffusion in the reservoir or surrounding aquifers can play a role in redistributing stress, after a potential production stop . For depleting reservoirs, pressure diffusion may assist in stabilizing fluid pressures in fault zones but can also result in water-weakening effects on faults due to water influx. Delayed depletion of bottom aquifer and creep of surrounding rocks can result in stress perturbations which can be of similar magnitude as those related to time dependent compaction of the reservoir.
In our model, we assume that pressure does not change after production stop. Because of continued production in the other production clusters of the Groningen field (Fig. 1), in 1-2 years it is expected that reservoir pressures will be further reduced in the central area, due to hydraulic diffusion [*van Thienen-Visser and Breunese,* 2015], which is likely to increase the likelihood of seismicity, compared to the present state.

The prediction of the model, building from the relative increase in expected moment, needs to interpreted with care in view of earthquake processes. An almost critically stressed fault at the end of the production period, which is incrementally loaded by an additional 1-2% of *CFF* predicted by our model after stop of production, could be sufficient to trigger a large event. Numerical inclusion of slip weakening effects and/or rate and state friction effects during rupture events, would result in a less smooth buildup of seismic moment [*Rutqvist et al.,* 2013; *Wassing et al.,* 2014], but is considered beyond the scope of this study.
The fundamental difference between our study and that of *Bourne et al.* [2014] is that we consider the stresses acting on the activated faults as the driving parameters of induced seismicity, rather than using the reservoir compaction as a proxy. These stresses originate from a combination of the direct poro-elastic effect through the pressure changes and from the delayed effect of ongoing compaction after cessation of reservoir production. Our claim is that both mechanisms need to be taken into account.

6. Conclusions

Geomechanical models, incorporating time dependent compaction of reservoir rocks, predict that seismic moment evolution after a production stop is subject to a very moderate increase, in the order of 3 to 10 times less than the values predicted by the heuristic approach correlating seismic moment to progressive compaction strain [*Bourne et al.,* 2014], for the first years and decades following cessation of production respectively. Our model supports low seismicity encountered in the central area of the Groningen Field, where production has been reduced by 80%, since January 17 2014.
The model findings support scope for mitigating induced seismicity through adjusting production scenarios, as the seismicity rates are expected to be correlated primarily with rates of pressure change.
The findings of our study may well be generalized for other depleting reservoirs in similar structural settings, as the strong jump of stress loading behaviour on faults as a function of arrest of pressure changes (eq. 3) is universal, and prolonged stress effects of time dependent compaction are typically one order of magnitude lower, than those of pressure change.
A number of issues, considered beyond the scope of the present study, need to be addressed to augment to the robustness of our findings. These include: a) more realistic constitutive laws for time dependent compaction; b) adoption of the full 3D complexity of reservoir structure and of pressure depletion; c) pressure diffusion and creep in the over and underburden of the reservoir; d) effects of rate and state friction.

7. Acknowledgements

The data used in this manuscript are publically available: seismicity data from the Royal Netherlands Meteorological Institute KNMI (www.knmi.nl); monthly production data from production wells in the Groningen field, available from the Geological

Survey of the Netherlands TNO (www.nlog.nl). We thank Jaap Breunese, Dries Hegen, Bogdan Orlic, and Brecht Wassing for constructive comments on earlier versions of the manuscript.

REFERENCES

Baranova, V., A. Mustaqeem, and S. Bell (1999), A model for induced seismicity caused by hydrocarbon production in the Western Canada Sedimentary Basin*, Can. J. Earth Sci., 36*(1), 47-64, doi: 10.1139/e98-080.

Bardainne, T., N. Dubos-Sallée, G. Sénéchal, P. Gaillot, and H. Perroud (2008), Analysis of the induced seismicity of the Lacq gas field (Southwestern France) and model of deformation*, Geophysical Journal International, 172*(3), 1151-1162, doi: 10.1111/j.1365-246X.2007.03705.x.

Bourne, S. J., S. J. Oates, J. van Elk, and D. Doornhof (2014), A seismological model for earthquakes induced by fluid extraction from a subsurface reservoir*, Journal of Geophysical Research: Solid Earth, 119*(12), 8991-9015, doi: 10.1002/2014JB011663.

Chang, C., E. Mallman, and M. Zoback (2014), Time-dependent subsidence associated with drainage-induced compaction in Gulf of Mexico shales bounding a severely depleted gas reservoir*, AAPG Bull., 98*(6), 1145-1159.

Dahm, T., F. Krüger, K. Stammler, K. Klinge, R. Kind, K. Wylegalla, and J. Grasso (2007), The 2004 Mw 4.4 Rotenburg, Northern Germany, Earthquake and Its Possible Relationship with Gas Recovery*, Bulletin of the Seismological Society of America, 97*(3), 691-704, doi: 10.1785/0120050149.

De Waal, J. A. (1986), On the rate type compaction behaviour of sandstone reservoir rock, PhD thesis, 1-166 pp., Technical University Delft.

Dieterich, J. (1994), A constitutive law for rate of earthquake production and its application to earthquake clustering*, Journal of Geophysical Research, 99*(93), 2601.

Eshelby, J. D. (1957), The determination of the elastic field of an ellipsoidal inclusion, and related problems*, Proceedings of the Royal Society of London.Series A, Mathematical and Physical Sciences, 241*(1226), 376-396.

Fokker, P. A. and K. Van Thienen-Visser (2015), Inversion of double-difference measurements from optical levelling for the Groningen gas field*, Proc. IAHS, 372*, 375-378.

Hettema, M. H. H., P. M. T. M. Schutjens, B. J. M. Verboom, and H. J. Gussinklo (2000), Production-induced compaction of a sandstone reservoir: The strong influence of stress path*, SPE Reservoir Evaluation and Engineering, August*.

Hol, S., A. Mossop, A. J. Van Der linden, P. M. M. Zuiderwijk, and A. Makurat (2015), Long-term compaction behavior of Permian sandstones - An investigation into the mechanisms of subsidence in the Dutch Wadden Sea*., 49th US Rock Mechanics / Geomechanics Symposium, ARMA 15-6184*, 1-8.

Keilis-Borok, V. I. (1959), On estimation of the displacement in an earthquake source and of source dimensions*, Annals of Geofysics, 12*, 205-214.

Kostrov, V. (1974), Seismic moment and energy of earthquakes, and seismic flow of rock*, Physics of the Solid Earth, 1*, 13-21.

Madariaga, R. (1979), On the relation between seismic moment and stress drop in the presence of stress and strength heterogeneity*, Journal of Geophysical Research: Solid Earth, 84*, 2243-2250.

Marketos, G., R. Govers, and C. J. Spiers (2015), Ground motions induced by a producing hydrocarbon reservoir that is overlain by a viscoelastic rocksalt layer: a numerical model*, Geophysical Journal International, 203*(1), 228-242, doi: 10.1093/gji/ggv294.

McGarr, A. (2014), Maximum magnitude earthquakes induced by fluid injection*, Journal of Geophysical Research: Solid Earth, 119*(2), 1008-1019, doi: 10.1002/2013JB010597.

Mossop, A. (2012), An Explanation for Anomalous Time Dependent Subsidence*, 46th US Rock Mechanics / Geomechanics Symposium, ARMA 12-518*, 1-8.

Mulders, F. M. M. (2003), Modelling of stress development and fault slip in and around a producing gas reservoir, Doctoral Thesis thesis, Technical University of Delft.

Okada, Y. (1992), Internal deformation due to shear and tensile faults in a half-space*, Bulletin of the Seismological Society of America, 82*(2), 1018.

Orlic, B. and B. B. T. Wassing (2013), A Study of Stress Change and Fault Slip in Producing Gas Reservoirs Overlain by Elastic and Viscoelastic Caprocks*, Rock Mech Rock Eng, 46*(3), 421-435, doi: 10.1007/s00603-012-0347-6.

Pijper, F. P. and F. D. Van der laan (2015), Phase 1 update May 2015: trend changes in ground subsidence in Groningen (http://www.cbs.nl/nl-NL/menu/themas/industrie-energie/methoden/dataverzameling/overige-dataverzameling/2015-onderzoeksrapporten-bodemdaling-groningen-phase1-update.htm)*, Statistics Netherlands | Scientific paper 2015*, december 1, 2015.

Pruiksma, J. P., J. N. Breunese, K. van Thienen-Visser, and J. A. de Waal (2015), Isotach formulation of the rate type compaction model for sandstone*, Int. J. Rock Mech. Min. Sci., 78*, 127-132, doi: http://dx.doi.org/10.1016/j.ijrmms.2015.06.002.

Roest, J. P. A. and W. Kuilman (1994), Geomechanical analysis of small earthquakes at the Eleveld gas reservoir, doi: 10.2118/28097-MS.

Ruina, A. (1983), Slip Instability and State Variable Friction Laws*, Journal of Geophysical Research, 88*(370), 10.

Rutqvist, J., A. P. Rinaldi, F. Cappa, and G. J. Moridis (2013), Modeling of fault ractivation and induced seismicity during hydraulic fracturing of Shale-Gas reservoir*, Journal of Petroleum Science and Engineering, 107*, 31-44.

Segall, P. (1989), Earthquakes triggered by fluid extraction*, Geology, 17*(10), 942-946, doi: 10.1130/0091-7613(1989)0172.3.CO;2.

Segall, P., J. R. Grasso, and A. Mossop (1994), Poroelastic stressing and induced seismicity near the Lacq gas field, southwestern France*, Journal of Geophysical Research, 99*(B8), 15.

Soltanzadeh, H. and C. D. Hawkes (2008), Semi-analytical models for stress change and fault reactivation induced by reservoir production and injection*, Journal of Petroleum Science and Engineering, 60*, 71, doi: 10.1016/j.petrol.2007.05.006.

Sone, H. and M. D. Zoback (2014), Time-dependent deformation of shale gas reservoir rocks and its long-term effect on the in situ state of stress*, Int. J. Rock Mech. Min. Sci., 69*, 120-132.

Suckale, J. (2009), Induced seismicity in hydrocarbon fields*, Adv. Geophys., 51*, doi: 10.1016/S0065-2687(09)05107-3.

Van Eijs, R. M. H. E., F. M. M. Mulders, M. Nepveu, C. J. Kenter, and B. C. Scheffers (2006), Correlation between hydrocarbon reservoir properties and induced seismicity in the Netherlands*, Eng. Geol., 84*, 99, doi: 10.1016/j.enggeo.2006.01.002.

van Thienen-Visser, K. and J. Breunese (2015), Induced seismicity of the Groningen gas field: History and recent developments*, The Leading Edge, 34*(6), 664-671.

van Thienen-Visser, K., P. A. Fokker, M. Nepveu, D. Sijacic, J. Hettelaar, and B. Kempen (2015), Recent developments on the seismicity of the Groningen field in 2015. (http://www.nlog.nl/resources/Aardbevingen%20Groningen/Recent%20developments%20on%20the%20seismicity%20of%20the%20Groningen%20field%20in%202015_TNO_2015_R10755.pdf), last accessed december 1st 2015*, R10755*, last accessed December 1st 2015.

Van Wees, J. D., L. Buijze, K. Van Thienen-Visser, M. Nepveu, B. B. T. Wassing, B. Orlic, and P. A. Fokker (2014), Geomechanics response and induced seismicity during gas field depletion in the Netherlands*, Geothermics, 52*(0), 206-219, doi: http://dx.doi.org.proxy.library.uu.nl/10.1016/j.geothermics.2014.05.004.

Wassing, B. B. T., J. D. van Wees, and P. A. Fokker (2014), Coupled continuum modeling of fracture reactivation and induced seismicity during enhanced geothermal operations*, Geothermics, 52*(0), 153-164, doi: http://dx.doi.org.proxy.library.uu.nl/10.1016/j.geothermics.2014.05.001.

Parameter	***Value***	***unit***
E	*18*	*GPa*
v	*0.2*	*-*
Top reservoir	*2900*	*m*
Thickness reservoir	*150*	*m*
Fluid density	*1150*	*Kgm^{-3}*
Rock density	*2260*	*kgm^{-3}*
Friction angle	*30*	*degrees*
Fault dip	*70*	*degrees*
Depletion	*25*	*MPa*
$K0_{eff}$	*0.45*	*-*

Table 1: parameters of the geomechanical model

Scenario	***E***	***E1***	$\tau = \eta_1/E_1$
50% creep	*13.5 GPa*	*27 GPa*	*7.3 year*
100% creep	*18 GPa*	*18 GPa*	*7.3 year*
500% creep	*54 GPa*	*10.8 GPa*	*7.3 year*

Table 2: visco-elastic parameters in the kelvin chain model (Fig. 3). Viscosity η_1 is chosen such that it agrees with a relaxation time τ =7.3 year (Mossop, 2012)

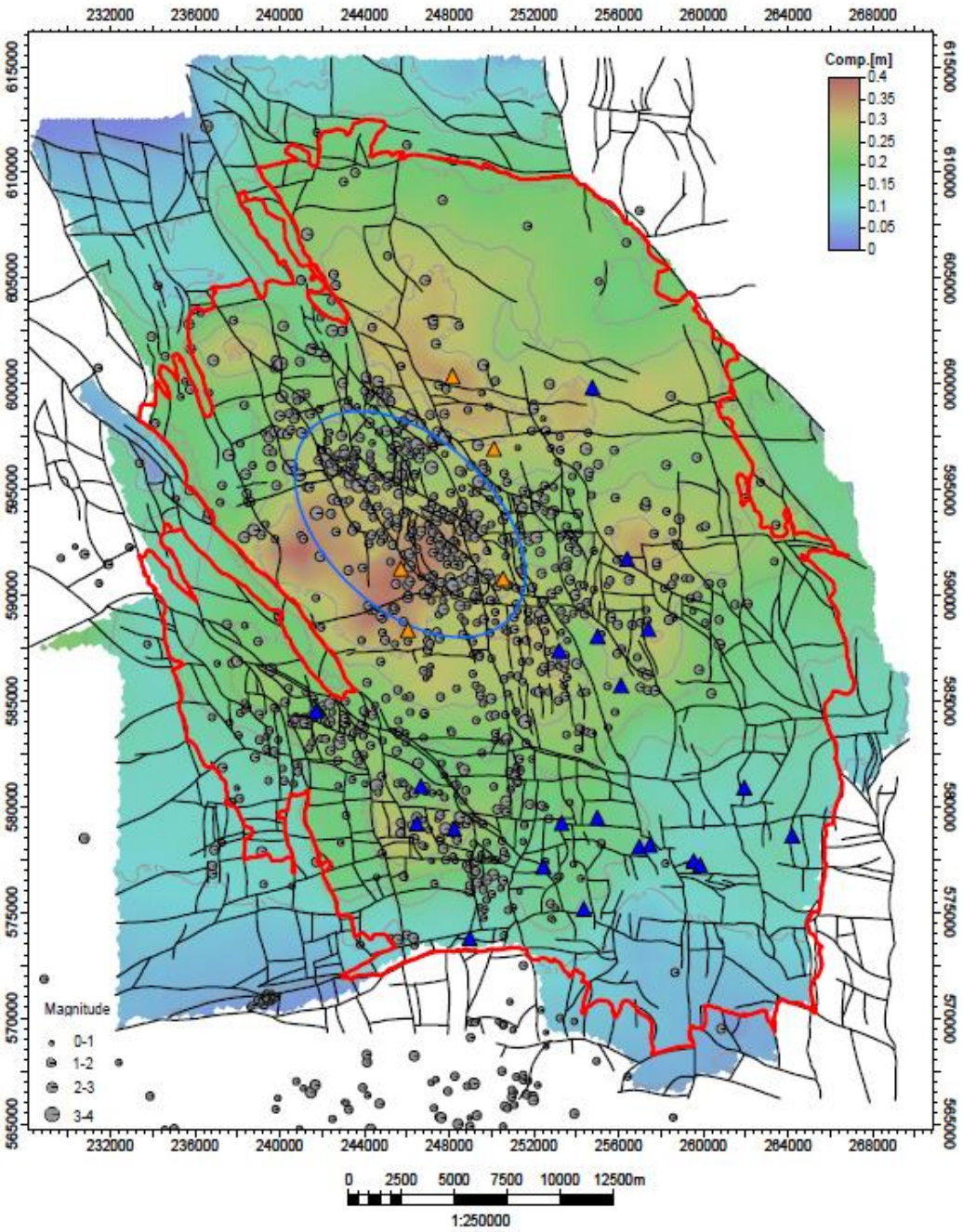

Figure 1. Outline of the Groningen field (red line denotes gas water contact), colored with compaction from subsidence inversion (after Fokker and Van Thienen-Visser, 2015). Induced events until august 1, 2015 for the field are indicated by grey dots (source www.knmi.nl), production clusters by triangles. Induced seismicity of central area within the blue polygon is shown in Fig. 2, jointly with production data of central area production clusters (orange triangles). The hydraulic diffusivity of the reservoir is such that pressure gets equilibrated in between production clusters in the central area within months to half a year, whereas pressure diffusion from the edges of the field to the center would take over a few years [*van Thienen-Visser and Breunese,* 2015].

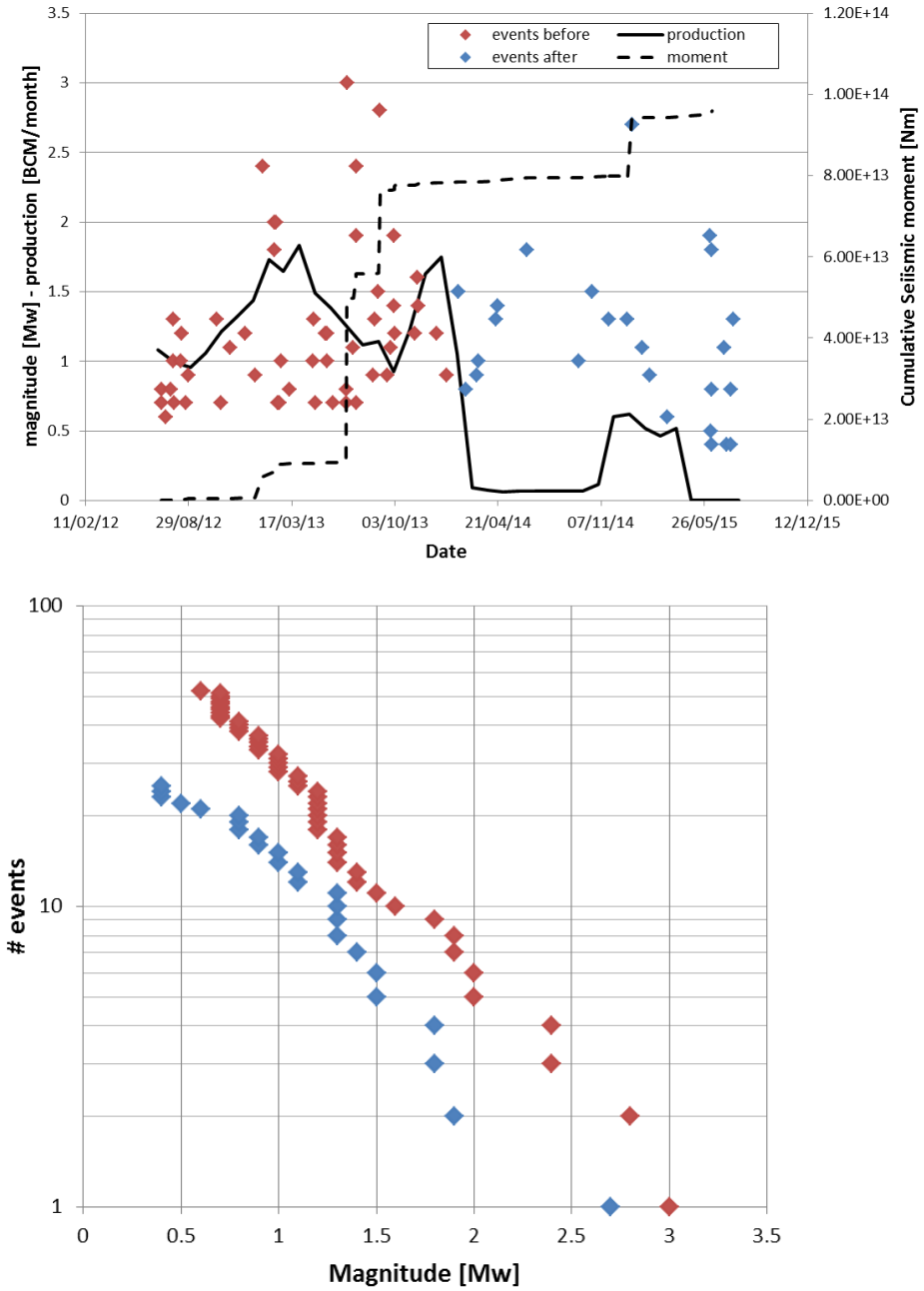

Figure 2 (top) production for Groningen's central area production cluster (solid, source www.nlog.nl), cumulative seismic moment (dashed) and induced seismic events from the central area 1.5 year before (red) and 1.5 years after (blue) production reduction (source www.knmi.nl). (below) Gutenberg-richter plot of seismic events before and after reduction in production.

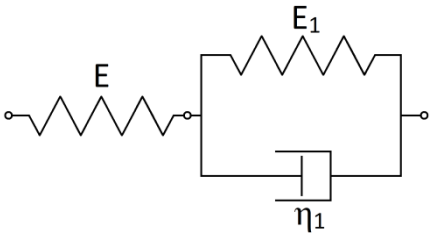

Figure 3: Kelvin Chain constitutive model adopted for time dependent compaction.

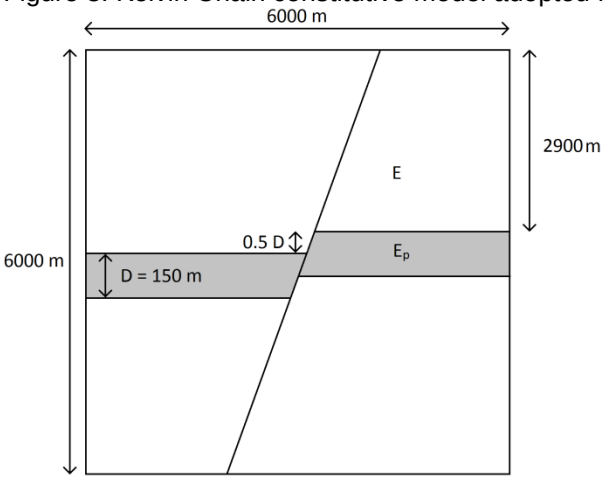

Figure 4 Geometry set-up for geomechanical model

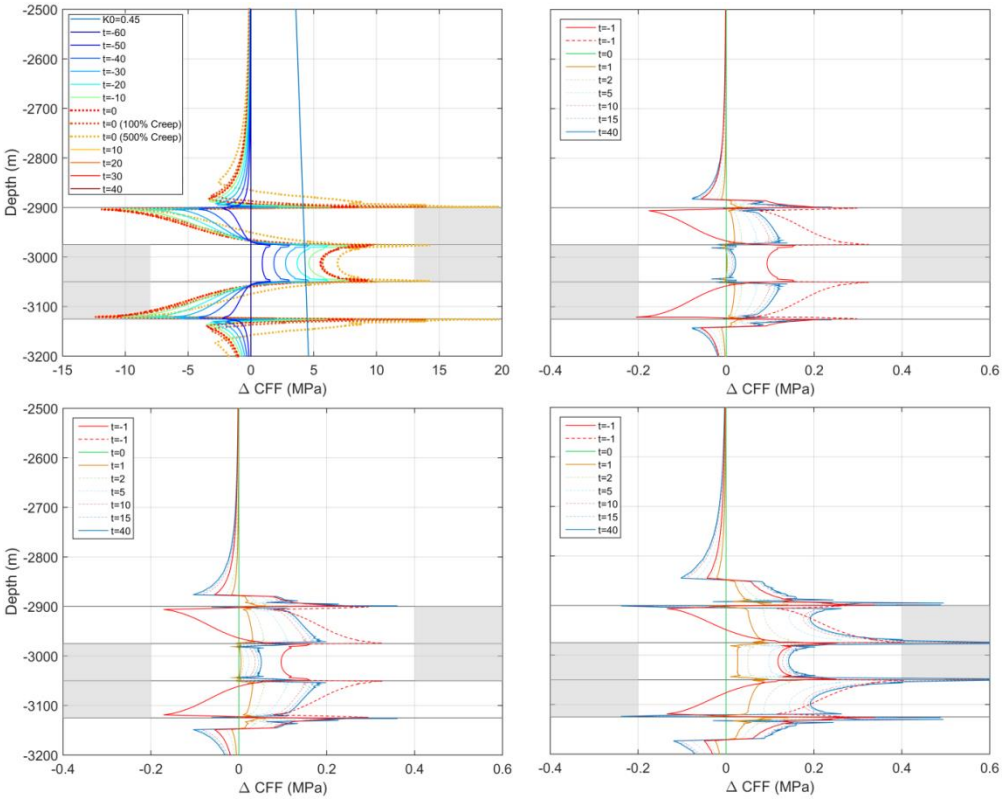

Figure 5: (top left) Change in the Coulomb stress function *ΔCFF* on fault in the geomechanical model for the 50% creep (time dependent compaction) scenario for 10 year increments (t=0 corresponds to production stop), including the *ΔCFF* solution at production stop (t=0) for 100% and 500% creep. (top right) *ΔCFF* increase for 1 year before production stop, and 1,2,5,10,15, and 40 years after production stop for 50% creep, (bottom left) 100% creep and (bottom right) 500% creep. For t=-1 solid red line corresponds to reservoir pressure and dashed line to ambient pressure assumption on the fault.

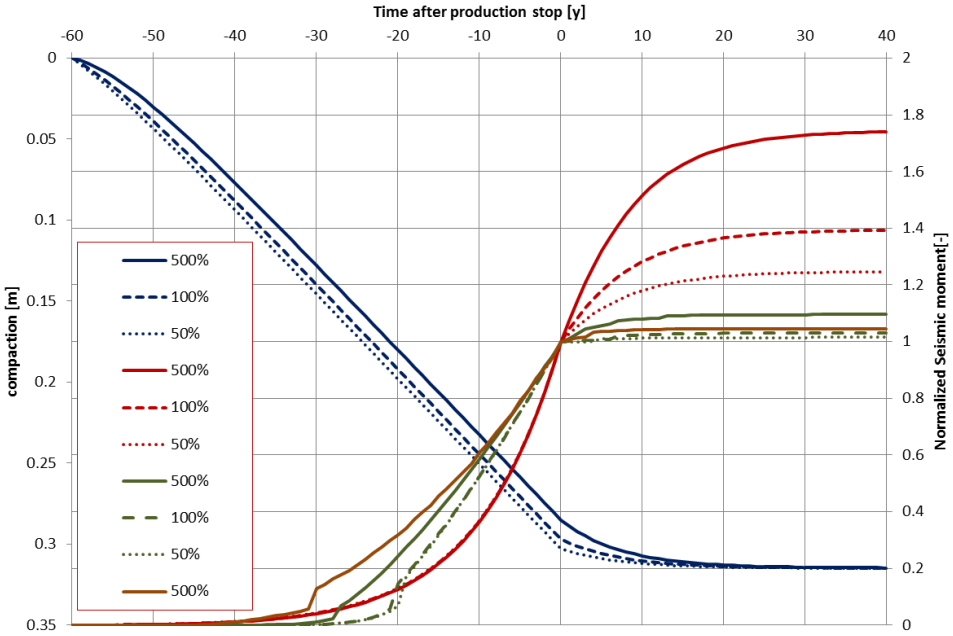

Figure 6: Uniaxial compaction (blue) in the geomechanical model for different time dependent Kelvin-Chain models (500%, 100%, 50% creep), predicted seismic moment from Bourne et al. (2014) (red), and predicted seismic moment from the geomechanical model (green for reservoir pressure, brown for ambient pressure conditions on the fault). Seismic moment is normalized to the value of seismic moment at the end of production (t=0).